Boston University

OpenBU **http://open.bu.edu**

Theses & Dissertations Boston University Theses & Dissertations

2017

Real-time tissue viability assessment using near-infrared light

https://hdl.handle.net/2144/23379

Boston University

BOSTON UNIVERSITY

COLLEGE OF ENGINEERING

Dissertation

REAL-TIME TISSUE VIABILITY ASSESSMENT USING NEAR-INFRARED LIGHT

by

JOSEPH PAUL ANGELO JR.

B.S., Drexel University, 2010
M.S., Boston University, 2014

Submitted in partial fulfillment of the

requirements for the degree of

Doctor of Philosophy

2017

© 2017 by
JOSEPH PAUL ANGELO JR.
All rights reserved, except for
Chapter 3 – Part 1 © SPIE 2014
Chapter 3 – Part 2 © SPIE 2015
Chapter 4 – Part 1 © OSA 2015
Chapter 4 – Part 2 © SPIE 2014
Chapter 5 – Part 1 © SPIE 2016
Chapter 6 – Part 3 © Wolters Kluwer Health, Inc. 2014

Approved by

First Reader _____

Irving J. Bigio, Ph.D.
Professor of Biomedical Engineering
Professor of Electrical and Computer Engineering

Second Reader _____

Sylvain Gioux, Ph.D.
Professor of Biomedical Engineering
Université de Strasbourg

Third Reader _____

Bernard T. Lee, M.D., M.B.A., M.P.H.
Associate Professor of Surgery
Harvard Medical School

Fourth Reader _____

Darren Roblyer, Ph.D.
Assistant Professor of Biomedical Engineering

Fifth Reader _____

Joyce Y. Wong, Ph.D.
Professor of Biomedical Engineering
Professor of Materials Science and Engineering

DEDICATION

To my parents, Joseph and Teresa.

ACKNOWLEDGMENTS

To Sylvain Gioux, your endless tenacity for innovation and progress always leaves me inspired. I've never stopped learning since I took your class and decided to join you on this journey. With your help, I've learned more about myself than ever before, and for that I am truly grateful.

To Irving Bigio, Darren Roblyer, Bernie Lee, and Joyce Wong, thank you for being so available, helpful, and friendly! I think I couldn't have asked for a more smiley bunch of professors for my committee. Our shared laughs made any struggle that much easier.

To everyone I worked with at Boston University and the Beth Israel Deaconess Medical Center, thank you for your time, your guidance, and your friendship! You made going to 'work' a joy and I look forward to our next adventure.

Special thanks to all the teachers who inspired me along the way - this work is your work.

Thank you from the bottom of my heart to my cherished family, my amazing friends, and my wonderful girlfriend, Sara. Most of all, thanks to my mother and father who have given me everything I have. You have always believed in me and have given me the support and freedom to dream. By any measure, any and all success I find is yours.

REAL-TIME TISSUE VIABILITY ASSESSMENT

USING NEAR-INFRARED LIGHT

JOSEPH PAUL ANGELO JR.

Boston University College of Engineering, 2017

Major Professor: Irving J. Bigio, Ph.D., Professor of Biomedical Engineering, Professor of Electrical and Computer Engineering

ABSTRACT

Despite significant advances in medical imaging technologies, there currently exist no tools to effectively assist healthcare professionals during surgical procedures. In turn, procedures remain subjective and dependent on experience, resulting in avoidable failure and significant quality of care disparities across hospitals.

Optical techniques are gaining popularity in clinical research because they are low cost, non-invasive, portable, and can retrieve both fluorescence and endogenous contrast information, providing physiological information relative to perfusion, oxygenation, metabolism, hydration, and sub-cellular content. Near-infrared (NIR) light is especially well suited for biological tissue and does not cause tissue damage from ionizing radiation or heat.

My dissertation has been focused on developing rapid imaging techniques for mapping endogenous tissue constituents to aid surgical guidance. These techniques allow, for the first time, video-rate quantitative acquisition over a large field of view (> 100 cm^2) in widefield and endoscopic implementations. The optical system analysis has been focused

on the spatial-frequency domain for its ease of quantitative measurements over large fields of view and for its recent development in real-time acquisition, single snapshot of optical properties (SSOP) imaging.

Using these methods, this dissertation provides novel improvements and implementations to SSOP, including both widefield and endoscopic instrumentations capable of video-rate acquisition of optical properties and sample surface profile maps. In turn, these measures generate profile-corrected maps of hemoglobin concentration that are highly beneficial for perfusion and overall tissue viability. Also utilizing optical property maps, a novel technique for quantitative fluorescence imaging was also demonstrated, showing large improvement over standard and ratiometric methods. To enable real-time feedback, rapid processing algorithms were designed using lookup tables that provide a 100x improvement in processing speed. Finally, these techniques were demonstrated *in vivo* to investigate their ability for early detection of tissue failure due to ischemia. Both pre-clinical studies show endogenous contrast imaging can provide early measures of future tissue viability.

The goal of this work has been to provide the foundation for real-time imaging systems that provide tissue constituent quantification for tissue viability assessments.

TABLE OF CONTENTS

LIST OF TABLES

LIST OF FIGURES

LIST OF ABBREVIATIONS

AC	Alternating current
B.S.	Bachelors of Science
CCD	Charge-coupled device
CMOS	Complementary metal–oxide–semiconductor
CT	Computed tomography
CW	Continuous wave
DC	Direct current
DMD	Digital micro-mirror device
DOSI	Diffuse optical spectroscopy imaging
FDA	Food and Drug Administration
FDPM	Frequency domain photon migration
FHI	Fabricolor Holding Int'l LLC
FOV	Field of view
FPGA	Field-programmable gate array
FPS	Frames per second
FWHM	Full width half maximum
GPU	Graphics processing unit
HDR	Habilitation à diriger des recherches
ICG	Indocyanine green
LD	Laser diode
LDI	Laser Doppler imaging
LED	Light-emitting diode
LSI	Laser speckle imaging
LUT	Lookup table
M.B.A.	Master of Business Administration
MC	Monte Carlo
M.D.	Doctor of Medicine
MDSI	Masked detection of structured illumination
MFP	Mean free path
MFP'	Transport mean free path
M.P.H.	Master of Public Health
MRI	Magnetic resonance imaging
M.S.	Master of Science
NIH	National Institutes of Health
NIR	Near-infrared
NSF	National Science Foundation
OCT	Optical coherence tomography
PCA	Principal component analysis

PET	Positron emission tomography
Ph.D.	Doctor of Philosophy
PpIX	Protoporphyrin IX
qF-SSOP	Quantitative fluorescence Single Snapshot of Optical Properties
Rd	Diffuse reflectance
ROI	Region of interest
RTE	Radiative transfer equation
SBR	Signal-to-background ratio
SFDI	Spatial frequency domain imaging
s-MTF	Spatial modulation transfer function
SNR	Signal-to-noise ratio
SPECT	Single-photon emission computed tomography
s-PSF	Spatial point spread function
SSB	Single sideband
SSOP	Single snapshot of optical properties
t-MTF	Temporal modulation transfer function
t-PSF	Temporal point spread function
US	Ultrasound
VCA	Vascularized composite allotransplantation

CHAPTER 1: INTRODUCTION

1.1 Motivation

Successful novel imaging technologies in the operating room must fit into the current protocol/standard of care and provide clinicians with information to impact patient outcomes. This is clearly a challenging task, as exemplified by the limited number of technologies that have reached daily clinical use in operating rooms today. While X-Ray Computed Tomography (CT) is now fairly common as a diagnostic tool, it requires a high dose of harmful ionizing radiation per examination, making it impractical as a monitoring method. Likewise, Positron Emission Tomography (PET) and Single-Photon Emission Computed Tomography (SPECT) are both costly and expose patients to ionizing radiation. On the other hand, the non-ionizing scans of Magnetic Resonance Imaging (MRI) are very slow, costly, and prohibit the use of any metallic object in the operating theater. Finally, ultrasound (US) techniques are very low cost and can provide instant feedback, but require contact with the patient and generate low contrast image slices into the body. The ideal surgical guidance technology should be low-cost and provide rapid feedback, while still providing high-resolution images that can be used to impact point-of-care decisions.

Optical imaging has the potential to solve this longstanding clinical need. Near-infrared (NIR) diffuse optical imaging techniques use the deep penetration of NIR light to provide fast, inexpensive, quantitative measurements with non-ionizing light. Most diffuse optical

technologies are also scalable, and so can provide images up to desired fields of view, from microscopic to macroscopic scales. However, with current technologies there is a general tradeoff between field of view, temporal resolution, and spatial resolution. For operating room use the technology should be fast enough so as to not slow down the clinical workflow, provide clear enough images so as to be visually helpful, and have a field of view large enough to help guide surgical procedures. The proposed dissertation work aims to develop and validate an optical quantitative technique to fit this need.

1.2 Chapter Summaries

All work presented in this dissertation is within the context of providing surgical guidance with quantitative optical measures to assess tissue viability. The fundamentals of light-tissue interactions and photon transport modeling are provided for reference in Chapter 2. This is followed by a review of the current optical modalities for clinical imaging. Much of the novel work presented from Chapter 3 to Chapter 6 relies on a particular technique, spatial frequency domain imaging, which is covered in detail. Finally, the state of the art in spatial frequency domain imaging is presented along with signal processing theory for thoroughness and preparation for the following chapters.

Chapter 3 introduces two novel imaging techniques that utilize structured illumination in order to enhance the current capabilities of fluorescence imaging. The first part, which also happens to be my first project, describes our masked detection of structured illumination technique, or MDSI. MDSI aims to enhance fluorescence imaging by

selectively improving relative signal for either shallow or deep fluorophores through instrumentation only. The second chapter part, which happens to be my final project, presents a novel combination of techniques called quantitative fluorescence single snapshot of optical properties, or qF-SSOP. This technique enables real-time fluorescence imaging that is quantitatively corrected for variations due to optical properties.

Chapter 4 and beyond focuses on endogenous imaging techniques that do not rely on drugs or dyes for contrast. Instead, physiological markers such as the concentration of oxy- and deoxyhemoglobin are quantified and imaged using real-time acquisition techniques. In the first part, a powerful profile-correction feature is introduced for snapshot of optical properties (SSOP) imaging. In the clinic, samples are expected to have topographical variation, and this technique introduces profile-corrected measurements of tissue optical properties with real-time acquisition. However, approximately 50% of surgeries are minimally invasive, making access an issue for widefield imaging techniques such as the ones developed previously. The next two parts present the evolution of SSOP towards endoscopic imaging that measures sample distance, optical properties, and tissue oxygenation with a single measurement. Measurement speed is limited only to camera exposure time, and so video framerates of tissue oxygenation are possible.

Chapter 5 presents work developing processing methods to help the real-time acquisition techniques presented in Chapter 4 provide real-time feedback. Two strategies are

presented that improve the processing speeds for spatial-frequency-domain inverse problem solving by a factor of 100. These strategies are flexible for different implementations and can be adapted to a variety of problems.

Chapter 6 demonstrates the ability for the presented optical techniques to assess tissue viability in novel ways. The part presents an ischemic tissue model, i.e. inadequate blood supply, for a rat skin flap that results in a gradient of perfusion across the flap. Skin tissue without enough blood supply undergoes necrosis, and this boundary between necrotic and viable tissue takes several days to fully form. This part investigates endogenous imaging for predicting this necrosis boundary as early as 5 minutes after blood supply is cut off. Part two utilizes a pig facial flap model to investigate the sensing capability of spatial frequency domain imaging for tracking and discerning between venous and arterial occlusions. Here, the measurement of both oxy- and deoxyhemoglobin are paramount for distinguishing venous and arterial occlusions and that oxygenation measurements alone cannot discern between the two.

Finally, Chapter 7 presents conclusions and future direction based on this body of work.

CHAPTER 2: BACKGROUND

Though not covered in this chapter, the fundamentals of electromagnetic radiation are as fascinating as they are enlightening. While a basic knowledge of optics and mathematics is assumed for readers of this dissertation, if more information is sought after I highly recommend The Feynman's Lectures of Physics that are freely available online. There, Dr. Richard Feynman covers basic physics principles such as wave propagation, the Law of Least Action, and wave-particle duality with all the fervor and curiosity of a man in love. While romantic, he is forever pragmatic with understanding the laws of nature, "the first principle is that you must not fool yourself and you are the easiest person to fool."

2.1 Light-tissue Interactions

Scattering, absorption, and fluorescence are the three main parameters that govern propagation of light in tissue. Because fluorescence is essentially a conversion of energy that changes the wavelength of light, it will be considered here as an absorption event. Mathematically, the absorbance *A* of light through a single chromophore at concentration *C* over a path length *L* is described by the Beer-Lambert Law:

$$A(\lambda) = \varepsilon(\lambda) \cdot C \cdot L = \frac{\mu_a(\lambda) \cdot L}{2.303} \quad (1)$$

where ε is the molar extinction coefficient and μa, the absorption coefficient, is the probability of absorption per unit path length, λ is the wavelength of light.

Experimentally transmittance T can be calculated by taking the ratio of output intensity I over the input intensity I_0 and taking its logarithm:

$$T(\lambda) = \frac{I(\lambda)}{I_0(\lambda)} = e^{-\mu_a(\lambda)\cdot L} \tag{2}$$

However, there are multiple chromophores in living tissues, each with a unique, wavelength dependent molar extinction coefficient ε that contributes to a sample's absorption coefficient μ_a.

$$\mu_a(\lambda) = 2.303 \cdot \sum_{i=1}^{N} \varepsilon_i(\lambda) \cdot C_i \tag{3}$$

However, there are multiple chromophores in living tissues, each with a unique, wavelength dependent molar extinction coefficient ε that contributes to a sample's absorption coefficient μ_a.

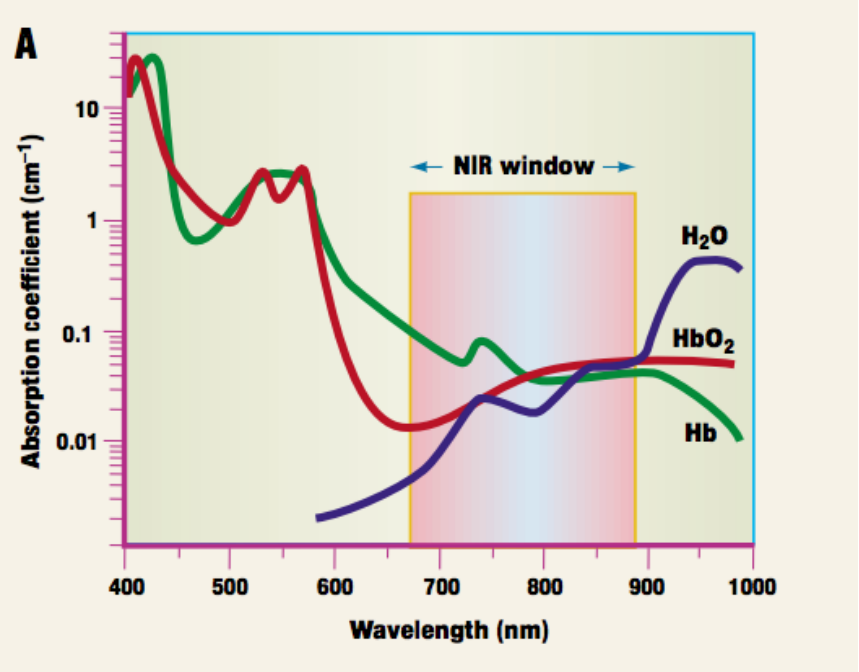

Figure 2.1: NIR window in biological tissue – adapted from here.[182]

The major endogenous chromophores in tissues are oxy-hemoglobin, deoxy-hemoglobin, and water. The molar extinction coefficients for these substances are well known (see Fig. 2.1.1), and so if one knew the absorbance spectrum of a sample, the molecular content can be extracted via Eqs. (1–3), i.e. absorption spectroscopy.[101,102,186] However, scattering dominates over absorption in tissue, greatly effecting optical path length, and must be considered in order to extract tissue constituent concentrations.[41]

Scattering (in our case elastic scattering) is a complex phenomenon that, in its simplest form, describes the refraction of light in diffusive media. It can be described using a power law in which the coefficient depends on the type of tissue[28,151] and is caused by boundary changes in refractive index, and depends on scatterer size, shape, and molecular

makeup. Though mostly attributed to sub-cellular content (nuclear size[66], cell membranes[14], mitochondria[13], etc.),[113,125] local order and structure should also be considered if studying single or limited scattering events[131] or in highly oriented media.[84] Furthermore, the physiological state of these organelles can be correlated with an optical signature, leading to diagnosis of a disease state.[12,110] Similar to absorption, the ratio of transmitted light I retaining its original direction to incident light I_0 through a purely scattering substance can used to describe scattering,

$$T(\lambda) = \frac{I(\lambda)}{I_0(\lambda)} = e^{-\mu_s(\lambda)\cdot L} \tag{4}$$

where T is the transmission of light, the scattering coefficient, μ_s, is the probability of scattering per unit path length, and L is the path length. In addition to the probability of scattering, one must also consider the angle of scatter, often described by a phase function $p(\theta, \Psi)$. The phase function describes the directional probability of scatter. For relatively large particles like those in tissue, individual interactions are described by Mie scattering that have highly forward scattering profiles., After multiple scattering events from randomly oriented scattering structures in tissue, the scattering dependence on the azimuthal angle Ψ averages isotropically and is therefore ignored while the polar angle θ is averaged to a form the anisotropy of scatter, $g = <\cos(\theta)>$, that characterizes scattering in tissue in terms of the relative amount of forward to backward direction of scatter.[78] This factor helps simplify the scattering dependence of tissue and effectively combines the scattering coefficient, μ_s, and the anisotropy factor g, to a reduced scattering coefficient

$$\mu_s' = (1 - g)\mu_s \tag{5}$$

However, it should be mentioned that for minimally scattered photons, the exact form of the phase function should be considered.[112] From here, the foundation is laid for discussing how photon migration is modeled in tissue.

2.2 Light Propagation Modeling

While Maxwell's equations describe the fundamental interactions of photon waves with matter, modeling on this level requires is impractical for scales much larger than the wavelength of light. However, modeling bulk properties of light energy transfer is extremely useful and will be briefly presented here.

2.2.1 Transport Theory

In transport phenomena, transport theory is a heuristic approach to modeling the propagation of a flux via conservation laws. Photon transport in biological tissue can likewise be modeled by the radiative transfer equation (RTE) based on conservation of energy, characterized by the radiance $L(\vec{r}, \hat{s}, t)$ [W/m2·sr], defined as the amount of energy flowing through elemental area per unit solid angle per unit time. Six independent variables define the radiance: position vector $\vec{r}(x, y, z)$, direction vector $\hat{s}(\theta, \varphi)$, and time *t*. So defined, the RTE states

$$\frac{1}{c}\frac{\partial L(\vec{r}, \hat{s}, t)}{\partial t} = -\hat{s} \cdot \nabla L(\vec{r}, \hat{s}, t) - \mu_t L(\vec{r}, \hat{s}, t) + \mu_s \int_{4\pi} L(\vec{r}, \hat{s}, t) P(\hat{s}' \cdot \hat{s}, t) d\Omega' + S(\vec{r}, \hat{s}, t) \tag{6}$$

where c is the speed of light in the tissue, $\mu_t = \mu_a + \mu_s$ is the extinction coefficient, $P(\hat{s}' \cdot \hat{s}, t)$ is the aforementioned phase function in vector, time dependent form, and *S* is the source. This models light propagation such that radiance can be lost via extinction and divergence, i.e. from absorption and scattering away from $\hat{s}$, respectively, and gained from a source, $S(\vec{r}, \hat{s}, t)$, or scattering from $\hat{s}'$ into $\hat{s}$. Coherence, polarization, and non-linearity are neglected here. Optical properties are assumed to be time-invariant, though can vary spatially, and scattering is assumed to be elastic. The RTE can be implemented numerically using Monte Carlo methods to produce highly accurate results for many conditions and is considered a gold standard in modeling.[179,202] However, these methods are computationally expensive and not analytically tractable for modeling light in tissue.

2.2.2 Diffusion Approximation

A full derivation of the diffusion equation from the RTE can be found here.[180] Briefly, two main assumptions are made to reach the diffusion equation from the RTE. First, relative to the high number of scattering events, absorption events are rare, resulting in a nearly isotropic propagation of radiance. Second, over one transport mean free path the fractional change in current density is much less than unity, meaning there should be no harsh boundaries in optical properties or indices of refraction. Both of these assumptions require a turbid media in which $\mu_s' >> \mu_a$, and source–detector separation large enough, which is appropriate for most measurement in biological tissue. To reach this formalism, first it is useful to define the fluence rate Φ

$$\Phi(\vec{r}, t) = \int_{4\pi} L(\vec{r}, \hat{s}, t) \tag{7}$$

which describes the total number of photons incident from all directions on a unit sphere divided by the cross-sectional area of the sphere and per time interval. The above equation simply integrates the radiance *L* in all directions, resulting in the scalar value of fluence rate Φ. Now, assuming that light has scattered enough to lose all directionality, an isotropic, diffusive propagation of energy is described by the diffusion equation

$$\frac{1}{c}\frac{\partial\Phi(\vec{r},t)}{\partial t} + \mu_a\Phi(\vec{r},t) - D\nabla^2\Phi(\vec{r},t) = S(\vec{r},t) \tag{8}$$

where *D* is the diffusion coefficient $1/3(\mu_a + \mu_s')$ and *S* describes the photon source. Now, the original six independent variables have been reduced to four, and analytical solutions are readily available for several geometries and domain types (discussed below). Note, this formulation does not depend on μ_s, but on μ_s' only, meaning that all scattering direction information is simplified to the anisotropy factor g. Work has been done recently to probe a higher order scattering anisotropy factor γ

$$\gamma = \frac{1-g_2}{1-g_1} \tag{9}$$

to sense the likelihood of backscatter in a medium that can correlate with physiological changes in tissue.[27,29,107] This factor depends on the first and second Legendre moments of the scattering phase function, though to be sensitive to the second moment g_2 the length scale must be shorter than what is applicable for the diffusion regime.[16,194]

Now that limits are being set on when the diffusion equation is appropriate and when it is not, it is necessary to define parameters that somehow normalize unique optical property combinations into comparable factors. In any physical description of a medium with tractable interactions, it is useful to define the mean free path (*MFP*) of the medium as the average distance traveled by a photon between collisions that cause directional change or energy loss. Here, photons are interacting with absorbers and scatterers as

$$MFP = \frac{1}{\mu_a + \mu_s} \tag{10}$$

However, because the diffusion equation assumes many scattering events have occurred and a loss of source directionality, it is appropriate to define a transport mean free path

$$MFP' = \frac{1}{\mu_a + \mu_s'} \tag{11}$$

that uses the reduced scattering coefficient μ_s'. Now, it should be noted that the accuracy of the diffusion equation diminishes within of 3-4 transport mean free path lengths of a source or distinct boundary.[194] There are higher order approximations such as P_3 that results in both a more complicated expression and a more accurate model than the standard diffusion approximation, especially at distances shorter than one *MFP′*.[122] Figure 2.2.1 demonstrates the increased accuracy of the diffusion equation with increased distance from the source. Still, the diffusion equation's accuracy over large scales and computational ease allow for relatively fast extraction tissue of optical properties and has led to the development of several diffuse optical imaging technologies.

2.2.3 Monte Carlo Modeling

Maxwell's equations can be used to model light-particle interactions that are on the order of the wavelength of light but becomes cumbersome for large-scale interactions. The RTE can be simplified with assumptions in order to form an analytical expression that works best when modeling photon migration over several *MFP'*s. When modeling light-tissue interactions that are much longer than the wavelength of light and perhaps up to multiple *MFP'*s, Monte Carlo (MC) modeling is most appropriate (see Fig. 2.2.1). MC modeling involves computational algorithms that step photons through a well-defined media based on the probability of energy loss due to absorption and the directional probability of scattering. MC methods are necessarily statistical, requiring a large number of simulated photons and hence computational time and power. However, many iterations and improvements have been made since its first use for light-tissue interactions[184] that include features such as polarization,[133] quantum absorption,[26] multiple tissue layers,[179] and parallel computing implementation.[2] A thorough review can be read here.[80]

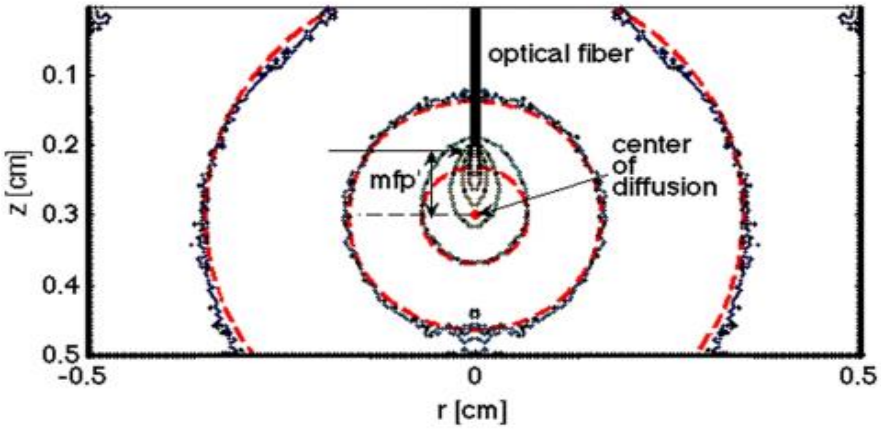

Figure 2.2.1: Comparison of Monte Carlo (black dots) and Diffusion Approximation (dashed red line) light propagation models. Iso-concentration contour plots show little agreement between these methods for measurements close to the source, but show strong agreement at longer distances – adapted from here.[79]

2.3 Current Optical Modalities for Clinical Imaging

2.3.1 Fluorescence Imaging

Through a phenomenon of conversion of energy within a molecule, a change in wavelength, or fluorescence, will occur. This "color" change allows for the isolation of light that has interacted with the molecule. Some endogenous tissues constituents fluoresce (termed autofluorescence), providing imaging contrast and diagnostic information[40,142], however, this same signal can cause a higher background signal for other fluorescent targets. Several techniques are used to minimize or subtract a autofluorescent background signal, such as the use of near-infrared (NIR) light or fluorescent lifetime quantification.[1] Thusly, exogenous contrast agents can appear as "bright stars on a black background," i.e. imaging a high signal to background ratio (SBR).

Image-guided surgery using exogenous contrast agents has been a hot topic as of late with the advent of several pre-clinical and clinical-ready instruments. The Novadaq SPY™ (www.novadaq.com) and the Fluobeam™ (www.fluoptics.com) are currently approved by the U.S. Food and Drug Administration (FDA), while other experimental systems, e.g. the FLARE™ camera system (www.frangionilab.org), the Artemis™ camera system (www.O2view.com), and the Photodynamic Eye (Hamamatsu Photonics, Hamamatsu City, Japan), have eligibility for 510(k) approval from the FDA based on the Novadaq system as a predicate. Several reviews exist to explicate the parameters and applications of such systems.[61,82,144] These powerful, real-time imaging techniques have

great potential for clinical impact though they rely on the use of exogenous fluorophores, of which none are currently FDA approved for the indications relevant to image-guided surgery.

2.3.2 Multi-spectral Imaging

Multi-spectral imaging is a continuous wave technique that uses planar illumination to acquire images at several wavelengths. There are two main types of multi-spectral imaging: chromophore imaging and spectral unmixing. In chromophore imaging, the scattering and absorption coefficients cannot be separated. So, in order to acquire chromophore parameters, such as tissue oxygenation, assumptions are made about the tissue's scattering properties. It should be noted that monochrome continuous wave (CW) techniques cannot uniquely separate μ_a and μ_s',[9,188] but utilizing several wavelengths can overcome this downfall by the careful selection of measurement wavelengths.[34] Recent work has achieved this in a single acquisition.[81] Spectral unmixing relies on a priori knowledge of the fluorophores' emission spectra and principal component analysis (PCA) in order to color-code an analyzed image.

2.3.3 Coherence Techniques

An even more successful optical imaging technique that has reached the clinic is optical coherence tomography (OCT). Though there are several forms and measurement domains of the technique, the basic principle relies on low coherence interferometry, allowing interference to occur between the output signal and a reference signal at very specific depths within a sample. Therefore, the techniques rely on label-free, backscattering

contrast. For clinical use, ophthalmic OCT is now the standard-of-care in the U.S. and in Europe[56] and has been one of the main successes of optical imaging technologies. Likewise, intravascular OCT is quickly becoming the standard-of-care in interventional cardiology,[155] and many other emerging implementations, such as endoscopic OCT, are on the rise.[20] Scan rates depend on the type of OCT and the instrumentation used (often >5 second per 3D scan),[162] but algorithms have been developed to utilize graphics processing units (GPUs) for real-time feedback.[196,197] However, the sampled area is generally under 1 cm2 and not suitable for widefield imaging applications.

Laser Doppler imaging (LDI) has also reached the clinic with its ability to measure blood flow because anomalous peripheral blood flow can be an indicator for many health disorders.[50,88,114] The technique relies on the classic Doppler effect between an input signal and the reflected signal off of a moving particle. This reflected signal will have a frequency shift directly related to the particle's speed, enabling blood flow measurements for point, scanning, and (simultaneous) full field measurements. Real-time, full field LDI has been achieved on the bench-top through the use of a fast complementary metal oxide semiconductor (CMOS) camera with a generous FOV (~50 cm2) over 480 x 480 pixels capable of 12–14 fps.[97] The technology can be further refined by addressing a few issues, such as low signal-to-noise ratio (SNR), motion artifacts, and its FOV by increasing laser power and photosensitivity of its high-speed CMOS sensors.

A very similar technique, laser speckle imaging (LSI) has also found many applications

in measuring blood flow. A thorough overview of the various laser speckle techniques can be found here.[46] This technique uses laser speckle created from a coherent laser reflecting off a diffusive surface. The speckle pattern changes over time and space when the sample moves, and so techniques tend to be temporally- or spatially-resolved at the cost of the alternate domain's resolution. The use of laser speckle has been inherently widefield and held that advantage over LDI until said real-time, full field LDI was developed. A disadvantage to laser speckle techniques is that a velocity distribution must be assumed, whereas laser Doppler needs no assumption. Furthermore, movement artifacts cannot be filtered out by a high-pass filter like that of laser Doppler. However, laser speckle is inherently much faster than laser Doppler and can be implemented with an inexpensive low-frame-rate camera. Both laser speckle and laser Doppler techniques boast high compatibility with other techniques and are continuously compared in many reviews.[22,23,175] Still, these techniques gain contrast through structure, whether it be through refractive index (OCT), or particle flow (LDI and LSI). The following section will address techniques capable of functional imaging through mapping tissue optical properties.

2.3.4 Widefield Modalities for Mapping Optical Properties

There is an ever-expanding list of optical technologies capable of quantifying tissue optical properties and, by extension, tissue constituents through the detection of a remitted or transmitted light field. This detected light field is a function of space and time (Eq. 8), and so technologies rely on spatially-resolved or time-resolved measurements (see Fig. 2.3.1). For spatially- and temporally-resolved techniques several similarities

occur. First, both genres use reflectance and transmittance geometries for data collection, but it should be mentioned that reflectance is generally preferred in the clinic. Second, both are capable of using point or widefield measurements, though the ease for some techniques to be done in widefield is a great advantage. Finally, no matter the domain, there is always a tradeoff to be made in performance. For instance, any technique that boasts high spatial resolution will sacrifice temporal resolution. Minimizing these sacrifices in order to gain clinical utility is the goal for these modalities.

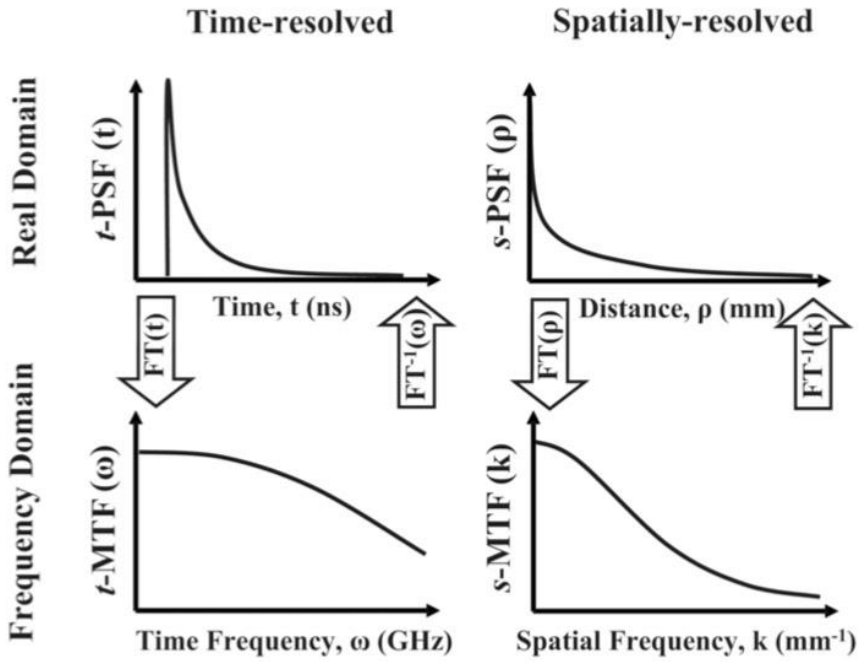

Figure 2.3.1: Measurement domains for characterizing turbid media - adapted from here.[35]

Time-resolved techniques rely on the measurement of the time-domain temporal point-spread function (t-PSF), i.e. the temporal spreading of pulsed light[183,193] or its Fourier transform equivalent in the frequency domain, the temporal modulation transfer function

(t-MTF), i.e. the attenuation and delay of temporally modulated photon density waves.[54,121,156] Time-domain instrumentation is typically expensive and complex,[11,141] though it has been used for early detection of breast cancer.[65] Point raster-scanning or multiple array acquisitions leads to long acquisition times impractical for real-time measurements, though strides are being made toward faster acquisition via charged couple device (CCD) detection.[31] The large dataset and extensive post-processing enables tomographic reconstruction of tissue optical properties, but is also prohibitively slow for real-time feedback. Finally, these robust time-domain techniques have been kept to pre-clinical imaging due to costly equipment.

Frequency-domain methods are typically less expensive and easier to use than time-domain instrumentation,[60] have reached clinical trials,[146] and are thoroughly reviewed here.[30] Diffuse optical spectroscopy imaging (DOSI) is an example of frequency domain technique, also called frequency-domain photon migration (FDPM). Though it has shown positive results for discerning healthy and diseased tissue in its clinical trials, it has yet to find its place as a standard-of-care in the clinic. Moreover, while some current frequency-domain methods can track tissue hemodynamics in real-time, few systems provide imaging and none can do both.

Similarly, spatially-resolved measurements belong to one of two domains: the spatial-domain (or continuous wave-domain), i.e. measuring the spatial point-spread function (s-PSF) at multiple distances[19,52] or its Fourier transform equivalent in the spatial frequency

domain, the spatial modulation transfer function (s-MTF), i.e. measuring the remitted light fields at several spatially modulated illumination patterns.[36,44] Just as the time domain relies on the temporal spreading of a light pulse, the spatial domain relies on the spatial spreading of a point source. For this reason, spatial-domain techniques require point-scanning (time/field of view prohibitive)[71,195,198] or a large source-detector array (resolution prohibitive)[17,32,76] to form an image map of optical properties, though are typically used for tomography.

Imaging in the spatial frequency domain is of particular interest for widefield mapping of optical properties in the clinic because it is inexpensive, easy to implement, and capable of mapping optical properties over large fields of view rapidly.[35,36] Briefly, because of the spatial low-pass filter characteristics of tissue, analyzing the frequency-dependent reflectance allows one to map the s-MTF (Fig. 2.3.1) and quantitatively obtain tissue optical properties. In order to separate the carrier signal from the sample-dependent signal, M_{AC}, standard processing requires acquisition of at least three phases for each spatial frequency of analysis. These three phases are required for each wavelength, and unless multispectral acquisition is employed, the number of acquisitions quickly adds up. Height correction should be implemented for accurate diffuse reflectance maps, though requires an additional three phases,[62] further compromising temporal resolution. By implementing a pre-calculated 2-D look-up table of Monte Carlo simulations, processing times for mapping optical properties from diffuse reflectance are minimal compared to other optical properties imaging methods, but still outside of real-time. However, with

advances in processing techniques, spatial-frequency domain methods have potential for providing real-time feedback.

2.4 Spatial Frequency Domain Imaging

2.4.1 Principles

A full tutorial on spatial frequency domain imaging (SFDI) can be found here.[35] Spatial-frequency domain imaging relies on the ability to extract diffuse reflectance as a function of spatial-frequency. In order to measure the diffuse reflectance, system-dependent components must be removed from the measurement. So, starting with an initial measurement of the remitted signal $I = I_{AC} + I_{DC}$, the AC component I_{AC} can be modeled as a sine wave with phase φ at location (x, y)

$$I_{\mathrm{AC}}(x, y, f_x, \varphi) = M_{\mathrm{AC}}(x, y, f_x) \cdot \cos(2\pi f_x x + \varphi) \tag{12}$$

where f_x is the projected spatial frequency and M_{AC} is the frequency-dependent modulation amplitude. Intuitively, M_{AC} is the measurement I_{AC} demodulated of the carrier frequency projected onto the sample. As mentioned, this can be acquired with through many processing techniques, but standard SFDI protocol uses a three-phase acquisition scheme, per frequency, per wavelength. The modulation amplitude is of interest because it can be related directly to diffuse reflectance R_d through the source intensity I_0 and the modulation transfer function of the optical system MTF_{sys}

$$M_{AC}(x, y, f_x) = I_0 \times \mathrm{MTF}_{sys}(x, y, f_x) \times R_d(x, y, f_x) \tag{13}$$

The spatial-frequency domain allows for easy separation of system components through division, as opposed to deconvolution in the spatial domain. A calibration measurement $M_{\mathrm{AC},\,ref}$ is made from a phantom with known optical properties to remove the instrument-dependent components, I_0 and MTF_{sys}, and a predicted diffuse reflectance measurement $R_{d,\,\mathrm{ref,pred}}$ is used for normalizing the calibration:

$$R_d(x, y, f_x) = \frac{M_{\mathrm{AC}}(x, y, f_x)}{M_{\mathrm{AC},ref}(x, y, f_x)} \times R_{d,\mathrm{ref,pred}}(f_x) \tag{14}$$

Hence, after calibration the modulation amplitude can be used to directly solve for the diffuse reflectance. A detailed derivation can be found here.[35] Figure 2.4.1 shows the dependence of diffuse reflectance on spatial frequency and optical property variations.

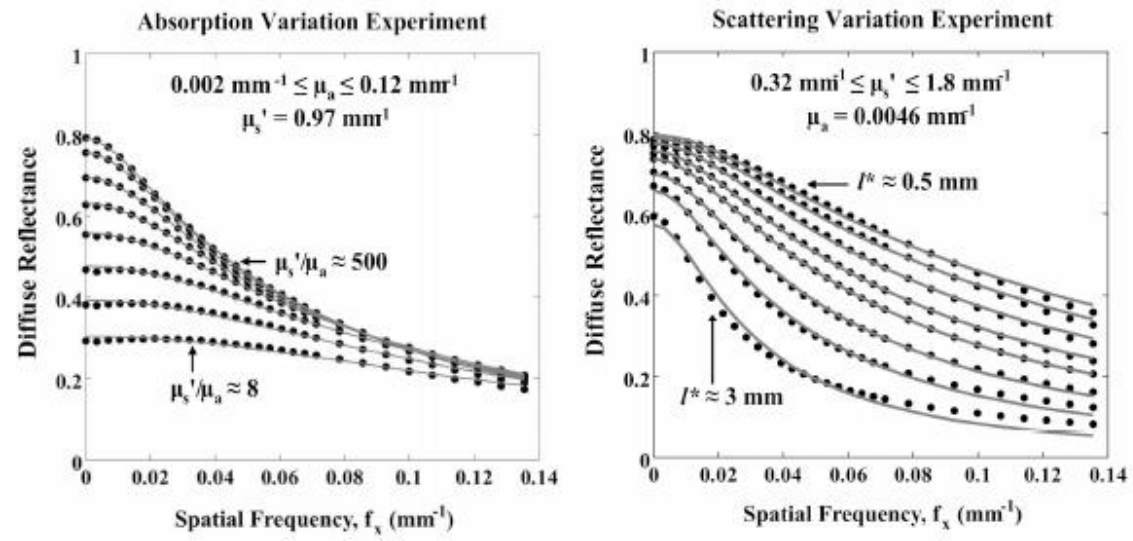

Figure 2.4.1: Diffuse reflectance frequency dependence with varying optical properties. Dots show experiment measurements made on phantoms, while the lines show Monte Carlo predictions - adapted from here.[35]

Figure 2.4.1 demonstrates the experimental validity of the standard SFDI. Experimental values (dots) show agreement with Monte Carlo predictions (lines) over a wide range of spatial frequencies and absorption and scattering coefficients. It should also be noted that low frequencies show sensitivity to both absorption and scattering, while high frequencies are mostly sensitive to scattering variations. These different dependencies provide a means to separate the two optical properties with as few as two spatial frequency measurements.[35] The most rapid processing methods to solve this final inverse problem employ a lookup table approach, by which solutions for diffuse reflectance are generated from a light propagation model (diffusion, Monte Carlo) or empirically with various spatial frequencies and optical properties.[35,124,132] A visual example of this two-dimensional look-up table can be seen in Figure 2.4.2, where the contour lines represent constant absorption and scattering. The contour lines in this example are very orthogonal, meaning that the optical properties can be extracted with maximum sensitivity. This is largely due to the large separation in DC and AC spatial frequencies used, 0 mm^{-1} and 0.5 mm^{-1}, respectively. The range of spatial frequencies in Figure 2.4.1 only reaches 0.14 mm^{-1}, but the most common spatial frequency pair used in experiments is (0 mm^{-1}, 0.15 – 0.2 mm^{-1}).

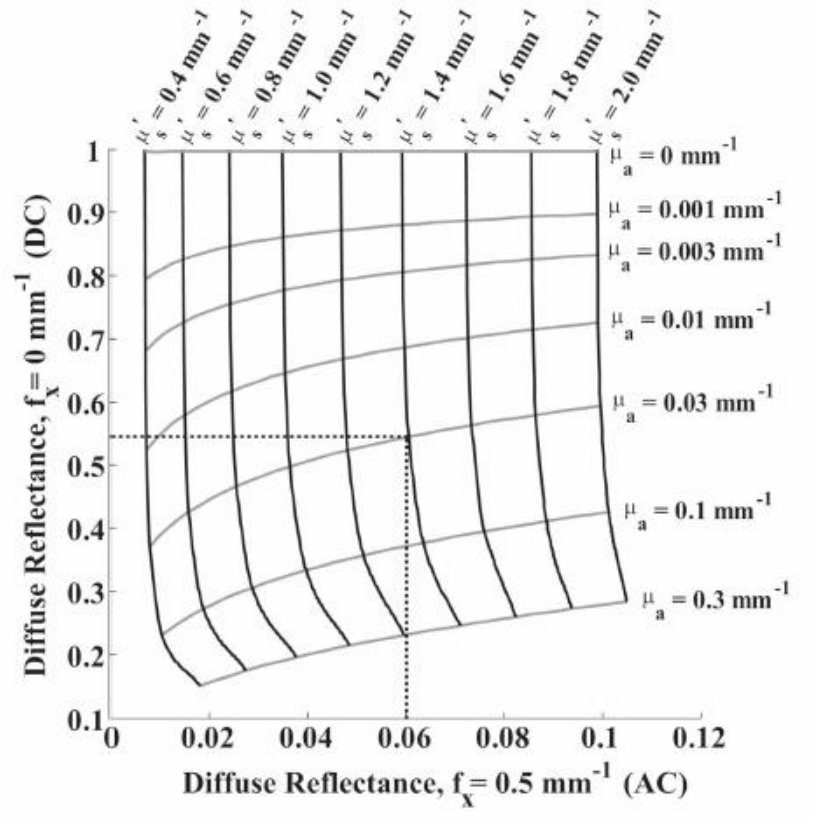

Figure 2.4.2: Two-dimensional look-up table for mapping diffuse reflectance to optical properties.[35]

2.4.2 System and Data Flow

In principle, all that is needed for SFDI is sinusoidal illumination and narrow-band wavelength imaging. To that point, work has been done to demonstrate the accessibility of SFDI, utilizing inexpensive consumer-grade equipment such as inexpensive light-emitting diode (LED) sources[39] or a common digital projector system for illumination.[150] A common format for the illumination and collection scheme in reflectance is shown in Figure 2.4.3. In short, a projection source and an imager are placed off-angle so as to limit specular reflections from the sample and to enable fringe profilometry for sample

profile measurement and correction.[62] Crossed polarizers further minimize collection of specular reflections, and either an emission filter or narrow-band source are used for optical property analysis.

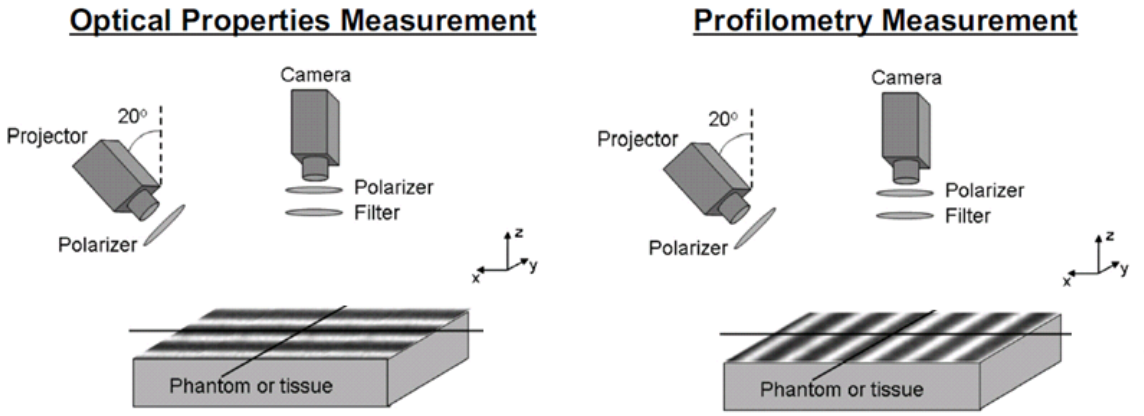

Figure 4.2.3: Schematic of a common SFDI system setup. Note that only two fundamental components, the projector and the camera, largely determine the cost and performance of the system – adapted from here.[62]

As visualized in Figure 2.4.4, each image I_i at each wavelength and spatial frequency f_x must be processed. First, it must be demodulated to calculate its modulation amplitude (Eq. 13), which is then calibrated to find its diffuse reflectance R_d (Eq. 14). Then, a data fitting, most commonly via lookup table (see Fig. 2.4.2), must be done to calculate optical properties μ_a and μ_s'. It should be noted that in order to calibrate the sample, another acquisition must be made on a reference phantom of known optical properties.

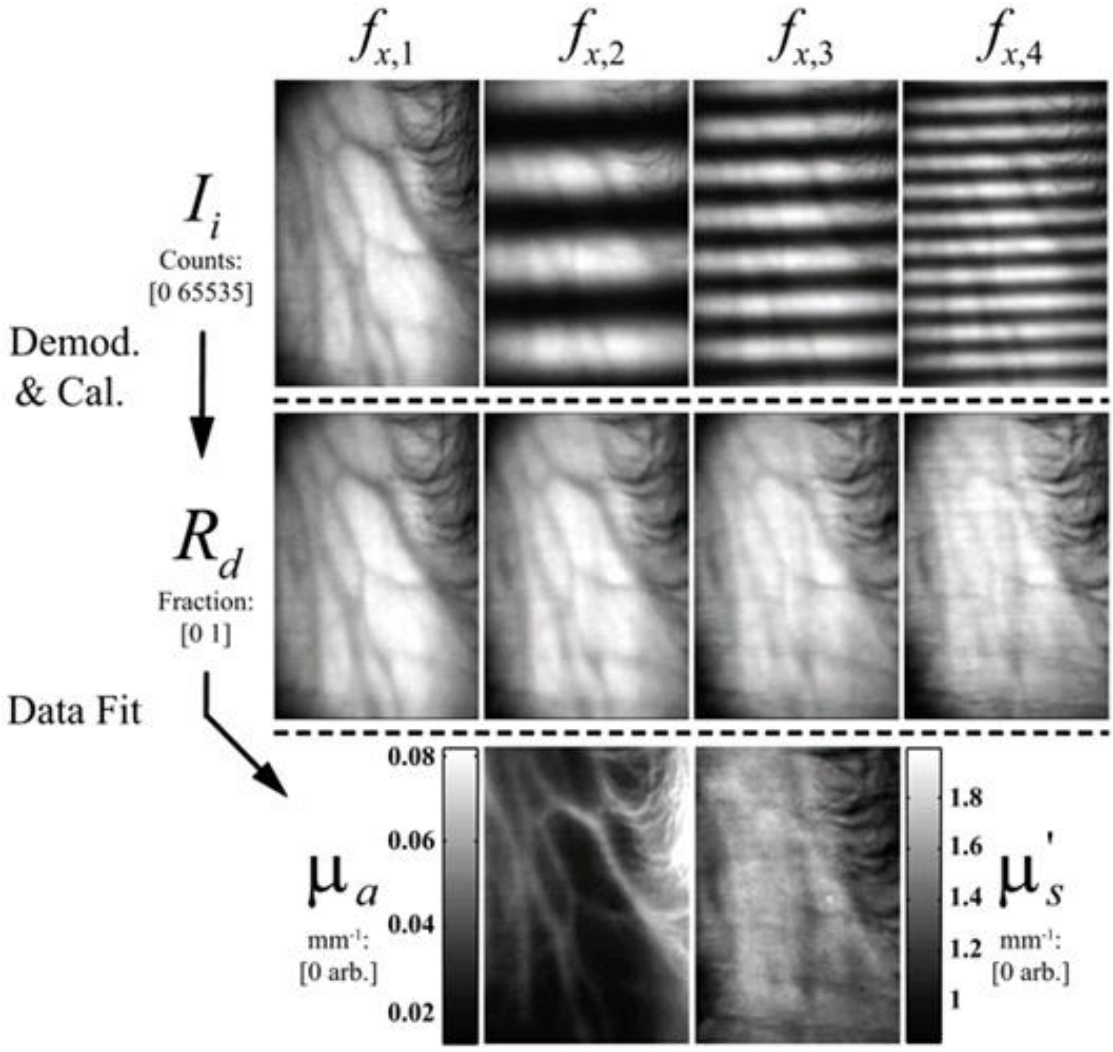

Figure 2.4.4: A visualization of the data flow dictated by the proposed principles in the previous section.[35]

With these fundamentals of theory and acquisition, there has been a flurry of activity around SFDI in the past 5 years. Several groups have aimed to push the robustness of measurement to include profile correction (See Fig. 2.4.5),[62,199] wavelength optimization for chromophore fitting,[106] tomographic imaging and depth sensing,[36,38,89,104] scattering orientation measurement,[90] and sub-diffuse sensitivity.[107] Others have aimed at achieving

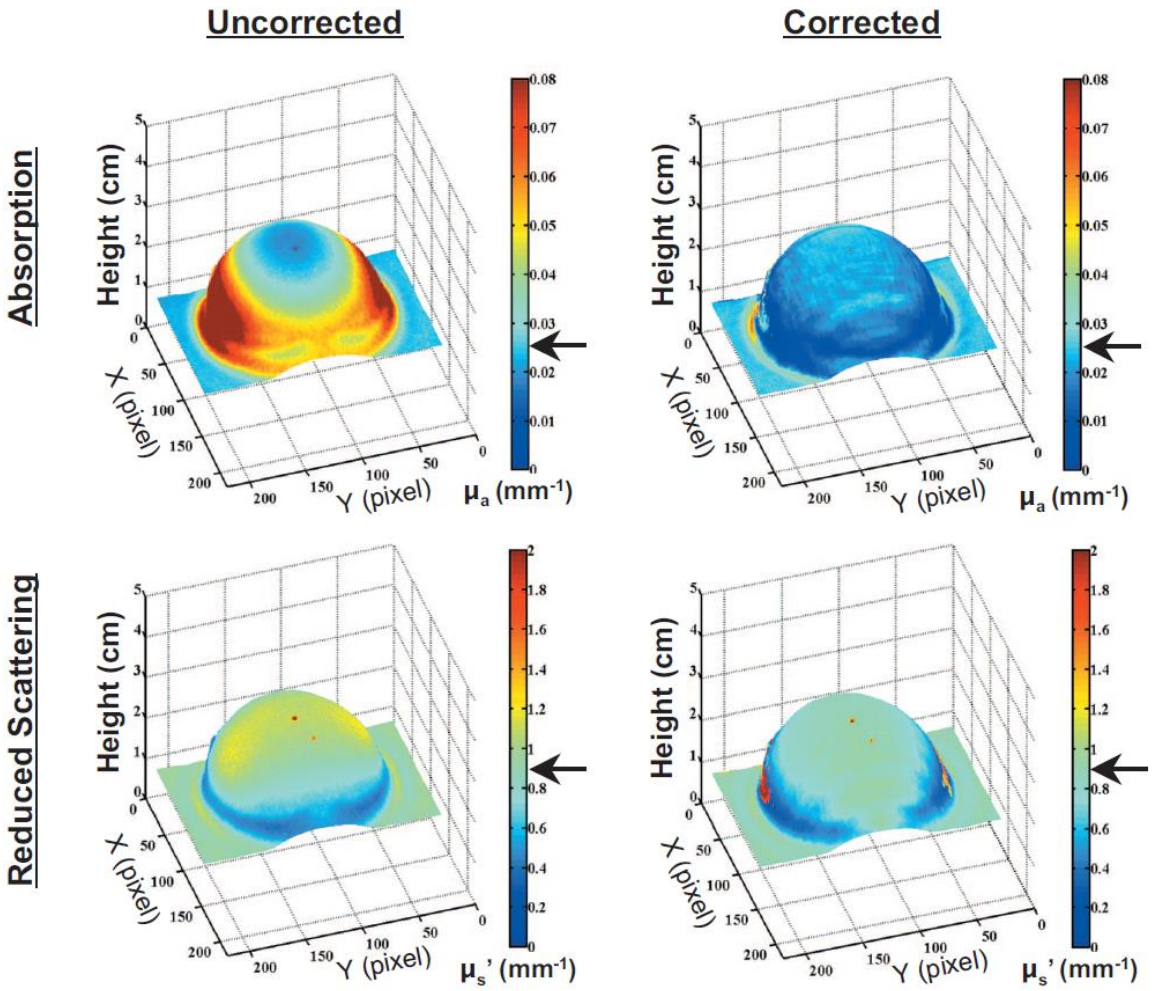

Figure 2.4.5: Demonstration of surface measurement and profile-corrected optical property measurements for SFDI.[62]

multi-modal measurements by utilizing SFDI's simple imaging requirements and combining it with polarization imaging,[190] speckle imaging,[105] and short-wave multispectral measurements.[185] So rapid this exploration has been that clinical and pre-clinical applications are already sought after in various capacities, such as burn wound assessment,[24,118] guidance for breast reconstruction,[63,120] monitoring of drug delivery,[150] and monitoring response to neoadjuvant chemotherapy.[158]

2.5 Single Snapshot of Optical Properties

By and large the literature has utilized SFDI's robustness and ease of implementation to build *onto* the existing platform while keeping its limitations, namely speed. With the potential to be utilized by nearly all of the above improvements and breakthroughs just mentioned, a reduction in acquisition time has the potential to bring these techniques utility as time is always precious in the clinic. Furthermore, as will be demonstrated in the remainder of this dissertation, it will allow implementation of widefield optical property imaging in ways previously thought impractical and sensitivity to a time-regime once thought impossible.

2.5.1 Demodulation via single sideband analysis

As previously mentioned, nearly all SFDI techniques require the acquisition of three phase images φ to perform a demodulation in order to remove the carrier signal and acquire the demodulation amplitude M_{AC}. Once this is done, various processing is done to calculate diffuse reflectance, optical properties, or other parameters. Note most end-goal calculations require multiple M_{AC} measurements, meaning that if four wavelengths at two spatial frequencies are required, then $4\lambda \cdot 2\, f_x \cdot 3\varphi = 24$ images are needed for a single measurement!

Recent progress has been made to reduce the three-phase acquisition dependence of standard spatial-frequency domain imaging.[115,177] Both methods utilize the power of the Hilbert transform and analytic functions for extracting wave envelopes of sinusoidal signals (See Fig. 2.5.1).

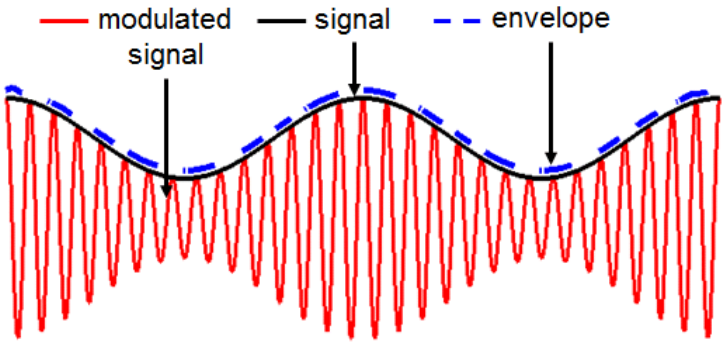

Figure 2.5.1: Signals considered in demodulation. The goal is to calculate the envelope of the modulated signal, effectively reconstructing the signal wave.

The following demodulation theory only works for a detected signal $u(t)$ with no DC component and is commonly known as single sideband (SSB) demodulation. Therefore both methods in question have ways of removing the DC component of $u(t)$, the red "modulated signal" curve in Fig. 2.5.1, which will be discussed shortly. First, the carrier wave $c(t)$ with frequency f_c modulates the signal $s(t)$, the black "signal" in Fig. 2.5.1, and shifts the Fourier spectrum of $s(t)$ to $\pm f_c$. This results in a detected signal $u(t) = s(t) \cdot c(t)$ (see Fig. 2.5.2). Again, in practice, the carrier signal will have a DC component. This component is neglected for the following analysis and will be addressed afterward.

The analytic function of $u(t)$ is formed thusly

$$u_a(t) = u(t) + iH\{u(t)\} \tag{15}$$

The Hilbert transform H rotates all positive frequencies of $u(t)$ by -90° and all negative frequencies by +90° in the complex frequency domain. Then, multiplication with i rotates

all frequencies by +90°, resulting in all positive frequencies being restored and negative frequencies being rotated 180 degrees with respect to their original orientation. Hence, the addition of $u(t)$ will 'constructively interfere' with all positive frequencies, resulting in a doubling effect, and a 'destructive interference' for all negative frequencies, resulting in their complete removal. In the context of signal detection, this new, complex function $u_a(t)$ is formed from a real-valued signal $u(t)$ by removing all negative frequency components. As the Fourier transform $F\{u_a(t)\}$ is shown in Fig. 2.5.2, this results in keeping only one of the so called 'sidebands' at $+f_c$. It is now helpful to write this complex signal $u_a(t)$ in polar coordinates:

$$u_a(t) = \tilde{u}(t)e^{i2\pi f_c t} \tag{16}$$

This is a very helpful insight, as this shows that one can view the analytic function $u_a(t)$ as a function $\tilde{u}(t)$, called the complex envelope, with frequency components centered at zero that are shifted with the complex exponential by frequency f_c. This shift can be followed in Fig. 2.5.2. Therefore, by simply taking the magnitude of $u_a(t)$ one can calculate $\tilde{u}(t)$. This brings the signal back to the baseband, effectively demodulating the detected signal $u(t)$ and calculating the sample signal $s(t)$.

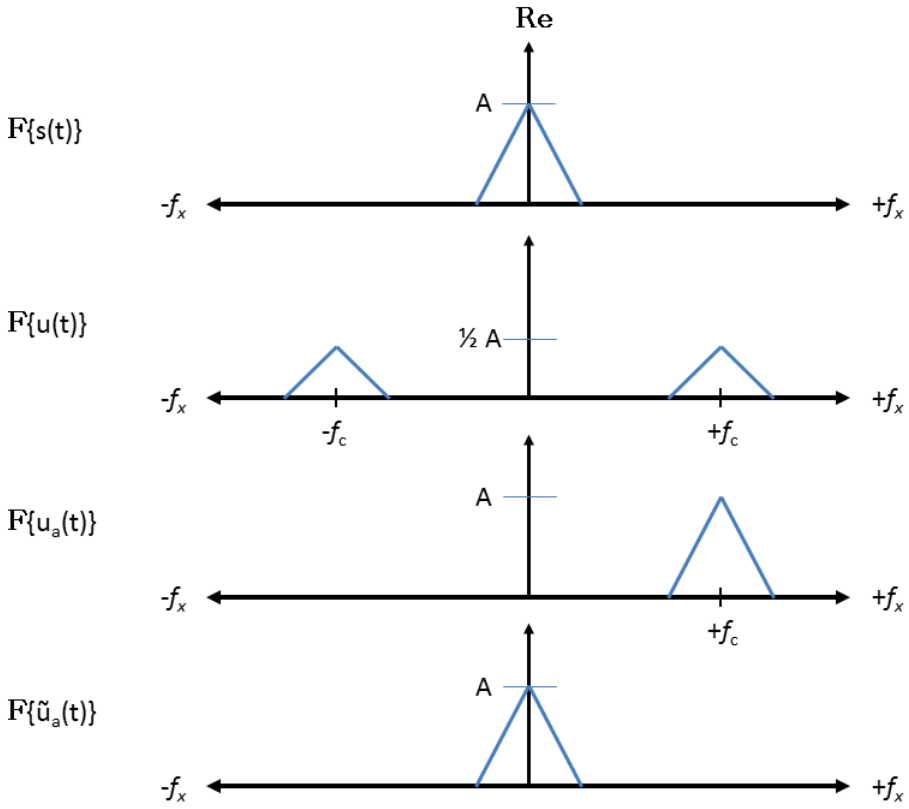

Figure 2.5.2: Frequency domain schematic following the modulation of a signal *s*(*t*) by +/- f_c into *u*(*t*), the nullifying of negative frequencies with $u_a(t)$, and the shifting to ~$u_a(t)$ to a center frequency of zero.

The method recently developed from Nadeau et al uses this SSB demodulation strategy in order to reduce the image capture requirements from six down to two, a three-fold improvement.[115] By acquiring a DC image separately from a combined DC + AC signal, the difference can be taken to remove the DC signal and the resulting AC signal can be demodulated using SSB analysis. This analysis requires a pure sinusoidal projection, but flicker rates of most digital micromirror device (DMD) projectors at 8 bits greatly inhibit the projection speed, hence limiting the possible framerate of collection. A benefit to their two-dimensional analysis is that the AC pattern can be oriented at any angle, which

is a consideration for the following technique. However, perhaps this convenience gained by rotational freedom does not outweigh the cost of synchronizing projection with collection as far as practical implementation of technique is concerned.

Single Snapshot Optical Properties (SSOP) imaging takes advantage of both DC and AC components of a single projected spatial frequency wave and effectively reduces the acquisition burden from six frames down to one. By taking the Fourier transform of each row of pixels along the remitted spatially modulated wave, the DC and AC reflectance components can be separated in frequency space to extract two spatial frequency images (see Fig. 2.5.3). In order to separate the DC and AC components, this method uses a minimum detection algorithm to find the optimal cutoff frequency once the spectrum is smoothed. After the spectrum is separated into two, each undergoes an inverse Fourier transform and then is demodulated using the SSB analysis (see Fig. 2.5.2) to acquire the AC and DC images seen in Fig. 2.5.3. From here, the images are then processed with the standard 2-D look-up table to create optical property maps.

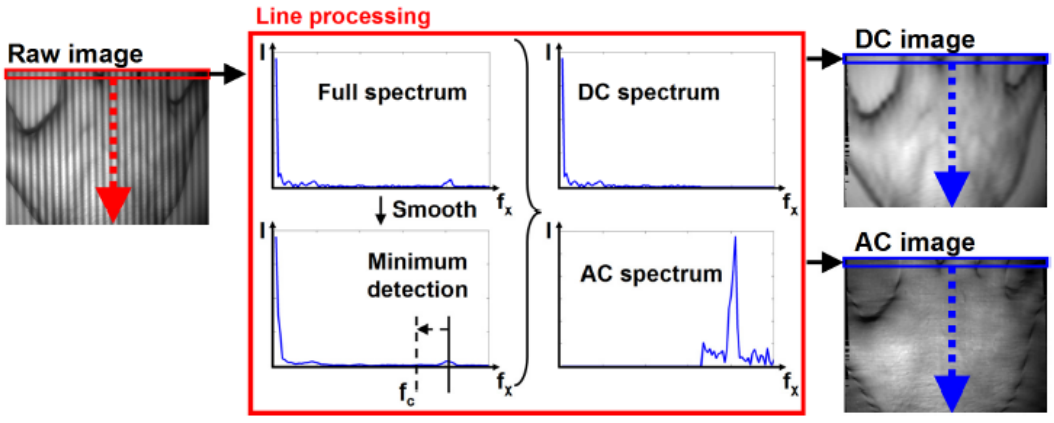

Figure 2.5.3: Single snapshot processing method that highlights the separation of DC and AC signals in Fourier space - adapted from here.[177]

This technique has effectively reduced acquisition times to that of a single exposure for mapping optical properties, hence its name. Note, improvements have been made to the Hilbert technique by Nadeau et al.[116] This allows for square wave projection, removing the original burden of 8-bit projection and its cost to speed. This analysis also allows for the harmonics of a spatial frequency to be analyzed as well, though creating a computational cost approximately an order of magnitude more than the original three-phase processing. However, any reported speed can effectively be doubled using SSOP given its single exposure advantage. Furthermore, square wave projection and harmonic analysis is compatible with SSOP as well. Recent developments of this technique, as demonstrated throughout this dissertation, support the already video-rate acquisition of SSOP by minimizing processing time, applying profile corrections, simplifying instrumentation, and combining multispectral measurements so as to provide real-time feedback for inexpensive, robust, quantitative surgical guidance.

CHAPTER 3: STRUCTURED ILLUMINATION FOR ENHANCED FLUORESCENCE IMAGING

Fluorescence image guided surgery has been shown to provide improved benefit to patients[8] (from qF-SSOP). Though there have been many developments for widefield, real-time fluorescence imaging, our lab has focused on two areas to broadly help fluorescence imaging become more effective for surgical guidance: depth sensitivity and quantitative corrections. In part 1, depth sensitivity is approached with a novel depth-enhanced imaging technique called masked detection of structured illumination (MDSI). This technique utilizes the diffusive nature of tissue to either focus on highly scattered, relatively deep fluorophores or less scattered, shallow fluorophores. Structured light and detection allows for system control and analysis that enables this selective process. Part 2 presents our real-time, quantitative fluorescence single snapshot of optical properties (qF-SSOP) technique that aims to correct for variations in fluorescence signal due to varying tissue optical properties. Sinusoidal projection enables spatial frequency domain processing for optical property measurements, bringing quantitative processing to real-time fluorescence imaging. In this chapter, structured illumination provides parametric control over spatial fluence that allows tailored light collection in MDSI and quantitative system analysis using qF-SSOP, making the future of fluorescence image guided surgery brighter.

3.1. Depth-enhanced Fluorescence Imaging using Masked Detection of Structured Illumination

The work in part 3.1 is published in the Journal of Biomedical Optics[5] with the following contributing authors:

Joseph Angelo,[1, 2] Vivek Venugopal,[1] Frederic Fantoni,[3] Vincent Poher,[3] Irving J. Bigio,[2] Lionel Herve,[3] Jean-Marc Dinten,[3] and Sylvain Gioux[1]

[1] Beth Israel Deaconess Medical Center, Department of Medicine, 330 Brookline Avenue, Boston, MA 02215, United States

[2] Boston University, Department of Biomedical Engineering and [4] Department of Electrical and Computer Engineering, Boston, MA 02215, United States

[3] CEA-LETI, Minatec Campus, Grenoble 38054, France

3.1.1 Introduction

Continuous wave reflectance imaging of exogenous fluorescence in turbid media is relatively superficial, with a maximum detection depth of 5 to 10 mm in the near-infrared (NIR), depending on the medium optical properties.[61] This limitation, in turn, strongly impairs the use of fluorescence imaging during in vivo applications in animals or in humans. For example, during the detection of sentinel lymph nodes in breast cancer,[160] fluorescence imaging performs as well as the detection of 99 Technetium-colloid except in high body mass index patients, where the presence of fatty tissue strongly limits the depth of detection to <2 to 3 mm.[3] Therefore, there is a strong interest in increasing the capabilities of fluorescence imaging to measure signals at depth. Two general approaches are taken to increase the sensitivity to fluorescence at depth. The first approach consists of using ultrasensitive detection technology, such as image intensifiers, intensified CCD,

or electron multiplying CCD.[61,145,201] The second approach relies on developing acquisition methods to enhance the sensitivity of fluorescence signals at depth. In this study, we chose the latter approach, since the price of the equipment can be a concern when using highly sensitive detection methods.

Several methods have been developed to perform depth-sensitive measurements within turbid media, each with its own fundamental limitations and benefits. Time- and frequency-domain reflectance methods require the acquisition of several sequential images, or raster scans, to collect a final depth-sensitive map.[127] This prolonged acquisition usually permits tomographic reconstruction at the cost of lengthy model-based processing. In the spatial domain, laminar optical tomography,[71,195,198] while mainly exploited for tomographic reconstructions, could be employed to perform depth-sensitive fluorescence imaging. However, the acquisition requires two-dimensional raster scanning, the field of view is relatively small, and post-acquisition image reconstruction is required. In the spatial-frequency domain, spatial frequency domain imaging has been used for depth-sensitive and tomographic applications over wide fields of view.[36,89,104] Still, an acquisition requires several images and post-processing to obtain depth-sensitive images.

In this study, we introduce a novel acquisition method called masked detection of structured illumination (MDSI) that is capable of preferentially enhancing the relative fluorescence signal at depth within a diffuse medium. This spatial-domain method relies

on the scanning of a collimated beam onto a diffuse medium and the physical masking of the point spread function (PSF) on the detection arm before acquisition on a CCD camera. By using instrumentation to preferentially collect diffuse photons at a chosen source-detector range, this method shows promise for enhancing fluorescence at depth within the medium. In the first section of this article, we describe the principle of the method and its implementation. In the following section, we present experiments to validate the approach using both digital and physical masks, by imaging fluorescence from various depths inside a tissue-mimicking phantom. Finally, we assess the performance of the method and its current implementation in highlighting deeper or more superficial fluorescence contrast.

3.1.2. Materials and Methods

3.1.2.1 MDSI Principle

The radial dependence of the backreflectance from a point source illumination in a diffuse medium has been widely described.[52] From a reflectance imaging perspective, the function that describes this radial dependence can also be called a PSF. This PSF is directly related to the photons' visitation histories between a source and a detector, i.e., the paths most traveled by the collected photons within the medium, often described as a banana-shape function or photon banana. Typically, as the source-detector separation increases, the mean depth of this visitation distribution also increases.[37] As the length of travel increases, photons are more scattered and absorbed by the medium and the PSF intensity decreases. Many studies have taken advantage of this phenomenon to measure

information at depth in a diffuse medium[126,203] or to characterize optical properties.[45] MDSI relies on this principle to preferentially select or reject photons by masking the PSF from a collimated illumination.[4,51]

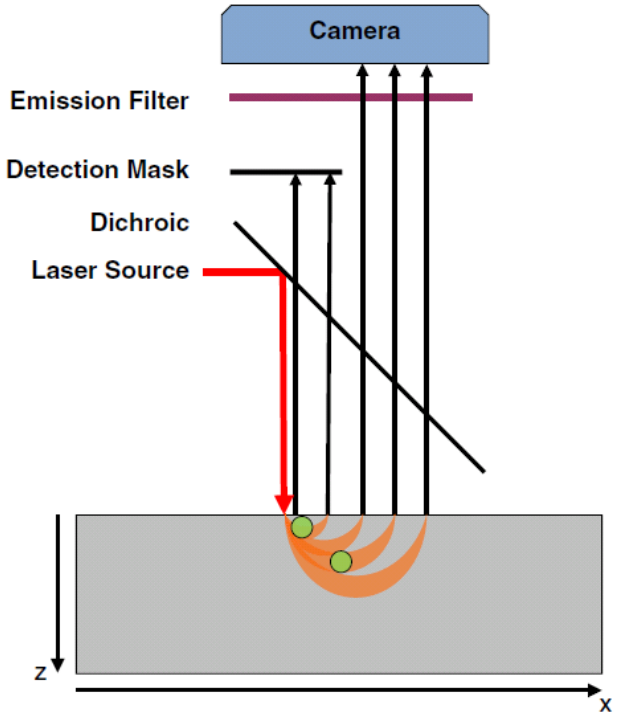

Figure 3.1.1: Masked detection of structured illumination (MDSI) — principle. A point illumination is shined onto a diffuse medium containing two fluorescence inclusions at different depths. Fluorescence is collected through the dichroic mirror and an emission filter in front of a camera. In this geometry, the shallow fluorescent inclusion is optimally excited at shorter source-detection separations and the deeper inclusion at larger source-detection separations. MDSI introduces a mask that preferentially selects the most diffused photons and, therefore, the deeper inclusion in the diffuse medium.

As shown in Fig. 3.1.1, a laser source is collimated, reflected by a dichroic mirror, and directed onto a diffuse medium (shown in gray). Fluorescence images are formed on a camera through the dichroic mirror and rejecting the excitation light with an emission filter. If two fluorescent inclusions (in green) are present within the medium at different depths and the detection system is scanned across the medium, shorter source-detector

separations will excite fluorophores at shallower depth, while longer source-detector separations will excite fluorophores at deeper depths. Therefore, by using a physical mask to block a range of short source-detector separations on the detection path of the system, contributions of deeper fluorophores will be relatively highlighted. Similarly, a different mask can be used to block the longer source-detector separation and highlight the contribution from shallower fluorophores (not shown in Fig. 3.1.1).

MDSI relies on this core principle to preferentially enhance deeper or shallower contributions to the fluorescence signal. To interrogate the entire medium, and, therefore, form a depth-enhanced fluorescence image, the laser illumination is scanned at regular intervals across the surface of the medium while keeping the mask always centered on the illumination, and images are collected by the camera. One image is acquired per scan location, and all acquired images are summed at the end of the scan to form a final, depth-enhanced fluorescence image.

In this study, we present a possible embodiment for a setup capable of performing the described MDSI and report test results of its performance on the bench.

3.1.2.2 System Design

An experimental challenge in building a setup capable of performing MDSI is to guarantee that the physical mask is always centered on the illumination location in the detection path, regardless of the scan position. To achieve this, we built the setup shown schematically in Fig. 3.1.2. The source is collimated and then directed onto the sample

using a mirror (M_s) that scans the beam over the medium. A first two-lens relay system (L_1, L_2) is used to relay the image plane from the sample surface to the mask location through the scanning mirror. This guarantees that the illumination is always centered on the physical mask. A second two-lens relay system (L_3, L_4) is used to relay the masked image back onto the sensor of a CCD camera and de-scan it to the correct location through a rotating mirror (M_d) that is synchronized with the first scanning mirror. In summary, as the first scanning mirror samples the surface of the medium, the center of the illumination is always at the center of the mask plane, and the resulting masked image is directed to its correct location using the second rotating mirror. In this proof-of-concept implementation, the source was shaped as a line, and the scanning was performed along one dimension only.

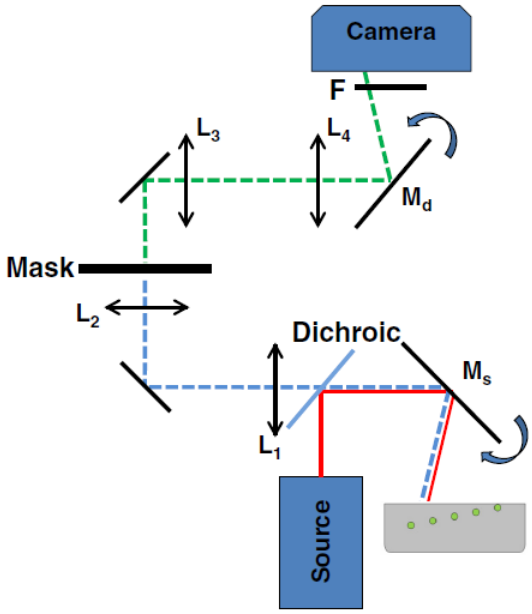

Figure 3.1.2: MDSI—schematics. A source shines a collimated line illumination on the medium via a dichroic mirror and a scanning mirror (M_s). This mirror scans the line illumination over the medium and an image of the fluorescence is formed at the mask plane using a two-lens relay (L_1 and L_2). Note that through this geometry, the illumination is always centered onto the mask plane. An image of the mask plane is formed onto the CCD camera sensor using a two-lens relay (L_3 and L_4) and a de-scanning mirror (M_d) that replaces the masked image at the correct location onto the CCD sensor.

3.1.2.3 Data Acquisition and Processing

In this study, the sample used was a tissue-mimicking, silicone-based phantom having fluorescent tubes at different depths and optical properties of μ_s' = 1 mm^{-1} and μ_a = 0.01 mm^{-1}. Titanium dioxide was used as a scattering agent and India ink as an absorbing agent.[10,128] As shown in Fig. 3.1.3, a total of five capillary tubes were embedded within the sample, separated progressively by 1 mm in depth at 1 cm intervals, tube 1 being most superficial and tube 5 being the deepest. Each tube was ~1 mm in diameter. The capillary tubes were filled with FHI-7206 (Fabricolor Holding, Paterson, New Jersey) in dimethyl sulfoxide at a concentration of 3 μM. This dye's maximum absorption is at 720 nm and the emission is strongest at 750 nm, though it continues out to 850 nm. FHI-7206 was chosen because it proved more stable in preliminary testing than other common dyes. Tube depths were sampled individually with the same procedure.

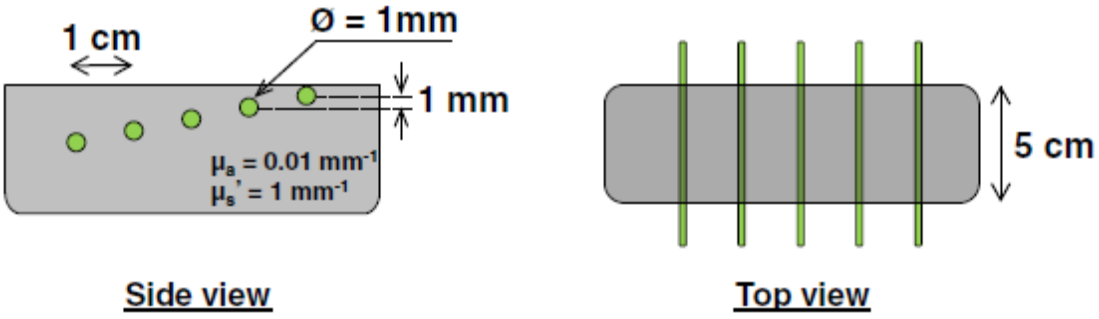

Figure 3.1.3: Schematics of the phantoms used during the experiments. Five capillary tubes are embedded at different depths into a silicon- based tissue-mimicking phantom. Each tube is separated by 1 cm laterally and 1 mm in depth, and is filled with FHI-7206 in dimethyl sulfoxide at a concentration of 3 μM.

The illumination line was scanned over the sample with 0.25 mm steps. First, a calibration run was performed to synchronize the two rotating mirrors. Following the calibration run, a rapid scan was performed on a homogenous sample to calibrate the camera exposure to collect enough signal at all scan locations (>3000 counts on a 12-bit camera). Finally, the sample was scanned and each image normalized by its optimized exposure before summation. Two types of acquisitions were performed, either with no physical mask (no-mask acquisition) or with a physical mask (mask acquisition) in the detection path of the system. Two types of masks were tested, either center passing or center blocking.

3.1.2.4 Simulation Experiments

The concept of MDSI was first tested by simulating the effect of masks onto a no-mask acquisition. Digital masks were created by extrapolating real physical mask profiles to the desired shape or size. Digital masks of blocking width from 0 to 7 mm were used for the center-blocking design, and from 2 to 12 mm passing width for the center-passing design. Following a no-mask acquisition, exposure-normalized images were masked using a digital mask and then summed together.

3.1.2.5 Validation Experiments

To validate MDSI, masked images were formed using mask acquisitions (i.e., with a physical mask) and summing the individual exposure-normalized images together. Real

masks of 6 mm blocking width (for the center-blocking design) and 3 mm open width (for the center-passing design) were fabricated and tested.

3.1.3 Results

3.1.3.1 MDSI System

Figure 3.1.4 shows an actual photograph of the experimental setup. For the source, a 660 nm 1-W 9-mm laser diode (LDX-3115- 660, LDX Optronics, Maryville, Tennessee) was mounted in a temperature-controlled laser diode mount (TCLDM9, Thorlabs, Newton, New Jersey). The laser diode temperature was controlled using a thermoelectric cooler controller (TED200C, Thorlabs) and the intensity using a diode current controller (LDC220C, Thorlabs). The line illumination was formed using a combination of a 50 mm focal length biconvex lens, a 500 mm focal length biconvex lens, and a cylindrical lens having a 3.8 mm focal length. The dichroic mirror used was a 2 in. × 2 in. 770 nm long-pass interference filter (Chroma, Bellows Falls, Vermont). The scanning was accomplished using standard 2 in. × 2 in. silver mirrors mounted on stepper motors (HT11-012, Applied Motion, Watsonville, California) and controlled with stepper motor controllers (1240i, Applied Motion). The first two-lens relay system was built using a 50-mm-diameter lens having a 300 mm focal length (L_1) and a 50-mm-diameter lens having a 75 mm focal length (L_2). The second two-lens relay system comprised a 50-mm-diameter lens having a 100 mm focal length (L_3) and a 50-mm-diameter lens having a 75 mm focal length (L_4). Center-blocking masks were made from aluminum shims, while

center-passing masks were based on a mechanically variable slit (VA100/M, Thorlabs). Finally, the camera used was a monochrome 12- bit cooled CCD (Hamamatsu Orca-ER, Bridgewater, New Jersey) and the emission filter a 25-mm-diameter 795 nm long-pass interference filter (HHQ795LP, Chroma).

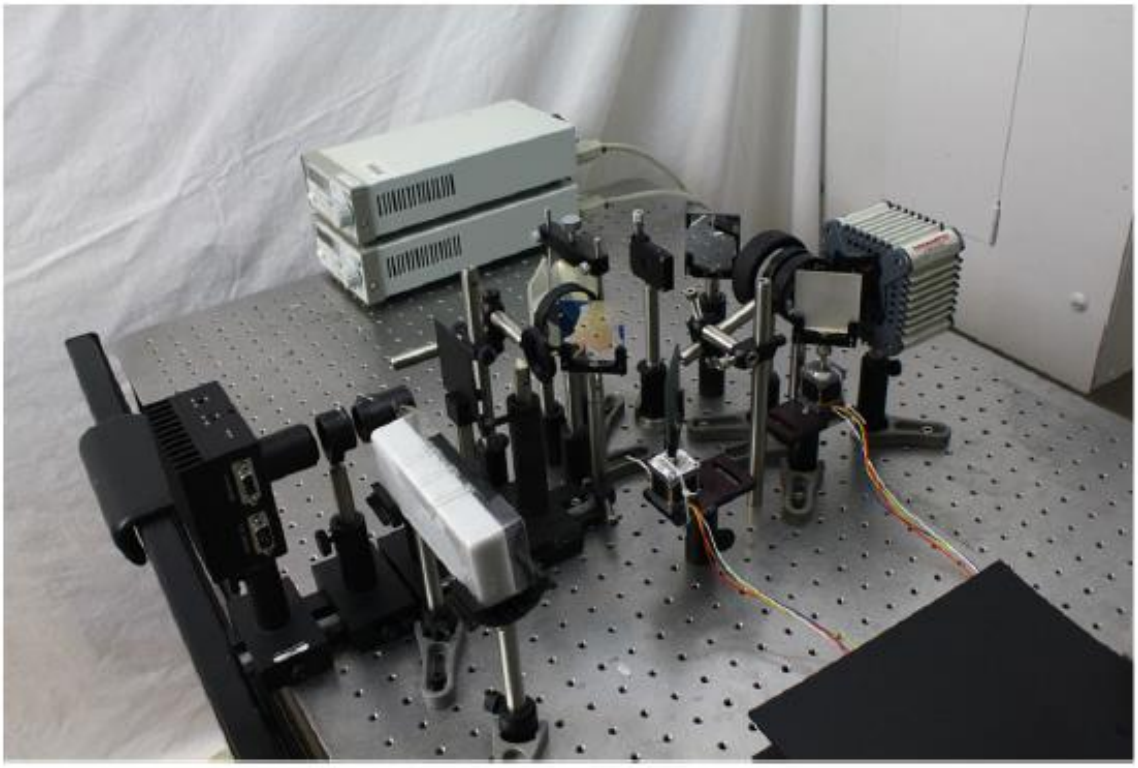

Figure 3.1.4: Photograph of the MDSI setup. As shown in the schematics in Fig. 3.1.2, a source shines a collimated beam through a dichroic mirror and a scanning mirror. An image of the phantom is formed at the mask plan and a secondary image for the masked phantoms reformed on the CCD sensor.

Shown in Fig. 3.1.5 are sample images and corresponding line profiles taken during a mask acquisition (center-blocking design) of a single tube, as well as the resulting summed image using the MDSI system. As anticipated, both the images and line profiles

clearly show the overlapping illumination and real mask scanning over the tube containing the fluorophore.

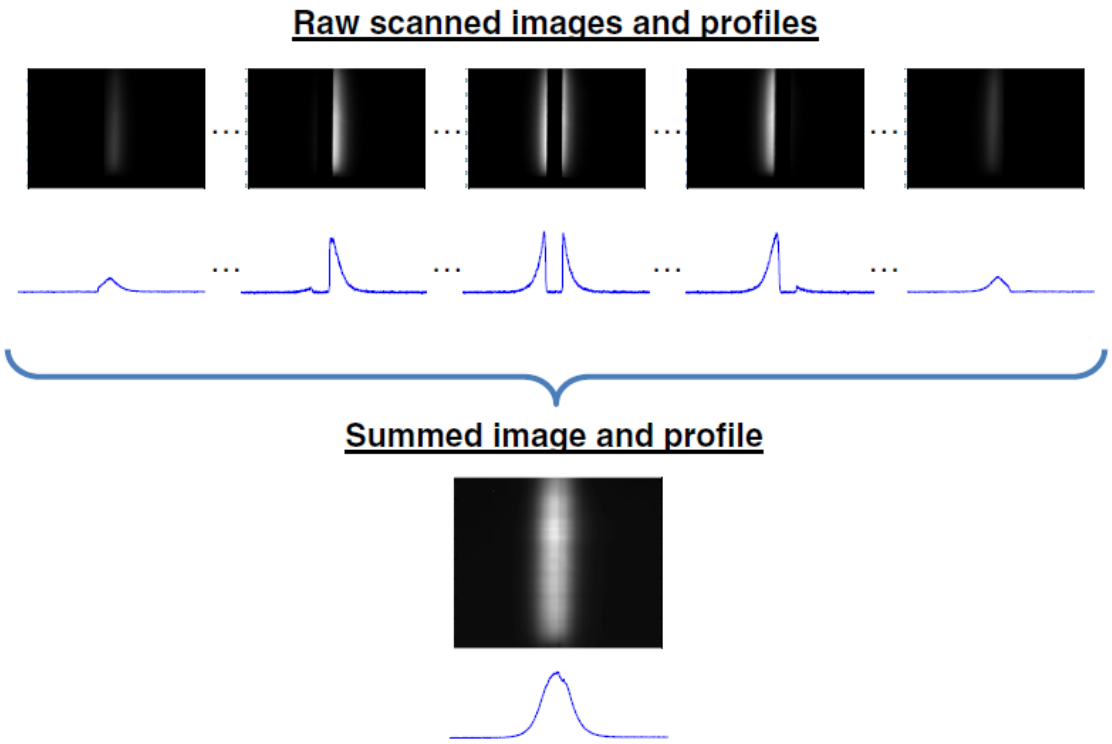

Figure 3.1.5: Sample images and corresponding profiles obtained with the MDSI setup. As the illumination scans the medium, the mask (center blocking) is centered on the illumination and blocks the less diffused photons. The summed image is formed by individually summing all masked images.

3.1.3.2 Center-Blocking Simulation Experiments

In this experiment, several digital center-blocking masks of varying size, from 0 to 7 mm blocking width, were applied to no-mask acquisitions. As illustrated in Fig. 3.1.6(a), for a fixed 6-mm real mask size, the fluorescence from shallower tubes is relatively more attenuated compared to deeper tubes, showing a relative enhancement of fluorescence signal at depth. To quantify this effect, the ratios of the peak for a given digital center-

blocking mask scan to that of the no-mask case were simulated at various mask sizes without averaging, and are shown in Fig. 3.1.6(b). Going from a 0-mm mask (i.e., no-mask) to a 7-mm mask, the peak signal for tube 1 decreases by 76%. Similarly, peaks for tubes 2, 3, 4, and 5 exhibit decreases by 70, 64, 60, and 54%, respectively, demonstrating less attenuation for deeper signals. In addition, a broadening of the profiles (demonstrated in Fig. 3.1.6(a)) is noticeable as the mask size increases, which is consistent with the fact that a greater proportion of diffused photons is collected. This broadening is characterized by the full-width at half-maximum (FWHM) of the emission line profiles for digital masks and is shown in Fig. 3.1.6(c). The percent increase in FWHM from a no-mask scan to a 7-mm center-blocking scan is 100, 100, 77, 62, and 50% for tubes 1, 2, 3, 4, and 5, respectively. In addition, results obtained with the 6-mm center-blocking real mask are plotted in Figs. 3.1.6(b) and 3.1.6(c) (x's) for comparison with the digital mask data.

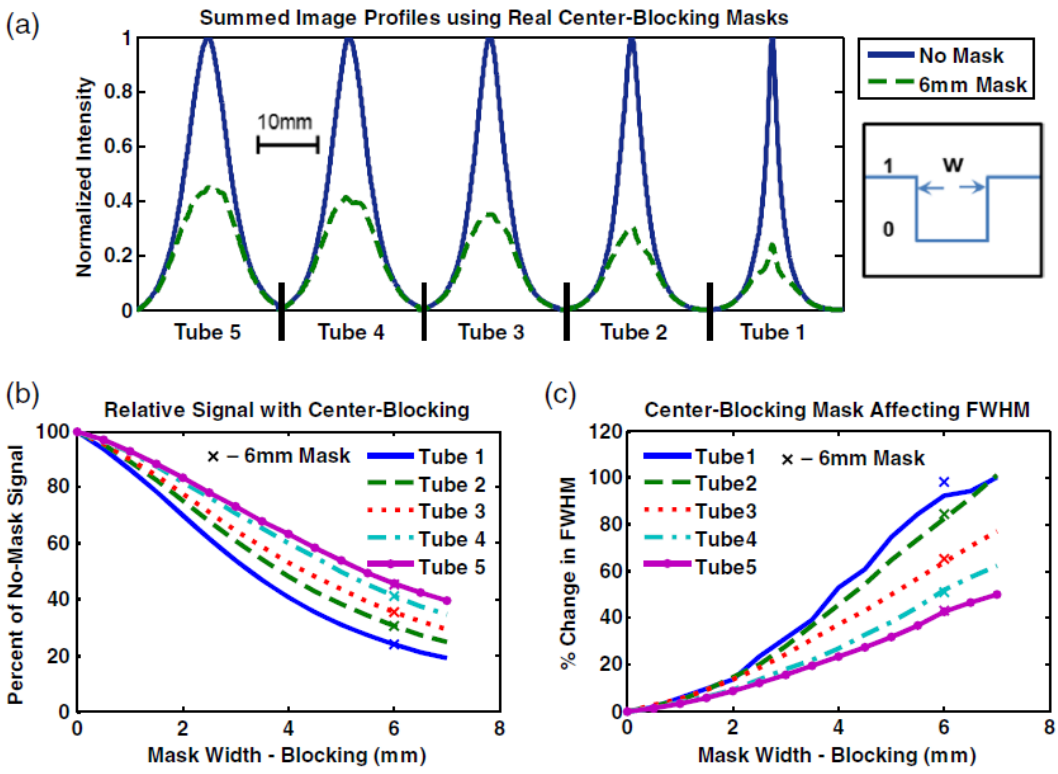

Figure 3.1.6: Center-blocking mask results. (a) compares the summed images profiles for the no-mask scan and the real 6 mm mask scan. Note the relative signal and full-width at half-maximum (FWHM) increase for deeper tubes when the center-blocking mask is used. Digital mask simulations (lines) demonstrate this effect showing (b) the relative signal increase and (c) the FWHM with increasing blocking width and tube depth, along with the real 6 mm mask scans (x's).

3.1.3.3 Center-Passing Simulation Experiments

In this experiment, several digital center-passing masks of varying sizes from 12 to 2 mm width were applied to no-mask acquisitions. As shown in Fig. 3.1.7(a), for a fixed 3-mm real mask size, the fluorescence from deeper tubes is relatively more attenuated compared to shallower tubes, showing a relative enhancement of the fluorescence signal at the surface. To quantify this effect, the ratios of the peak for a given digital center-passing mask scan to that of the no-mask case were simulated at various mask sizes, without

averaging, and are shown in Fig. 3.1.7(b). Comparing results from the no-mask [Fig. 3.1.7(b), asterisk] to a 2-mm mask, the peak signal for tube 1 decreases by 63%. Similarly, peaks for tubes 2, 3, 4, and 5 exhibit decreases of 69, 71, and 77%, respectively, demonstrating more attenuation for deeper signals. In addition, a narrowing of the image profiles is noticeable as the mask size decreases, which is consistent with the fact that a greater proportion of diffused photons is rejected. This narrowing is characterized by the FWHM and is shown in Fig. 3.1.7(c). The decrease in FWHM is 19, 25, 33, 21, and 28% drop for tubes 1, 2, 3, 4, and 5, respectively. In addition, the no-mask condition (asterisks) and the 3 mm center-passing physical mask (x's) results are plotted in Figs. 3.1.7(b) and 3.1.7(c) for comparison with the digital mask data.

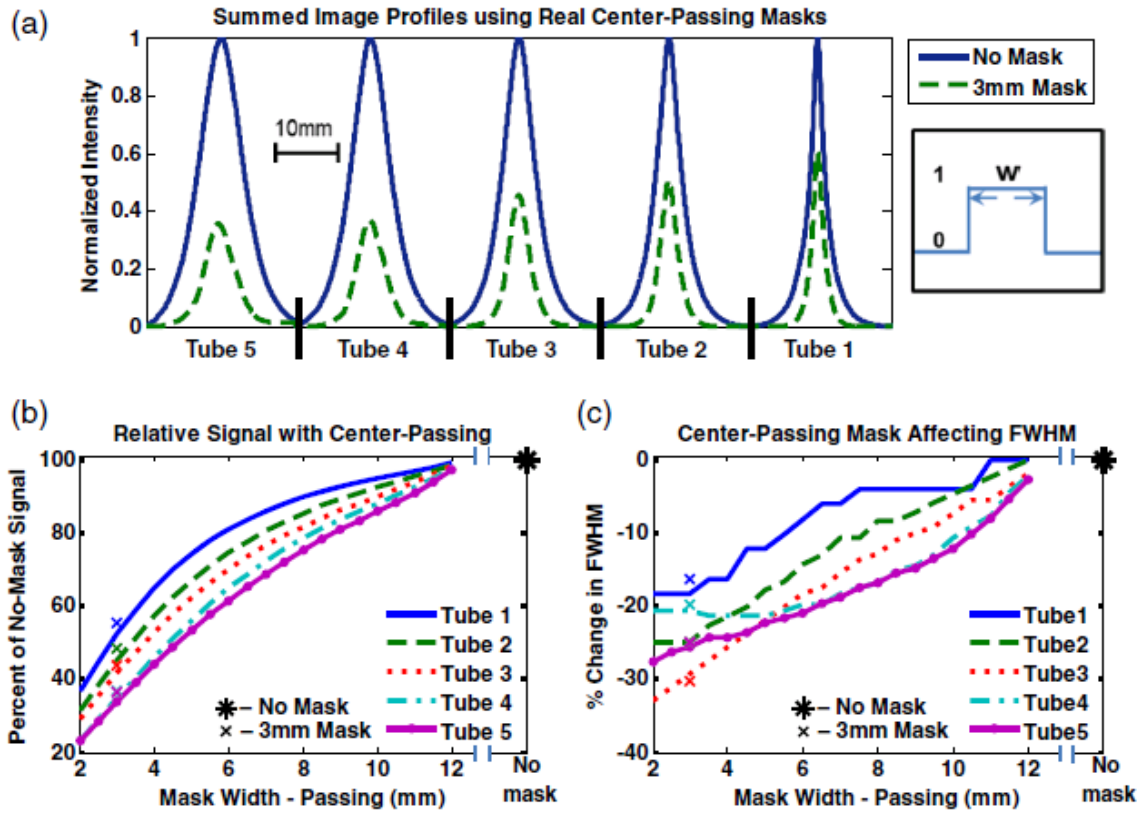

Figure 3.1.7: Center-passing mask results. (a) compares the summed images profiles for the no-mask scan and the real 3 mm mask scan. Note the relative signal and FWHM decrease for deeper tubes when the center-passing mask is used. Digital mask simulations (lines) demonstrate this effect by showing (b) the relative signal decrease and (c) the FWHM with decreasing passing width and tube depth, along with the real 3 mm mask (x's) and no-mask (asterisks) scans.

3.1.3.4 Validation Experiments

A set of summed images obtained with no mask, a real 6 mm center-blocking mask, and a real 3 mm center-passing mask is shown for all tubes in Fig. 3.1.8. Each row of images is normalized to tube 1 of the row. Line profiles for center-blocking and center-passing masks are normalized by and compared to the no-mask case in Figs. 3.1.6(a) and 3.1.7(a), respectively. Again, it is evident that the relative effect on deeper, more diffused signals

is less for center-blocking scans and more for center-passing scans. As evidenced in the previous experiments (Secs. 3.1.3.2 and 3.1.3.3), compared to a no-mask acquisition, the center-blocking mask shows more diffuse images with higher levels of fluorescence at deeper locations. The center passing, conversely, shows less diffuse images with lower fluorescence levels.

Results obtained with these validation experiments were compared to simulations performed previously and indicated in plots in Figs. 3.1.6(b), 3.1.6(c), 3.1.7(b), and 3.1.7(c). Overall, they show good agreement with the simulation data.

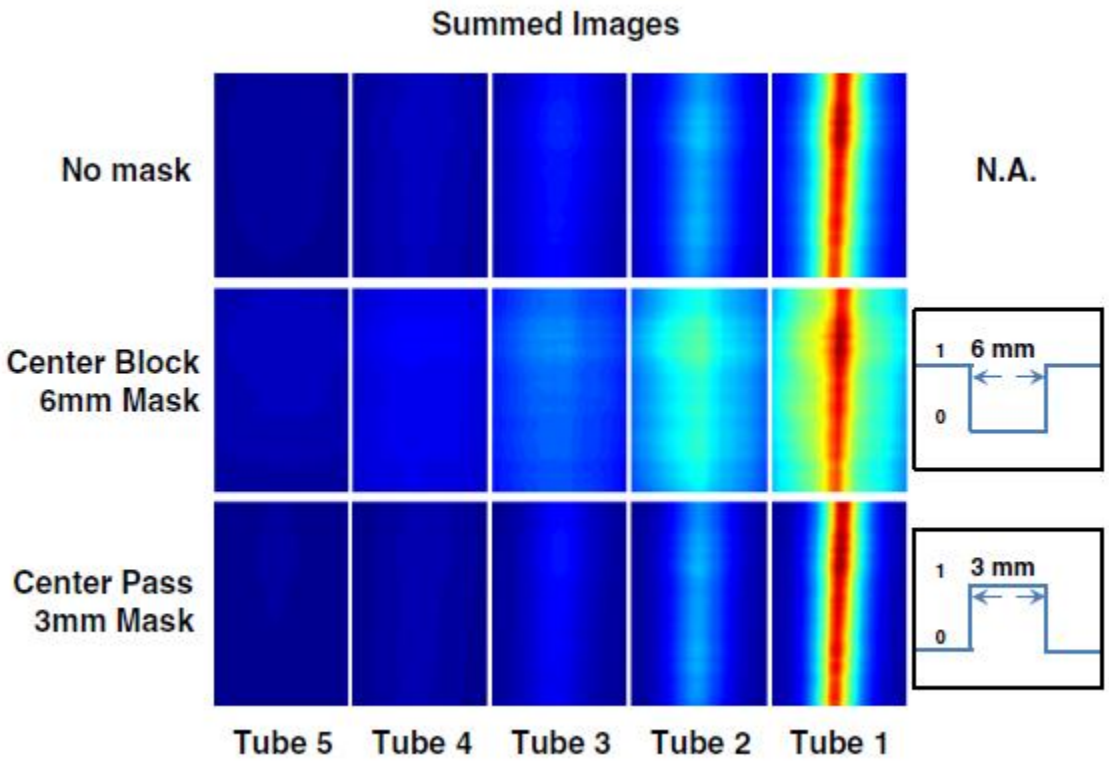

Figure 3.1.8: Images for all tubes formed by physically masked scans. The blurring and signal enhancement is apparent between the no-mask case and the center block 6 mm mask case. Likewise, sharpening and signal decrease is apparent for the center pass 3 mm mask case.

3.1.4 Discussion

In this study, we introduce and validate a novel acquisition method, called MDSI, taking advantage of the diffusion of photons within a turbid medium to preferentially enhance fluorescence signal as a function of depth in an imaging geometry. In this particular embodiment, the method enables performance of depth-enhanced fluorescence imaging without any post-processing, simply relying on an optical arrangement to either mask or select diffuse photons in a scanning geometry.

We investigated the effect of different mask sizes and shapes. Because the selection of the mask is of paramount importance with MDSI, a large body of work remains to be completed by studying different mask shapes and understanding their effects. In addition, the current implementation is focused on fluorescence imaging, but because MDSI highlights diffusion effects, it is anticipated that this method could also be used without fluorescence to highlight changes in absorption and/or scattering without post-processing.

The phantom used in this study consists of tissue-simulating material without autofluorescence since the motivation for this study was to prove the potential of MDSI for signal depth enhancement. In our case, in the NIR range around 800 nm, tissue autofluorescence in living tissues is particularly low[55] and should not present any concern. However, if this technique is applied to lower wavelengths, where autofluorescence becomes significant, such as <700 nm, this method may be prone to collect nonspecific diffused fluorescence, which would lower its performances.

Some of the limits concerning signal depth and mask size were reached in this study. Though the percent change in relative signal increases with increasing center-blocking mask width for each tube (see Fig. 3.1.6(b)), the absolute signal also decreases (Figs. 3.1.6(a) and 3.1.8). Tube 1's signal decreases faster than deeper tubes' signals, but exposure time and signal noise become a concern when using wide masks with deeper tubes. For the center-passing mask case, mask widths narrower than 3 mm tend to create sampling artifacts, causing the relative signal to fluctuate and seem non-monotonic. These sampling artifacts can be avoided by using a higher spatial sampling. Finally, the center-pass effect of narrowing a signal's FWHM for the deepest tubes (4 and 5) begins to diminish at ~5 mm masks or smaller. This is thought to be due to the absolute signal of these deeper tubes reaching the noise floor. All measurements were made on a homogenous phantom, and the performance of this method on heterogeneous media will be the topic of future investigation.

One of the limitations of the current setup is a long acquisition time due to a calibration run followed by data acquisition, all in a step-by-step scanning manner. More particularly, the current setup has the disadvantage of keeping the collimated laser line at the same position for a long time. This causes the fluorescence signal to bleach over time and is the reason behind the choice of laser dye, which is more stable in these conditions. However, the current setup acquisition is not optimized, scanning could be performed more rapidly, and the source could be synchronized with the image acquisition. Also, the development of a continuously scanning instrument would eliminate this effect.

A strong motivation for developing MDSI is the potential to provide rapid (near to real time) depth-enhanced fluorescence imaging. As detailed above, the current system relies on a step-by-step scanning approach, requiring post-acquisition summation of the images and rendering the acquisition slow. Because MDSI relies only on masked scanning of the medium without post-processing, it is possible to add a continuously rotating polygonal mirror along with continuous acquisition on a CCD camera for real-time summation of masked images and, therefore, real-time depth-enhanced fluorescence imaging.

The similarity of MDSI to other diffuse optics techniques has been described above. Some similarities can be seen between MDSI and microscopy techniques such as confocal microscopy, but the techniques function according to different principles. MDSI relies on highly scattering media in order for the structured illumination to propagate diffusely and to sample select depths on average according to the source-detector separation. Sufficient scattering is necessary for MDSI to work, whereas most microscopy techniques suffer greatly from noise due to light scattering within the sample.

3.1.5 Conclusion

In this study, we introduce and validate an acquisition method, called MDSI, allowing performance of depth-enhanced fluorescence imaging from a diffusive medium without post-processing. We present a proof-of-concept instrument and perform simulation experiments using digital masks to investigate the effect of mask size and shape, as well as validate MDSI capabilities with a physical blocking and passing masks. In summary,

this study lays the foundation for the development of a rapid in vivo depth-enhanced fluorescence imaging method without post-processing.

3.1.6 Acknowledgments

The authors would like to thank John V. Frangioni and Caroline Boudoux for many helpful discussions. We would also like to thank David Burrington, Jr. for editing and Eugenia Trabucchi for administrative assistance. This work was supported by NIH/ NCATS Award Number 8 UL1 TR000170-05 to Harvard Clinical and translational Science Center, collaboration Award Number 027343.386541.05226, and NIH/NIDDK Award Number K01-DK-093603. Joseph Angelo was supported by a National Science Foundation Graduate Research Fellowship under Award Number DGE-1247312.

3.2 Real-time Optical Property Corrected Fluorescence Imaging using Quantitative Fluorescence Single Snapshot of Optical Properties Imaging

Much of the work in part 3.2 has been presented and published through SPIE[163] with the following contributing authors:

Pablo A. Valdes,[1]* Joseph Angelo,[2,3,]* and Sylvain Gioux[3,4]

[1] *Harvard Medical School, Brigham and Women's/Boston Children's Hospitals, Department of Neurosurgery, Boston, MA 02115, United States*

[2] *Boston University, Department of Biomedical Engineering, Boston, MA 02215, United States*

[3] *Beth Israel Deaconess Medical Center, Department of Medicine, Boston, MA 02115, United States*

[4] *ICube Laboratory, University of Strasbourg, Illkirch 67412, France*

**Co-first authorship shared*

3.2.1 Introduction

Fluorescence image guided surgery has been shown to provide improved benefit to patients.[153] Current state of the art clinical fluorescence imaging systems do not account for the distorting effects of tissue optical properties. As a result, clinical assessments of the fluorophore levels are highly prone to subjectivity and as such, are qualitative in nature.[21,57,87,140,164,165,167,169,191,192] Qualitative assessments can lead to intraoperative assessments of 'no fluorescence present' in areas of low, raw fluorescence emissions and/or higher attenuation, and as such surgeons are prone to leaving significant levels of non-visually fluorescent tumor tissue unresected.[165,167] This can be particularly crucial near the end of resection when the surgeon is surveying the surgical cavity for left over, infiltrative tumor.

The varying effects of tissue optical properties significant impact light tissue interactions during fluorescence imaging of tissue, which lead to qualitative, relative assessments of the emitted fluorescence. Two broad categories of methodologies for addressing this non-linear phenomenon are: model based corrections or empiric ratiometric techniques.[21] The former provides direct estimates of tissue optical properties and applies them in a model of the fluorescence, and the later, uses a ratio of the raw fluorescence over the tissue reflectance to correct the raw fluorescence. Model based techniques to date have been mostly successful with single point probes. Recent studies have demonstrated some advances in imaging based methods whereas the ratiometric techniques have had more success translating into imaging techniques.[21,35,57,86,140,166,168,191,192]

An ideal optical property corrected fluorescence technique would provide real-time, i.e. video rate, images of the full surgical field of view; would collect the necessary information to estimate tissue optical property maps of the surgical cavity to implement a rigorous model based fluorescence correction method; and would estimate optical property corrected fluorescence images co-registered in both space and time. Here we present a technique using single snapshot optical properties (SSOP) imaging[177] to image the tissue optical properties in real time. Our imaging system was coupled with simultaneous acquisition of the tissue fluorescence to derive optical property corrected maps of fluorescence. We call this technique, quantitative fluorescence-single snapshot optical properties (qF-SSOP) imaging represents a significant advancement in fluorescence image guidance as we provide a novel real-time optical property corrected

fluorescence imaging technique that has the potential to integrate with the neurosurgical workflow and significantly improve molecular fluorescence image guidance.

3.2.2 Materials and Methods

The raw fluorescence undergoes attenuation due to the heterogeneous effects of tissue optical properties at both the excitation and emission wavelengths. A significant effort has been dedicated at developing empiric ratiometric, model-based, spectroscopic and/or imaging based techniques that account for these effects to produce quantitative (i.e., intrinsic, optical property corrected) fluorescence estimates.[21,57,86,140,164,168,169,191,192] The basic concept for estimation of the quantitative fluorescence assumes that the quantitative fluorescence, $\boldsymbol{f_{xm}}$, is a function of the raw fluorescence, $\boldsymbol{F_{xm}}$, and an unknown correction factor, **X**,

$$f_{xm} = \frac{F_{xm}}{X} \tag{17}$$

The correction factor is a function of the tissue optical properties and system specifics (e.g., excitation power, detector efficiency), such that application of this factor on the raw fluorescence can account for the pixel-by-pixel fluorescence attenuation. A common correction technique uses an empiric correction of the fluorescence as ratio of the raw fluorescence over the reflectance at the excitation wavelength, $\boldsymbol{F_{xm}/R_{x.}}$[169] More rigorous techniques use model-based correction methods that depend on *a prior* estimates of the diffuse reflectance and tissue optical properties to derive a correction factor, $\boldsymbol{X}$, and

ultimately, the quantitative fluorescence, $\boldsymbol{f_{xm}}$.[21] Here we used a previously validated algorithm[86] noted in Equation 18 that has been shown to correct for the distorting effects of tissue optical properties to produce quantitative estimates of tissue fluorescence,

$$f_{xm} = \frac{\eta_{a,x}}{\left(1 - R_{,x}\right)} * \frac{F_{xm}}{R_m} \tag{18}$$

Equation 18 is a function of the raw fluorescence, the absorption coefficient at the excitation wavelength, and the diffuse reflectance at the excitation and emission wavelengths. Estimation of the diffuse reflectance and derived tissue optical properties provides the necessary information to derive the correction factor, $\boldsymbol{X}$.

We used an imaging system enabled for simultaneous patterned illumination and fluorescence imaging. Patterned illumination is required for SSOP imaging at one predetermined frequency. Previous work by our group, Vervandier and Gioux,[177] validated the use of single patterned illumination with subsequent line processing in the frequency domain for extraction of optical properties. This was a technical development arising from the standard spatial frequency domain imaging (SFDI) technique which uses patterned illumination at multiple frequencies and multiple phases (i.e., 6 total images) for estimation of the diffuse reflectance and tissue optical properties[35]. SSOP imaging uses one single frequency without need of multiple phases. As such, it requires only one (1) image to extract the tissue optical properties, in comparison to the standard 6 images required for SFDI. Our system performs SSOP imaging with patterned illumination at the

excitation (λ_x = 760 nm) and emission (λ_m = 808 nm) wavelengths, and simultaneously excites tissue to collect spatially and temporally co-registered fluorescence emissions (λ > 815) (Fig. 3.2.1a,b). We can subsequently use SSOP techniques to estimate the diffuse reflectance (R_x, R_m), and derive the tissue optical properties – absorption ($\mu_{a,x}, \mu_{a,m}$) and reduced scattering ($\mu'_{s,x}, \mu'_{s,m}$) - at both wavelengths (Fig. 3.2.1b).

We fabricated tissue simulating phantoms using silicone oil and one tenth part methanol as the medium. India ink (Blick Art Materials, Boston MA) was used as the main absorber, and titanium oxide (Atlantic Equipment Engineers, Bergenfield NJ) as the main scatterer. ZW800-1, developed in the Center for Molecular Imaging at Harvard Medical School, was used as the main fluorophore and functions as a near infrared fluorophore that typifies other similar clinical NIR compounds such as indocyanine green (ICG). Fifteen (15) phantoms at varying absorption and scattering properties were fabricated in the range of $\mu_{a,x}$ = 0.05 – 0.20 mm^{-1} and $\mu'_{s,x}$ = 1.0 – 2.1 mm^{-1} (Table 3.2.1). Each phantom was made with a fluorophore concentration of 5 μmol/L ZW800-1.

Table 3.2.1 Phantom Optical Properties

Phantom #	$\mu_{a,x}$	$\mu_{s,x}'$
1	0.1	1.4
2	0.06	1.8
3	0.05	2.1
4	0.12	1.3
5	0.09	1.7
6	0.07	2
7	0.15	1.2
8	0.1	1.7
9	0.07	2
10	0.17	1.1
11	0.14	1.5
12	0.1	1.8
13	0.2	1
14	0.16	1.3
15	0.17	1.7

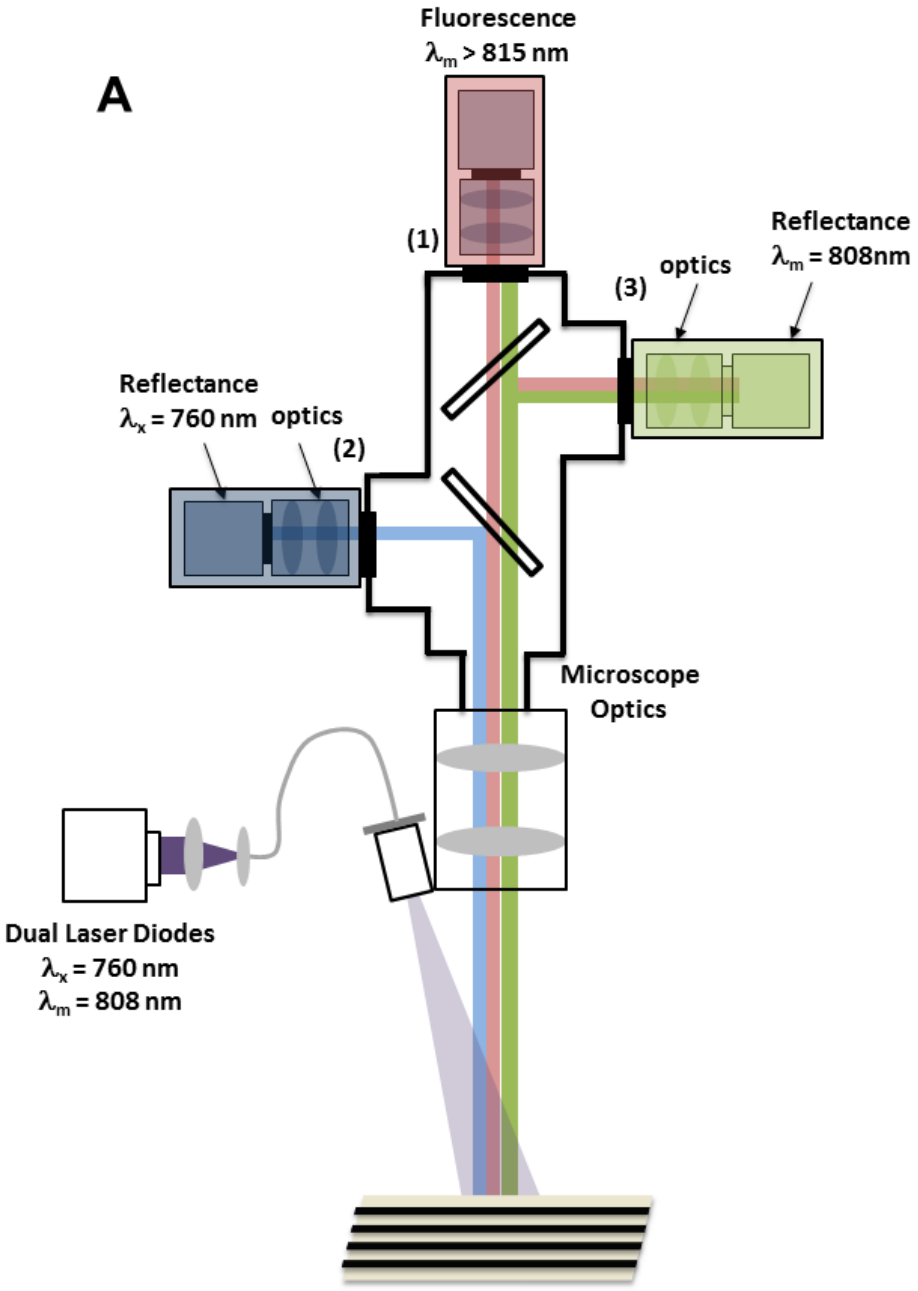

Figure 3.2.1 A): QF-SSOP Imaging Schematic. A surgical guidance SFDI system adapted for dual SSOP reflectance and fluorescence imaging was used[63]. Three temporally and spatially simultaneous images are acquired in real time: one fluorescence (λ>815 nm) and two reflectance images at the excitation (λ_x=760 nm) and emission wavelengths (λ_m=808 nm) under SSOP mode.

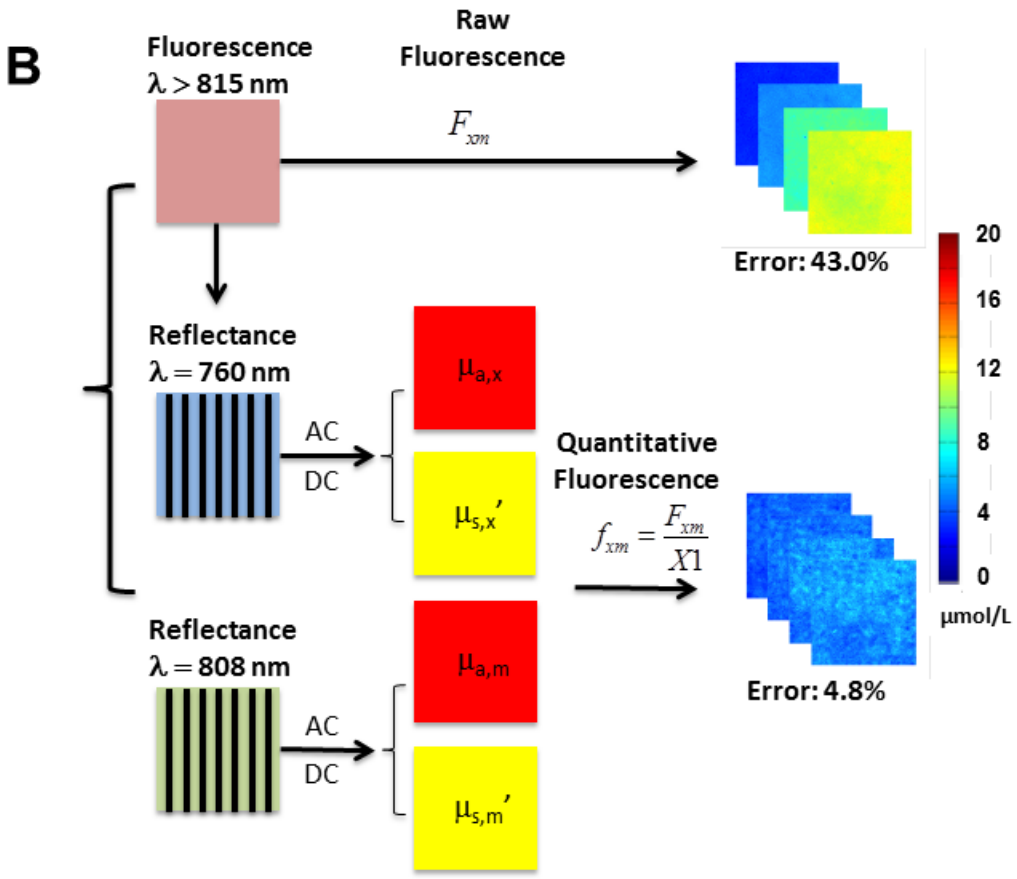

Figure 3.2.1 B): QF-SSOP Imaging Data Flow. The reflectance images at λ_x and λ_m at one spatial frequency are processed under SSOP conditions to derive the diffuse reflectance and corresponding μ_a and μ_s' maps. Fluorescence is evaluated using either the raw fluorescence maps only ($F_{x,m}$) or an attenuation correction is applied unto the raw fluorescence $F_{x,m}$ to correct for the distorting effects of tissue optical properties to derive quantitative fluorescence maps ($f_{x,m} = F_{x,m}/X$)

3.2.3 Results

Figure 3.2.2 presents phantom results across all combinations of scattering and absorption for both the raw (Fig. 3.2.2(a)), the F/R (Fig. 3.2.2(b)), and quantitative fluorescence (Fig. 3.2.2(c)). Optical property measurements were made with a spatial frequency pattern of 0.2 mm^{-1}. In Figure 3.2.2(a) the raw fluorescence signal intensity of 15 phantoms without correction for varying optical properties demonstrates a

qualitatively clear difference in the fluorescence signal in phantoms with highest absorption and lowest scattering (lower left corner) compared to phantoms with lowest absorption and highest scattering (upper right corner). The difference between the highest and lowest fluorescence signal phantoms varied by ~10x (st.dev 2.82 a.u., range: 1.7 - 11.7 a.u.) using the raw fluorescence estimates for ZW800-1 levels. Figure 3.2.2(b) shows the same 15 phantoms after using a standard literature empiric correction of F/R for variation in tissue optical properties.

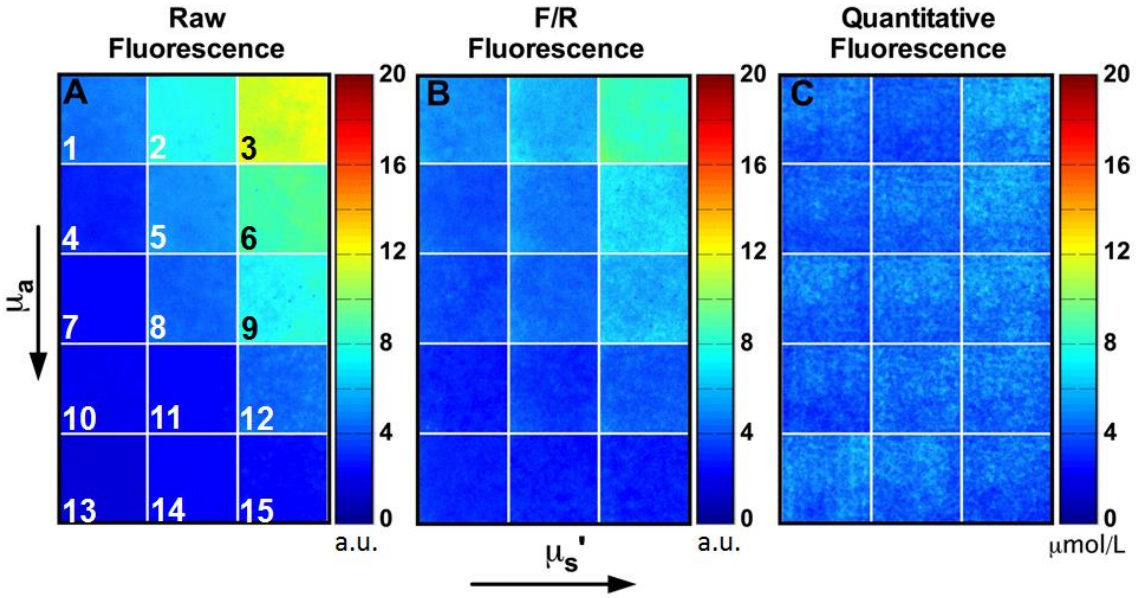

Figure 3.2.2: Raw and corrected fluorescence using Equation 2. Tissue simulation phantoms with equal fluorophore concentrations (5 μmol/L) demonstrate a clear difference in the A) raw fluorescence with attenuating effects with increasing absorption (top to bottom) and increasing scattering (left to right); B) demonstrates the F/R empiric fluorescence following an empiric correction using the raw reflectance in the same phantoms with a moderate improvement in the estimated fluorescence across all tissue phantoms; whereas C) demonstrates the qF-SSOP derived quantitative fluorescence following a model based correction for tissue optical properties in the same phantoms with a notable similarity in the estimated fluorescence across all tissue phantoms. Note: all methods were scaled to the same values of fluorescence, though on aF-SSOP it quantitative and reports units of concentration.

The F/R correction results demonstrate a moderately smaller variation in estimated levels (st.dev 1.39 a.u., range: 3.63 – 8.39 a.u.). Figure 3.2.2(c) shows the same 15 phantoms after using simultaneous SSOP and fluorescence detection for correction of tissue optical properties. In comparison to both the raw and F/R fluorescence estimates, the qF-SSOP correction results demonstrate a much smaller variation in estimated levels (st.dev 0.32 μmol/L, range: 4.55 – 5.66 μmol/L). These results qualitatively demonstrate an improvement in the recovered, estimated fluorescence using a fluorescence correction technique in imaging mode.

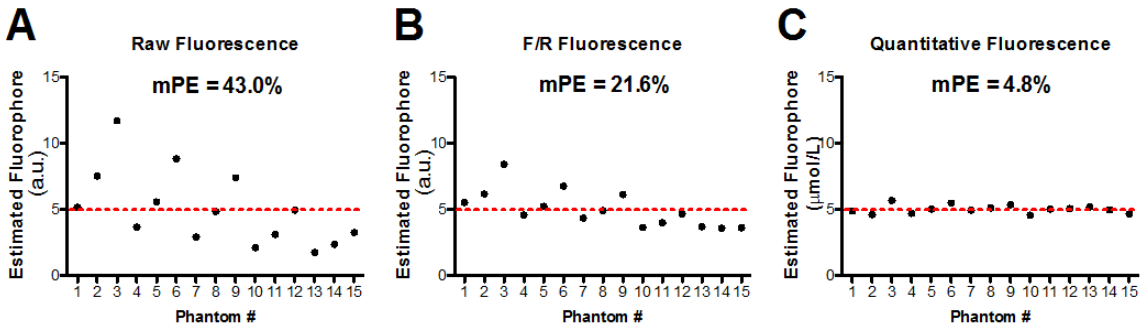

Figure 3.2.3: Region of interest analysis of raw and qF-SSOP corrected fluorescence. Estimated fluorophore concentrations using A) raw fluorescence demonstrate a significant deviation from the true phantom concentration (dotted red line) of 5μmol/L compared to the B) F/R fluorescence, and the C) quantified fluorescence as demonstrated by the mean percentage error estimates of 43.0%, 21.6% and 4.8%, respectively.

We analyzed each phantom to quantify the error in fluorescence estimates. Figure 3.2.3(a) shows the raw fluorescence, Figure 3.2.3(b), the F/R fluorescence, and Figure 3.2.3(c) the qF-SSOP estimated quantitative fluorescence. A dotted red line denotes the known fluorescence level of 5 μmol/L. The mean percentage error (mPE) for the raw fluorescence estimates was 43.0% with a coefficient of variation of 80.1% (st.dev:

34.5%, range: 1.2% - 134%). A moderated improvement of approximately 50% in the estimates is noted with the standard correction technique of F/R fluorescence estimates of 21.6% with a coefficient of variation of 75.7% (st.dev: 16.3%, range: 2.1% - 67.9%). Meanwhile, for the corrected, quantitative fluorescence, a much larger improvement was produce with a mPE of 4.8% and a coefficient of variation of 6.4% (st.dev: 4.0%, range: 0.1% - 13.2%).

Figure 3.2.4 presents a single frame from the real-time acquisition of two phantoms with distinct optical properties but the same level of fluorophore (8 μM), acquired with 0.24 mm^{-1} spatial frequency and flat-fielded. The video shows a real-time image of (a) the raw fluorescence, (b) F/R fluorescence, and (c) the corrected, quantitative fluorescence. As expected, Figure 3.2.4(a) and (b) show a marked difference in the detected fluorescence, whereas Figure 3.2.4(c) shows no clear difference in the estimated fluorophore levels. Note that both (a) and (b) have arbitrary units with max fluorescence set to 85%, and (c) the correct fluorescence is calibrated for fluorescence, allowing units of molecular concentration.[191] This video was acquired with a 500ms exposure time, giving a framerate of 2 frames per second.

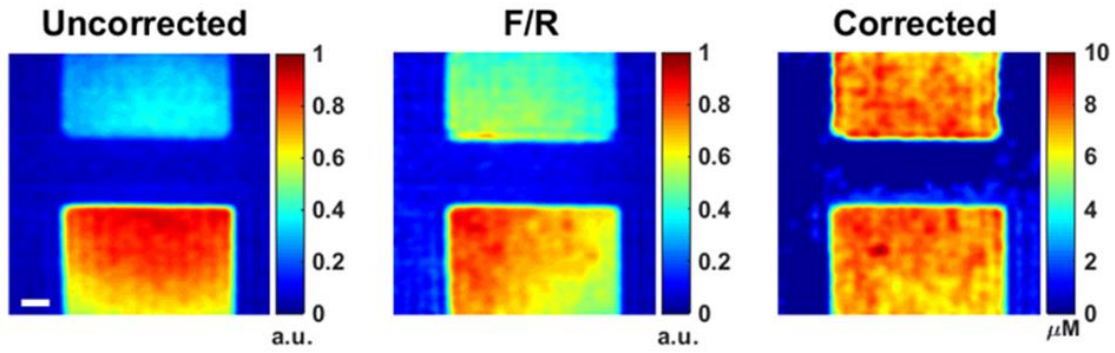

Figure 3.2.4: Video-frame of two tissue simulating phantoms. Two tissue simulating phantoms of varying tissue optical properties are imaged in real time with A) showing the raw fluorescence, B) the F/R fluorescence, and C) the qF-SSOP quantitative fluorescence of the same phantoms following correction for tissue optical properties. Note, only the quantitative fluorescence imaging presents a quantitative scale in fluorophore concentration.

3.2.4 Discussion

These promising results demonstrate a real-time imaging technique that acquires maps co-registered in space and time of tissue optical properties and raw fluorescence emissions followed by a rigorous model-based correction to estimate the quantitative fluorescence. The qF-SSOP technique provides a means to collect video rate images that are corrected for the distorting effects of tissue optical properties on the fluorescence emissions meanwhile concurrently collecting the absorption and scattering images for the same tissue. Our study uses one particular correction method noted in Eq. 18, but can be applied to a number of other rigorous model-based correction methods that depend on a priori knowledge of the tissue optical properties. We chose this model for its simplicity and successful implementation in previous studies for brain tumor surgery.[166].

This study used flat phantoms without the use of profilometry, or curvature correction methods. We have previously described a technique for curvature correction, and our

group is actively optimizing such methods to implement in our next iteration of this technology for ex vivo and in vivo studies on rodents glioma models and clinical surgeries having demonstrated the ability to perform quantitative fluorescence imaging.[62] Our technique uses SSOP, which has previously been validated to provide estimates equivalent in accuracy to the standard SFDI method.[177] Further, the current qF-SSOP system employs single band pass and long pass filters for collection of the reflectance and emitted fluorescence, and does not collect spectrally resolved data for fluorophore multiplexing. We are currently integrating previously developed spectrally resolved methods for fluorophore multiplexing with our SSOP technique.[167] Here we used the NIR fluorophore, ZW800-1, which is similar to other NIR compounds such as ICG. Our system is built for NIR imaging, but in principle, any fluorophore could be used, including Protoporphyrin IX (PpIX), which is currently used for brain tumor surgery. Future work is aimed at modifying our system to image PpIX in vitro and in vivo to implement in the neurosurgical operating room for quantitative PpIX imaging.

3.2.5 Conclusion

In conclusion, with the use of SSOP for real time estimates of tissue optical properties, we demonstrate a novel imaging system and technique for rigorous and model-based quantitative fluorescence imaging. Unlike previous studies, our qF-SSOP technique provides co-registered real-time tissue optical property maps and quantitative fluorescence images based on a rigorous model based method. This novel technique can

be easily integrated into the surgical workflow to further guide tumor resection, and enable more accurate molecular guidance.

3.2.6 Acknowledgments

This research was supported by grants from K01-DK-093603, France Life Imaging, University of Strasbourg and ICube Laboratory (S.G.), NIH/NIDDK Award Number F31-DK-105839 (J.A.), and DGE-1247312, a NSF-GRFP Fellowship (J.A.). We thank Dr. Hak Soo Choi for providing the ZW800-1 fluorophore and useful discussions. Pablo A. Valdes is supported through the Harvard Medical School Department of Neurosurgery at Brigham and Women's/Boston Children's Hospitals.

CHAPTER 4: REAL-TIME IMAGING OF TISSUE PROPERTIES

Surgical guidance poses a unique scenario and restricts the parameters for potential technological solutions. Space in the operating room is highly limited and time is costly in both patient care and patient management. Ideally, the technique would be noncontact and measure broadly so as to not disrupt the surgeon's field of view and it would provide quantitative feedback in real-time. Chapter 3 introduces two novel techniques with potential for future surgical guidance in the clinic, though they both rely on exogenous contrast. While these techniques are sure to benefit from future fluorophore development and FDA approval, we also wanted to focus on techniques that did not rely on exogenous agents and instead could utilize the wealth of endogenous contrast in tissue, namely hemodynamic contrast.

The importance of oxygen in all aspects of wound healing has been well studied for many years,[73,74] and so tissue oxygenation measurement has shown a prominent role in assessing tissue viability.[69] The original point-probe optical techniques have proven useful as pioneering oxygenation measurements with light. However, due to their single point sampling this technique requires contact with the tissue and relies on global effects, and visualization of the complete surgical field would be advantageous. Furthermore, no adaptation of this technique, or a full-field technique, has been made suitable for minimally invasive surgery.

This chapter introduces novel acquisition schemes for breaking current limits of oxygenation measurements. First, we improve upon real-time widefield acquisition by incorporating a profile-correction method – crucial for any practical clinical use of non-contact imaging. Next, parts 4.2 and 4.3 introduce and progress through the development of endoscopic oxygenation imaging, something heretofore never achieved.

4.1. Real-time, Profile-corrected Single Snapshot Imaging of Optical Properties

The work in part 4.1 is published in Biomedical Optics Express[170] with the following contributing authors:

Martijn van de Giessen,[1,2] Joseph Angelo,[1, 3] and Sylvain Gioux[1]

[1] *Beth Israel Deaconess Medical Center, Department of Medicine, 330 Brookline Avenue, Boston, MA 02215, United States*

[2] *Division of Image Processing, Leiden University Medical Center, Albinusdreef 2, 2333 ZA, Leiden, The Netherlands*

[3] *Boston University, Department of Biomedical Engineering, Boston, MA 02215, United States*

4.1.1 Introduction

Over the last few years, sub-surface diffuse optical imaging has been making constant progress towards reaching the bedside, in particular in the fields of functional point measurement[91,136] and wide-field surgical guidance.[61,169] However, providing real-time quantitative sub-surface images remains a significant challenge that has been strongly limiting diffuse optical imaging in being more widely tested and applied. Recent developments in Spatial Frequency Domain Imaging (SFDI) have shed hopes in solving this fundamental issue.[35] This method relies on the analysis of the spatial frequency response of turbid media to structured illumination (i.e. stripes of light), allowing the characterization of an entire field-of-view at once (i.e. in a multipixel approach). SFDI has shown significant promise in performing wide-field surgical guidance and specimen examination, both in animals and in humans, *ex vivo* and *in vivo.*[63,93,120,130,138 ,189]

Despite its capabilities of analyzing full fields-of-view at once, traditional SFDI acquisitions have been limited to phase shifting approaches to extract the tissue response to structured illumination, impairing its capabilities to perform in real time. Indeed, a minimum of 6 images is necessary to extract optical properties (absorption and reduced scattering), 3 phases at 2 spatial frequencies, with this number increasing to 9 images when performing simultaneous profile acquisition to correct for the effects of the sample distance and profile.

Efforts are currently being made to find alternative demodulation techniques to reduce the acquisition time in the spatial frequency domain. Nadeau et al. introduced a two-dimensional Hilbert transform method requiring only 2 images instead of 6 to extract the necessary information for deducting optical properties.[115] While much faster than the 3-phases traditional approach, this method still uses two sequential images, and necessitates expensive instrumentation (projector and camera) to perform at a real-time level. Our group recently introduced Single Snapshot of Optical Properties (SSOP), a method working entirely in the frequency domain that necessitates the acquisition of a single image to extract the optical properties.[177] While very rapid and inexpensive (a single projection slide containing a pattern is necessary), this method suffers from a degraded image quality due to the single-phase acquisition and spatial frequency filtering.

While these recent advances improve the capabilities of SFDI for forming quantitative images rapidly over a large field-of-view, none is taking into account the 3D-surface

profile of the sample, a major source of error using non-contact imaging techniques. As part of previous work, we introduced a method capable to acquire both the profile and optical properties sequentially in the spatial frequency domain, and developed a method using the 3D-profile information to correct for the effects of sample-to-imaging device distance and of sample's surface angle.[62] Not correcting for these effects can lead to very strong variations in optical properties, 10% errors on average per cm, and 86% for a 40 degree surface angle, preventing the use of SFDI during many clinical scenarios.

In this work, we present a novel acquisition and processing method that recovers both optical properties and surface profile from a single snapshot acquisition. This method is based on the previously developed Single Snapshot of Optical Properties (SSOP) method, but with the difference that both the phase and the amplitude modulation of a 2-dimensional sinusoidal intensity wave are recovered from a single projection. The method was validated on tissue mimicking phantoms and *in vivo*. Tissue mimicking phantoms with known absorption (μ_a) and reduced scattering (μ_s') coefficients were imaged using the single acquisition method and compared to the original 3-phase SFDI acquisition method. Finally, a demonstration of real-time acquisition using 3D-SSOP was performed on both a hemispherical tissue mimicking phantoms and on a human hand. Together, this study lays the foundation for the development of real-time quantitative sub-surface imaging for the clinic.

4.1.2 Materials and Methods

4.1.2.1 Spatial Frequency Domain Imaging

Spatial frequency domain imaging (SFDI) has been described extensively in the literature and will be only briefly summarized here. Analogous to the temporal point-spread function (t-PSF) as response to a pulse illumination in time-domain, a point source that illuminates tissue induces a diffuse reflectance with a spatial point spread function (s-PSF). The shape of the spatial decay of the s-PSF is characteristic for the sub-surface optical properties of the tissue.[52] Just as temporal frequency-domain measurements acquire as a function of temporal frequency the t-MTF (Modulation Transfer Function, the t-PSF Fourier equivalent), SFDI acquires the s-MTF as a function of spatial frequency by projecting a wide 1D intensity sinusoidal wave on the tissue.[44]

The medium s-MTF is represented by the diffuse reflectance R_d measured at a location x and spatial frequency f_x. The diffuse reflectance R_d of the medium (here considered homogeneous and with a semi-infinite geometry) can be modeled in various ways using the diffusion approximation to the radiative transport equation or Monte-Carlo.[36] On the other end, instrumentally, the diffuse reflectance is measured by extracting the amplitude modulation $M(x,f_x)$ from a projected intensity sinusoidal wave. Once the diffuse reflectance has been measured, solving the inverse problem allows the recovery of the optical properties of the medium.

Relevant to this work, the acquisition of the amplitude modulation of the projected sinusoidal wave traditionally relies on a 3-phases demodulation technique.[117] The intensity I of a sinusoidal wave as a function of x, at a spatial frequency f_x and phase Φ_i projected on the medium is acquired on the camera as:

$$I_i(x, f_x) = M(x, f_x)\cos(f_x \cdot x + \Phi_i) + I_{DC}(x) \tag{19}$$

where $M(x,f_x)$ is the amplitude modulation, and I_{DC} the DC component. $M(x,f_x)$ is obtained by projecting three sequential sinusoidal waves with phases $\Phi_{i\,=\,1\text{-}3}$ = [0°, 120°, 240°]:

$$M(x, f_x) = \frac{1}{3}\sqrt{2\left\{\begin{matrix}[I_1(x, f_x) - I_2(x, f_x)]^2 + [I_2(x, f_x) - I_3(x, f_x)]^2 \\ +[I_3(x, f_x) - I_1(x, f_x)]^2\end{matrix}\right\}} \tag{20}$$

The amplitude modulation $M(x,f_x)$ can be related to the measured diffuse reflectance $R_d(x,f_x)$ (the 1-D version as shown is chapter 2):

$$M(x, f_x) = I_0 \cdot \mathrm{MTF}_{sys}(x, f_x) \cdot R_d(x, f_x) \tag{21}$$

with I_0 the source intensity and $\mathrm{MTF}_{sys}(x,f_x)$ the amplitude modulation of the optical system (e.g. lenses). Finally, the medium diffuse reflectance is obtained by using a calibration reference with known optical properties (1-D version of Eq. 4 in chapter 2):

$$R_d(x, f_x) = \frac{M(x, f_x)}{M_{\mathrm{ref}}(x, f_x)} \cdot R_{d,\mathrm{ref,pred}}(f_x) \tag{22}$$

where $M_{ref}(x,f_x)$ is measured on the calibration reference, and $R_{d,ref,pred}(x,f_x)$, modeled based on the known optical properties of the medium

In the traditional "fast" acquisition implementation, two spatial frequencies (e.g. 0 and 0.2 mm^{-1}) are obtained by imaging a sinusoidal wave with three offsets in phase (e.g. 0°, 120° and 240°) per frequency.[35] The amplitude for both frequencies is obtained by demodulation of the three phases.[117] Following calibration using a tissue-mimicking phantom with well-known optical properties, the tissue sample optical properties can then be estimated rapidly from a precomputed lookup table generated using a Monte Carlo model.[35,49]

4.1.2.2 Profile-corrected SFDI

The original SFDI description assumes imaging of a flat surface at a well-defined height.[35] In clinical practice this assumption is challenging to satisfy, leading to calibration errors due to 1) variations in distance between the imaging system and the sample, and 2) the sample's local surface angle. Using a multi-height calibration method along with a Lambertian model for the reemitted light intensity from diffusive surfaces, the local intensity of the collected light can be corrected for these two effects.

As explained in detail here[62] and illustrated in Figure 4.1.1, optical properties are obtained by projecting sinusoidal patterns that are parallel to the plane spanned by the projector and optical collection axes. Such a projection ensures that the phase of the projected sinusoidal wave is insensitive to height variations. Following optical properties

acquisition, the surface profile is obtained through phase profilometry. Contrary to optical properties, the projected profilometry fringes need to be maximally sensitive to height variation and are projected perpendicular to the plane formed by the projection and collection axes. The height dependent phase is then obtained by demodulating a three phase acquisition, called phase-shifting profilometry,[75,152] similar to the 3-phase SFDI acquisition. Finally, the sample distance and angle is used to correct the intensity of the SFDI acquisition at each pixel. This approach has been validated and translated to the clinic.[63]

Alternatively, using Fourier transform based profilometry, a single image can be used to determine the height dependent phase of a projected profilometry fringe.[159] Because it relies on a single projection pattern, and therefore allows real-time measurements, this approach is taken in this work. Here the intensity variations due to the projected fringes are assumed to dominate intensity variations from tissue reflectivity in the spectral band around the projected carrier spatial frequency f_y. Taking the 1D Fourier transform in the image direction along the projected profilometry fringes enables separation of the profilometry information from slower varying intensity changes. Through the selection of only the positive sideband around f_y and applying the inverse 1D Fourier transform a complex signal is obtained that contains the local phases φ_y. The phase difference $\Delta\varphi$ between φ_y and the local phases φ_0 in a reference plane is directly related to the distance between camera and tissue.

4.1.2.3 Single Snapshot of Optical Properties

We previously developed an acquisition and demodulation method, called Single Snapshot of Optical Properties (SSOP), capable of extracting optical properties in the spatial frequency domain from a single acquired image. SSOP works by projecting a single sinusoidal pattern onto the specimen and relies on processing entirely in the frequency domain to extract the DC and AC components (i.e., 2 spatial frequencies) that are used to calculate the specimen's optical properties.[177]

4.1.2.3 Simultaneous Imaging of Optical Properties and 3-D Profile

In this work, we propose to extend this work to acquire simultaneously both optical properties and surface profile in real-time, and to directly obtain profile-corrected optical properties maps from a single image. For this purpose, a pattern containing two superimposed sinusoidal waves, orthogonal to each other, are projected onto the specimen. Specifically, one pattern will be used for optical properties processing (similarly to standard SSOP) and the other for extracting the specimen surface profile.[62] As illustrated in Figure 4.1.1, by projecting a dual sinusoidal wave pattern, one can gather information regarding both profile-sensitive pattern orientation (horizontal in this case) and optical properties, profile-insensitive pattern orientation (vertical in this case). Note that the profile-sensitive patterns are also sensitive to optical properties. However, the sinusoidal wave phase variations renders the amplitude modulation extraction challenging. In essence, the profile sensitive patterns are used to extract the phase of each

pixel in the image that can in turn be used to deduce each pixel's height.[200] Following this step, the profile insensitive patterns are used to extract the AC and DC components of the image, similarly to standard SSOP. Finally, the height information is used correct for both height and angle effects, and optical properties extracted.[62]

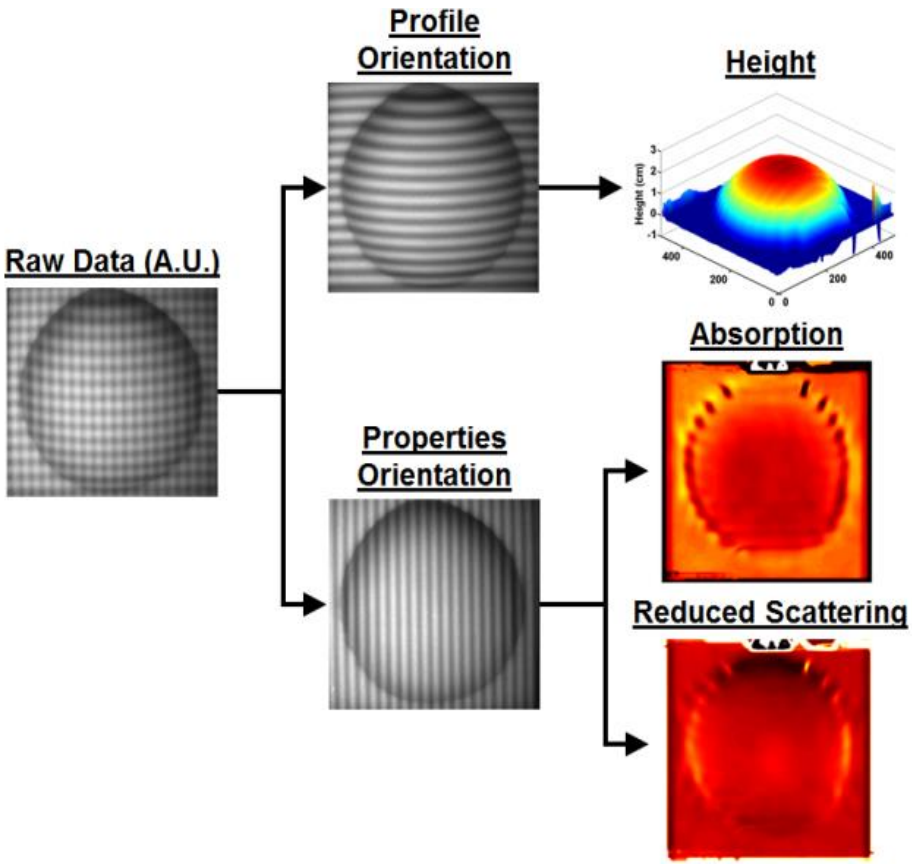

Figure 4.1.1: 3-D Single Snapshot of Optical Properties. A dual sinusoidal wave is projected, one wave being sensitive to the specimen's optical properties and the other to the specimen's profile. AC, DC components as well as phase are extracted (not shown here) leading to profile, absorption and reduced scattering.

More precisely, the AC and DC components as well as the phase for profilometry are estimated in frequency space. In this space, the optical properties sinewave (properties

orientation in Figure 4.1.1) exhibits a narrow band in one direction and the profilometry sinewave (profile orientation in Figure 4.1.1) a narrow band in a second direction, perpendicular to the first one. Apart from these pronounced bands, the higher frequency content describes spatially varying intensity variations of the projected waves, e.g. due to the height sensitive profilometry wave deformations. The orthogonality in the Fourier domain and clear detectability of frequency bands enables separation of the AC and DC components, as well as the phase for Fourier transform profilometry.

In 3D-SSOP each image is analyzed according to the schematics in Figure 4.1.2. After acquisition each frame is expanded using mirrored images to minimize artifacts due to discontinuities at the image edges (Figure 4.1.2.B). The expanded image is transformed to the frequency domain with a two-dimensional Fourier transform (Figure 4.1.2.C). The DC and AC components are obtained by filtering in the frequency domain with the filters shown in Figure 4.1.2.D and 4.1.2.E, respectively. The phase is obtained by filtering in the frequency domain with the filters shown in Figure 4.1.2.F. These filters are designed to select the appropriate frequency bands, while minimizing the formation of artifacts near discontinuities in the images. The latter is achieved by preserving the high frequency information in each of the filters. The bands that cover the projected waves are centered on the projected frequency. In this work, the band centers are estimated by peak detection in a 2D Fourier transform of a flat calibration image. Depending on the acquisition geometry and the expected variation in distance to sample, one could re-estimate the bands from each frame. The widths of the bands are user-determined and depend on the

accuracy of the projected sine waves and on the expected steepness of ramps in the scene for the profilometry wave.

After filtering, an inverse two-dimensional Fourier transform is applied to each of the filtered frequency domain images. The DC component is a direct result of the inverse two-dimensional Fourier transform (Figure 4.1.2.G). The inverse Fourier transformed images for the AC and phase components are obtained by applying an additional Hilbert transform (Figures 4.1.2.H and 4.1.2.I, respectively). The final images are obtained by selecting the central portion of the expanded frames.

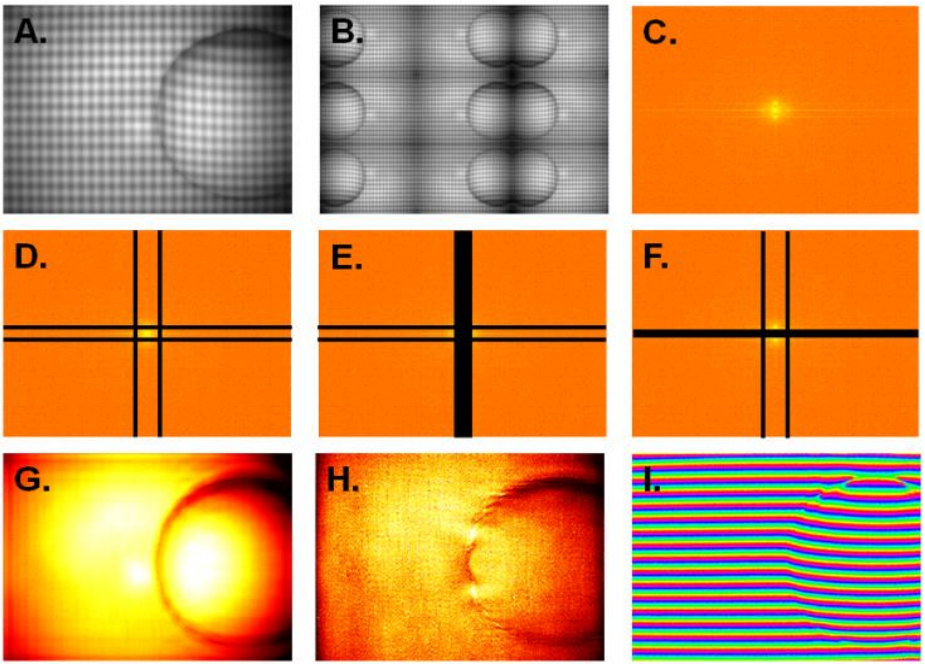

Figure 4.1.2: Data processing for 3-D Single Snapshot of Optical Properties. The acquired image (A) is expanded by mirroring (B) and a 2D Fourier transform performed (C). Filters (D, E and F) are then used to isolate the DC component (G), the AC component (H) and the phase (I), respectively.

4.1.2.5 Calibration

Spatial Frequency Domain Imaging necessitates a calibration measurement.[35] Our imaging setup is calibrated using a flat, homogeneous, tissue-mimicking phantom of 96×96×20 mm with known optical properties. The phantom consists of polydimethylsiloxane with India ink as absorber and TiO2 as scattering agent.[10] The spectral absorption and reduced scattering coefficients were verified with two-distance, multifrequency FDPM measurements.[15] In addition, because we perform 3D profile correction, the height dependency frequency response is calibrated by acquiring our calibration phantom at 6 heights with 1 cm steps.

4.1.2.6 Experiments

Three experiments were performed to compare the accuracy and precision of the proposed 3D-SSOP method with standard three-phase modulated and profilometry-corrected SFDI (3D-SFDI). All images have been acquired a 670 nm and at a spatial frequency of 0.2 mm^{-1} for optical properties calculation and of 0.15 mm^{-1} for phase extraction. Cutoff frequencies were set at 0.16 mm^{-1} (low) and 0.24 mm^{-1} (high) for filtering the AC component for optical properties calculation, and 0.11 mm^{-1} (low) and 0.20 mm^{-1} (high) for filtering the signal for the extracting the phase for profilometry.

Flat homogeneous phantom: In this experiment, height and optical properties were recovered from a tissue-mimicking phantom with known optical properties, imaged at six heights with steps of 1 cm. Using titanium oxide (TiO2) as a scattering agent and India

ink as absorbing agent, optical properties were set at 0.036 mm^{-1} for absorption (μ_a) and 0.97 mm^{-1} for reduced scattering (μ_s'). Height and profile-corrected optical properties maps were extracted using both methods and compared with non-profile-corrected maps using SFDI.

Hemispheric homogeneous phantom: In this experiment a hemispheric tissue-mimicking phantom on top of a flat homogeneous tissue-mimicking phantom having the same optical properties (μ_a = 0.023 mm^{-1} and μ_s' = 0.97 mm^{-1}) were imaged with both methods. Height and profile corrected optical properties maps were extracted and their percentage difference assessed. Finally a movie was captured where the phantom is imaged in real-time using the 3D-SSOP method.

In-vivo measurement: A hand movie was captured where the hand is imaged in real-time for both height and profile-corrected optical properties using the 3D-SSOP method.

4.1.3 Results

4.1.3.1 Flat Homogeneous Phantoms

The results from the flat homogeneous phantoms experiments are shown in Figure 4.1.3. A comparison of profile corrected maps of absorption processed either with profile-corrected SFDI (3D-SFDI) or 3D-SSOP is plotted in 3D in Figures 4.1.3.A and 4.1.3.B. One can notice a good agreement between the two methods, both in 3D profile and in

absorption values. This agreement is quantified and confirmed both in height (plot shown in Figure 4.1.3.C) and in optical properties (absorption shown in Figure 4.1.3.D and reduced scattering shown in Figure 4.1.3.E). Both 3D-SFDI and 3D-SSOP evidenced accurate and precise height estimation, on average within 1.1 mm of the expected height and with an average standard deviation of 0.7 mm. Similarly both methods were able to extract and correct optical properties for all the sample heights, within 1.25% of the expected value, and with 3.1% coefficient of variation for absorption, and 1.1% of the expected value, and with 1.6% coefficient of variation for reduced scattering. Note the extent of the correction necessary to account for the change in height of the sample.

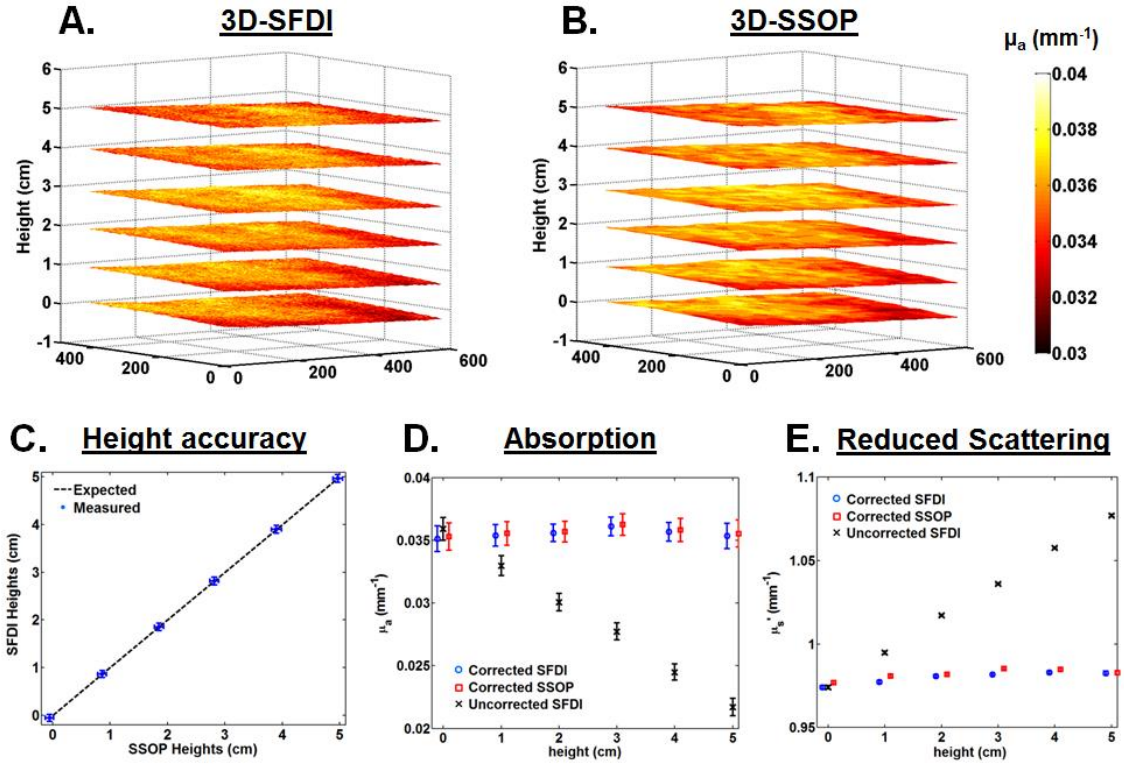

Figure. 4.1.3: Flat homogeneous phantom measurements. 3D-SFDI and 3D-SSOP methods were used to acquire and process a set of homogeneous phantoms at different heights (A and B, respectively). Notice the good agreement in heights (C), and in profile-corrected values for absorption (D) and reduced scattering (E).

4.1.3.2 Hemispheric Homogeneous Phantom

The results from the hemispherical phantoms measurements are shown in Figure 4.1.4. As expected from a single image measurement, the 3D-SSOP maps exhibit artifacts on the edge of the hemispheric phantom, as well as noise due to the variation in angle and height of the surface (themselves due to noise in the 3D profile data). However, on average the novel method performs fairly well, within 1.2 mm of the 3D-SFDI data for height with a 0.3 mm standard variation, 12% for absorption with a 4.2% coefficient of variation and 6.1% for reduced scattering with a 1.7% coefficient of variation (*note: errors are calculated from the absolute difference between the two methods, not the relative difference that would artificially give a lower error*).

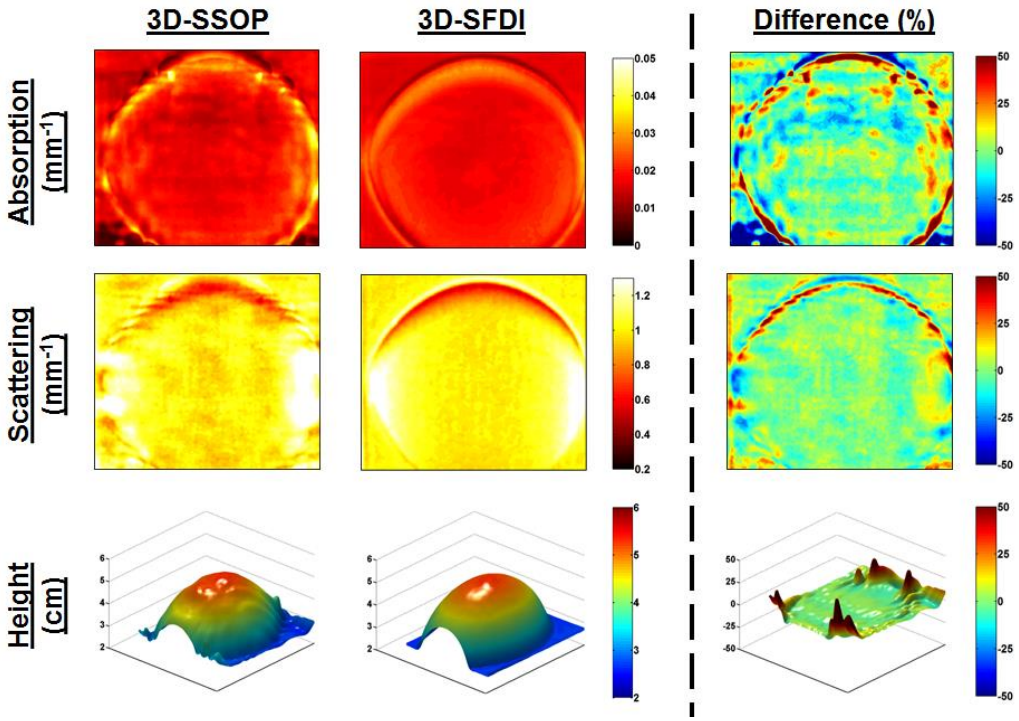

Figure. 4.1.4: Hemispheric phantom measurements. 3D-SFDI and 3D-SSOP methods were used to acquire and process a hemispheric homogeneous phantom. Notice the good agreement in heights, as well as in profile corrected values for absorption and reduced scattering.

To illustrate the advantage of this new method to provide real-time quantitative measurements of optical properties in realistic conditions, i.e. with profile-correction, we included a movie of the hemispheric phantom moving in space. Acquisition time was set at 220 ms, giving a frame rate of 4.5 frames per second. Are shown: the raw data (top, left), the 3D profile data (top, right), and the optical properties (absorption: bottom, left; reduced scattering: bottom, right). Note the quality of the 3D profile data as well as the quantitative values of optical properties over the image while the specimen moves.

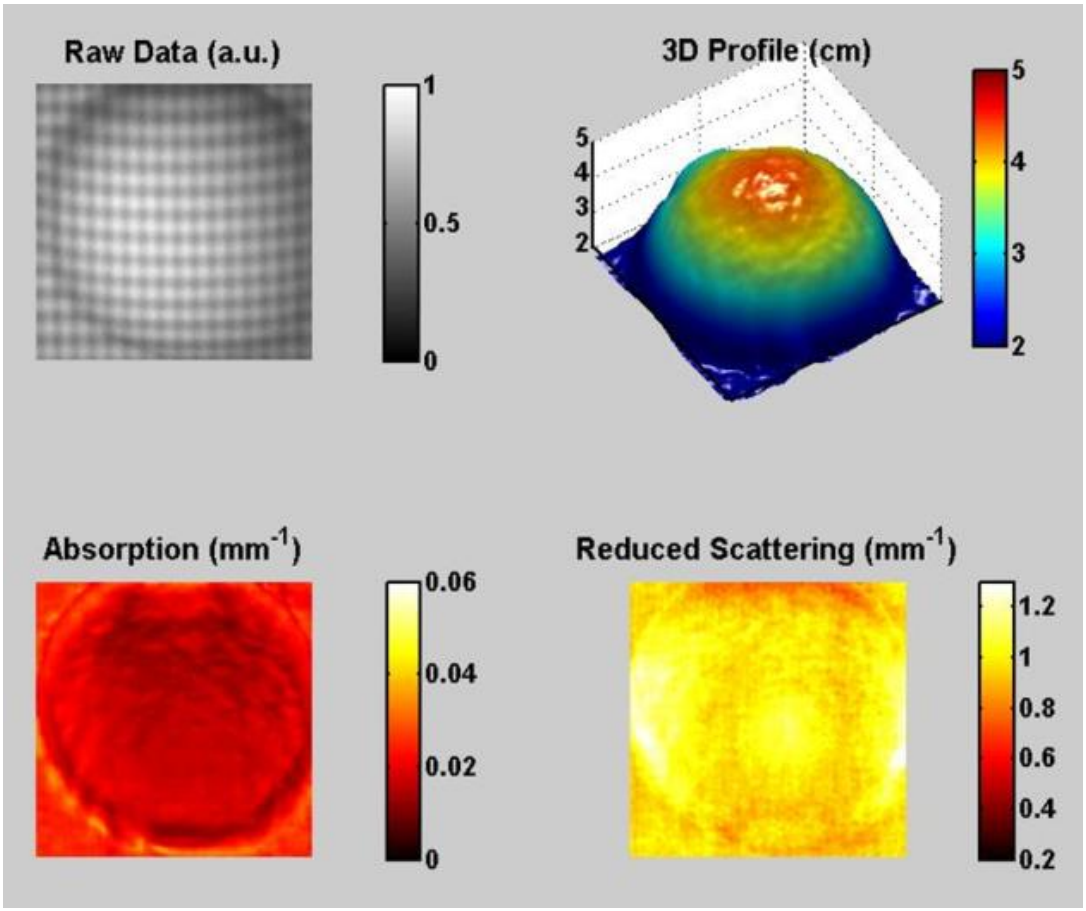

Figure. 4.1.5: Frame from the hemispheric phantom movie. A movie of a homogeneous hemispheric phantom was acquired with the 3D-SSOP method. Raw data (top, left), 3D profile (top, right), profile-corrected absorption (bottom, left) and reduced scattering (bottom, right) are shown.

4.1.3.3 In Vivo Measurement

To validate the novel method capability for providing real-time quantitative optical properties images with profile correction *in vivo*, we acquired a movie of a hand moving while performing a continuous 3D-SSOP measurement. Acquisition time was set at 150 ms, giving a frame rate of 6.7 frames per second. Are shown: the raw data (top, left), the 3D profile data (top, right), and the optical properties (absorption: bottom, left; reduced scattering: bottom, right). Note the quality of the 3D profile data as well as the quantitative values of optical properties over the image while the specimen moves.

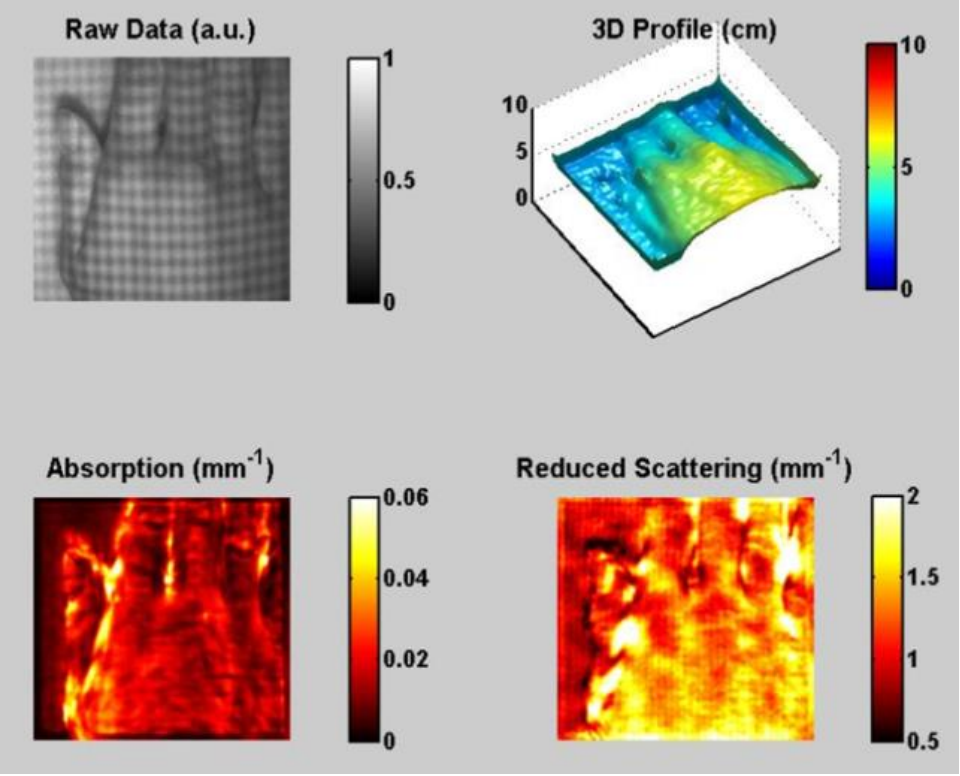

Figure. 4.1.6: Frame from the *in-vivo* hand movie. A movie of a hand was acquired with the 3D-SSOP method. Raw data (top, left), 3D profile (top, right), profile-corrected absorption (bottom, left) and reduced scattering (bottom, right) are shown.

4.1.4 Discussion

In this work we described and validated a novel method called 3D-SSOP that is capable of acquiring and processing profile-corrected optical properties maps from a diffuse medium. This method relies on projecting a dual sinewave and extracting orthogonally in the frequency domain the DC and AC components necessary to calculate optical properties, and the phase necessary to deduce the sample's 3D profile. The 3D profile is then used to correct for errors due to the mismatch between calibration and sample surface profile, and to obtain profile-corrected optical properties from a single acquired image. It is important to highlight that this method enables quantitative optical imaging over a large field of view (>100 cm^2) in real-time and in realistic conditions for future clinical use.

This method offers two important improvements over the previous SSOP method. First, it is capable of simultaneous profile and optical properties, which enables a broad range of applications compared to methods, such as standard SSOP, that suffers from severe quantitative errors due to sample's height and angle. Second, it introduces SSOP processing in the 2D Fourier space, which along with a novel fast 2D lookup table, enables real-time processing with an average image processing time of less than 125 ms. While describing this novel processing scheme will be the subject of another publication, it is important to note that 3D-SSOP truly enables real-time imaging through both acquisition and processing. Such a feature is highly desirable to reach future clinical use.

However, this method does introduce supplementary artifacts. On top of the image degradation caused by a single phase projection, and therefore energy spectrum losses, the phase itself is noisy, leading to artifacts that are visible in the sample's 3D profile. In turn these artifacts are visible in the optical properties maps, in particular through the surface angle correction that amplifies the profile noise. Several solutions are currently being investigated to increase the resolution of SSOP and the precision of the reconstructed 3D profile and therefore reduce the profile correction noise.

Finally, this method remains to be integrated within a preclinical imaging setup and tested through preclinical experiments towards enabling real-time tissue endogenous chromophore quantitative imaging. The possibilities offered by such a system are particularly interesting in surgery where feedback regarding the status and function of tissue is required in real-time.

4.1.5 Conclusion

The 3D-SSOP method allows for real-time imaging of profile-corrected tissue properties from a single acquired image. In this article, we presented the principles of this method and evaluated its performance onto tissue mimicking phantoms and *in vivo*, in comparison with standard profile-corrected Spatial Frequency Domain Imaging (3D-SFDI). Overall, the 3D-SSOP method performs similarly to the 3D-SFDI method, with some image degradation but with the unique property of enabling real-time profile-

corrected quantitative optical imaging. This work lays the foundation for the investigation of real-time surgical image-guidance using endogenous contrast.

4.1.6 Acknowledgments

The authors would like to thank Florin Neacsu for assistance with the SFDI acquisition software. This work was supported by NIH/NIDDK Award Number K01-DK-093603, NIH/NIDDK Award Number F31-DK-105839 and by the Dutch Center for Translational Molecular Imaging (MUSiS).

4.2 Real-time Endoscopic Optical Properties Imaging using 3D Single Snapshot of Optical Properties (3D-SSOP) Imaging

The work in part 4.2 was presented through SPIE[6] and will soon be submitted for publication with the following contributing authors:

Joseph Angelo,[1,2] Martijn van de Giessen,[3] and Sylvain Gioux[4,5]

[1]*Dept. of Medicine, Beth Israel Deaconess Medical Center, Boston, MA 02215, USA*

[2]*Dept. of Biomedical Engineering Boston University, Boston, MA 02215, USA*

[3]*Dept. of Radiology, Leiden University Medical Center, Leiden, The Netherlands*

[4]*Dept. of Surgery, Beth Israel Deaconess Medical Center, Boston, MA 02215, USA*

[5]*ICube Laboratory, University of Strasbourg, 300 Bd S. Brant, Illkirch, 67412 France*

4.2.1 Introduction

With the rapid increase in the number of minimally invasive procedures aimed at improving patient care while lowering the healthcare financial burden,[161] there has been a strong push for optical technologies to provide clinicians guidance during endoscopic procedures. This need for guidance is clearly evidenced by the development of instruments by both investigators and companies that aim at aiding visualization using techniques such as fluorescence,[48,53,99] endogenous imaging,[18,96,134] and stereoscopic imaging.[47,77,123] Unfortunately, most of these techniques are not quantitative in nature and are therefore subject to interpretation and user experience, limiting their value for being used routinely in clinical settings. With point measurements methods having established the potential of quantitative optical measurements for providing high sensitivity and specificity in many diseases and conditions, it is of paramount importance to develop

novel methods and instruments that would allow real-time optical quantitative imaging through endoscopes.

Spatial frequency domain imaging (SFDI) has recently been pushed to real-time acquisition[115,177] and is particularly well-suited for endoscopic implementation. SFDI offers a widefield, noncontact approach for acquiring optical property maps that can be analyzed over several wavelengths to produce chromophore concentrations of endogenous tissue constituents.[35,36,44] Several steps have been made to improve the technique's robustness and standard acquisition and processing times, including a fast 2-D look-up table,[35] a 3-D height correction method,[62,199] and an optimization of wavelengths for spectroscopic fitting of tissue constituent concentrations.[106] These developments led to a first-in-human pilot study that measured skin flap oxygenation during reconstructive breast surgery.[63] However, further work was needed in order to avoid motion artifacts and to approach real-time image acquisition for image-guided surgery.

Recent developments have pushed the speed of SFDI, reducing its usual requirement of 6 image acquisitions down to two[115] and even to one by using single snapshot of optical properties (SSOP) processing.[177] The single exposure acquisition and simple instrumentation of SSOP makes it amenable to the demanding environment of endoscopic imaging. Moreover, recent work has demonstrated the ability to extract phase information from a single projection while using SSOP, enabling height-corrections that

accommodate for irradiance loss due to variations in surface topography.[170] These features have led to this study that aims to provide quantitative endoscopic imaging.

The work presented in this article introduces a proof-of-concept endoscopic implementation of a functional widefield imaging technique that provides quantitative maps of absorption and reduced scattering optical properties as well as surface topography in real-time. SSOP acquisition and processing is utilized for speed and simplicity of instrumentation along with SFDI calibration and modeling for robust quantitative measurement. This study validates the developed system to accurately and precisely measure optical properties and height maps of tissue-mimicking phantoms and further demonstrates video acquisition of a moving phantom and an in vivo sample.

4.2.2 Materials and Methods

4.2.2.1 Spatial Frequency Domain Imaging

Spatial frequency domain imaging (SFDI) has been widely discussed in the literature and so will only be briefly introduced here. It is well known that the spatial response of a point source of light in turbid media can be described by a point spread function, s-PSF, which depends on the subsurface optical properties and radial distance from the source.[52] SFDI uses the medium's calibrated response to spatially modulated light to obtain the spatial modulation transfer function, s-MTF, the Fourier domain equivalent of the s-PSF. The s-MTF is obtained through the analysis of the diffuse reflectance R_d measured from

an intensity sinewave projection. Solving the inverse problem at each image pixel enables spatially resolved mapping of the medium's absorption and reduced scattering properties.[36,44]

This work utilizes the fundamentals of SFDI to acquire and process R_d measurements in the spatial frequency domain, thereby enabling optical property measurements. In practice, the intensity I of a sinusoidal wave at location x and spatial frequency f_x must be a linear combination of both an AC signal and a DC offset, as shown in part 4.1 (we cannot project a negative intensity):

$$I_i(x, f_x) = M(x, f_x)\cos(f_x \cdot x + \Phi_i) + I_{DC}(x) \tag{19}$$

where I_{DC} is the DC offset and $M(x, f_x)$ is the modulation amplitude of the AC signal, and φ is the phase. The modulation amplitude $M(x, f_x)$ can be obtained through various demodulation techniques, and though our work utilizes Fourier demodulation method, the most widely used method for SFDI is a three-phase demodulation where three sequentially projected sinusoidal waves with varying phase φ are acquired in order to isolate the contribution of $M(x, f_x)$ in $I_i(x, f_x)$. $M(x, f_x)$ is directly related to the sample's diffuse reflectance R_d by

$$M(x, f_x) = I_0 \cdot \mathrm{MTF}_{sys}(x, f_x) \cdot R_d(x, f_x) \tag{21}$$

as previously shown in Eq. 21 with I_0 as the source intensity and MTF_{sys} as the modulation transform of the optical system. In order to isolate R_d, a calibration

measurement is made on a reference phantom with known optical properties (and therefore known R_d) to account for both I_0 and MTF_{sys}. Spatial frequency domain measurements, as opposed to other spatially resolved measurements, have the advantageous multiplicative nature of system frequency response contributions, and these terms are accounted for with a simple division-based correction as shown in Eq. 22:

$$R_d(x, f_x) = \frac{M(x, f_x)}{M_{\text{ref}}(x, f_x)} \cdot R_{d,\text{ref,pred}}(f_x) \tag{22}$$

where $M_{\text{ref}}(x, f_x)$ is the reference phantom's modulation amplitude and $R_{d,\text{ ref, pred}}(f_x)$ is a model prediction of the reference phantom's diffuse reflectance. One can see that this assumes each measurement has the same source intensity and collection efficiency, and so the reference phantom should ideally have the same surface height and profile as the sample. Otherwise, a profile correction technique should be used to ensure measurement accuracy (discussed below in section 4.2.2.3).

Once the R_d of a sample is known, we utilize a model based 2-D look-up table method that can generate optical property maps given the R_d at a minimum of two spatial frequencies, a DC (planar illumination, f_x = 0) and an AC measurement, the latter typically around $f_x = 0.15\text{mm}^{-1}$ 0.2mm^{-1} for skin.[35] This modest requirement of the $R_{d,\text{ DC}}$ and $R_{d,\text{ AC}}$ measurements enables the use of single snapshot of optical properties imaging, a video-rate acquisition technique in the spatial frequency domain.

4.2.2.2 Single Snapshot of Optical Properties

Our lab recently developed a novel spatial frequency domain technique called single snapshot of optical properties (SSOP) that allows for video-rate acquisition of optical properties.[170,177] Long acquisition times (fewer than 1 frame per second, fps) are prone to motion artifacts created by a moving sample and are unable to capture dynamics of motion or changing optical properties. Long acquisition times are also not suitable for endoscopy, which requires at least a rate of 10 fps for proper visualization.[176] SSOP uses spatial-frequency filtering and single sideband (SSB) demodulation to recover the optical reflectance signal from the projected carrier wave from both the AC and DC components of a single sinusoidal projection. This minimizes the acquisition time to the length of a single exposure, which is simply limited by optical throughput and collection efficiency.

In this work we utilize the line-by-line Fourier transform method originally presented in 2013.[177] After the 1-D Fourier transform is performed line-by-line over the entire raw image, an ideal frequency filter separates the DC and AC components of the Fourier image. A simple inverse Fourier Transform of the DC spectrum recovers the DC image. SSB demodulation is performed on the AC image to remove the carrier frequency and recover the AC response image. These DC and AC images correspond to the components of the signal in Eq. (19) and, once calibrated using Eq. (22), provide the R_{d_DC} and R_{d_AC} components needed to utilize a 2-D look-up table and generate optical property maps.

4.2.2.3 Profile Correction

It is often difficult to control the surface height and profile of a sample, and so a profile-correction method was developed by utilizing the distance-dependent phase-shifting behavior of angled sinusoidal projections.[62] Profile corrections are absolutely crucial for both SFDI[62,199] and SSOP[170] as varying sample height causes uncorrected measurements of absorption and reduced scattering properties. Hence, this work also implements and demonstrates the need for a height-based correction. Note: in endoscopic imaging geometry, it seems more intuitive to describe the sample's position as an absolute measure in space in terms of distance from the endoscope as opposed to a 'height' from an arbitrary ground.

With our endoscope implementation, several parameters of a given measurement change along with the sample's distance from the endoscope, e.g. projected spatial frequency and the radiance of source intensity. However, each of these parameters can be calibrated and accounted for over a range of distances by using the same principles demonstrated previously.[62,170] For any given parameter, calibration measurements on a reference phantom are made at several known distances from the endoscope and the parameter is fit to a regression as a function of distance. Then, for any given sample distance, this parameter is known and can be corrected. First, the sample's distance from the endoscope must be measured.

This work utilizes a Fourier transform profilometry technique in order to measure the

sample's surface topography. Using the same fringe pattern for both profilometry and SSOP, the phase of a sample is measured using 1-D line-by-line Fourier processing previously demonstrated.[159] Once the phase is measured for the reference phantom at several known distances, a distance vs. phase relationship is made and can be utilized for a sample of unknown height.[200] Therefore, a phase measurement is simultaneously taken for every pixel of a sample, and for every pixel a distance is calculated. Finally, this distance measurement then gives the distance-dependent factors their correction based on the calibration regressions.[62]

4.2.2.4 System Design

Figure 4.2.1(a) depicts the optical design of the endoscopic imaging system. The fundamentals of imaging in the spatial frequency domain are preserved, starting with a light source. Given a source with a fiber output, lenses L_1 and L_2 are used to expand and collimate the beam onto mask M of a sinusoidal pattern. Since SSOP only requires a single pattern, the need for a digital micro-mirror device (DMD) or other type of variable projector can be replaced by a simple mask. The image of the illuminated pattern is then collimated by L_3 and polarized by linear polarizer P_1 as it is sent through the projection channel of the endoscope and onto the sample. The reflected light is imaged through the collection channel of the endoscope. The collimated output is cross-polarized with respect to P_1 by linear polarizer P_2 and then imaged by objective lens L_4 onto the CCD. The entire endoscope is shown in Fig. 4.2.1(b), while the optical channels of the working end of the endoscope are shown in Fig. 4.2.1(c).

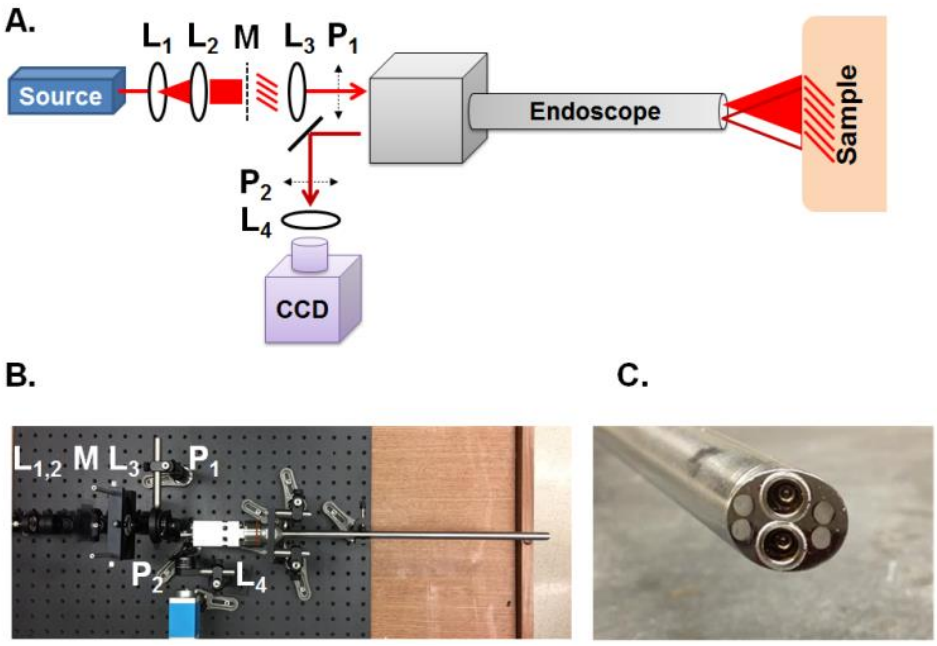

Figure 4.2.1: (a) A schematic of the optical system: a laser source is expanded and collimated by lenses L_1 and L_2, passes through a mask of a sinusoid printed onto a transparency and is collimated by L_3 into the projection channel of the endoscope. The polarizers P_1 and P_2 ensure specular light removal. The collection channel of the endoscope sends light through L_4 where it is imaged onto a CCD camera. (b) A photograph of the optical system. (c) The distal end of the endoscope showing the projection and collection channels.

Figure 4.2.2 compares the projection characteristics of (a) standard widefield structured illumination with (b) endoscopic structured illumination used in this work. Both systems have an image projection that undergoes a phase shift as a function of distance from the projector. While widefield illumination systems have an almost constant projected spatial frequency or are approximated as such, this endoscopic implementation has a non-negligible monotonic decrease is spatial frequency with increased distance due to the viewing angle of the endoscope (45°). This varying spatial frequency is accounted for by first calibrating over several known distances and then measuring the samples height, as described above.

Much of the data flow follows standard widefield SFDI and SSOP processing implemented on a custom-developed MATLAB code (Mathworks, Natick, MA) that was further adapted for this work. This code has been previously validated in past experiments.[62,63,170,177]

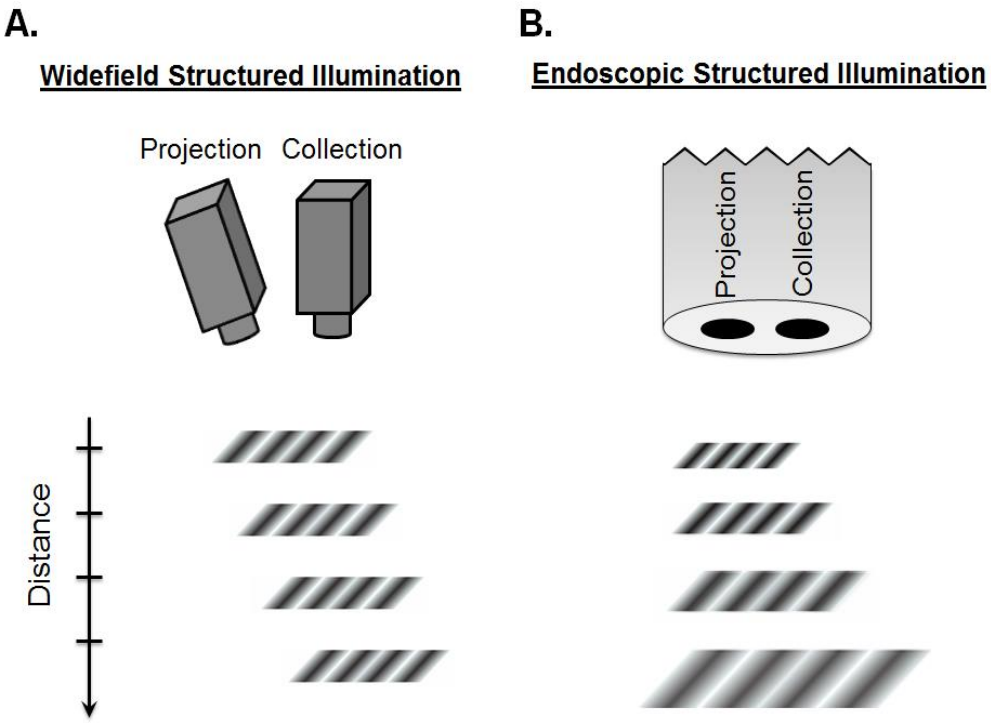

Figure 4.2.2: Schematic demonstrating the projection and collection characteristics (a) a common widefield setup and (b) our endoscopic system. Both systems use the phase shift in the projected sinusoid to measure distance. However, the endoscope system has a field of view dependent on distance, and so this variation is characterized during calibration.

4.2.2.5 Calibration

4.2.2.5.1 Flat Homogeneous Phantom

Fixed distance measurement: to first validate the accuracy and precision of extracting optical properties without the involvement of profile correction, a flat, homogeneous,

tissue-mimicking phantom with known optical properties was used as a sample and placed at a fixed distance for measurement and calibration. The phantom was fabricated with silicone and used India Ink and titanium dioxide to adjust for absorption and scattering properties, respectively.[10] The phantom's known optical properties (μ_a= 0.032 mm^{-1} and μ_s' = 0.99 mm^{-1} as measured by widefield SFDI) were used as gold standards for the measurements made using this endoscopic SSOP system.

Multi-distance measurement: to then validate the system for generating optical property and distance maps over varying distances, the same flat homogeneous phantom was measured at each calibration distance (4 thru 9 cm at 1 cm increments). Validating against the expected values, distance-based corrected optical property measurements and profile maps were compared with non-corrected optical property measurements for accuracy and precision.

4.2.2.6.2 Hemispheric Phantom

In this experiment, a hemispherical tissue-mimicking phantom was used in order to assess the profile acquisition and distance-based correction of a curved surface. This silicone phantom was made to have similar optical properties as the flat homogeneous phantom described above by using India Ink and titanium dioxide to control absorption and scattering, respectively (0.025 mm^{-1} and 1.05 mm^{-1}). In order to also test the accuracy of extracted optical properties over time and sample location, a video was acquired of the

hemispherical phantom placed on top of the flat homogeneous phantom as it is moved in three dimensions.

4.2.2.6.3. In-vivo measurement

To demonstrate the endoscopic real-time acquisition of optical properties and profilometry in vivo, a video of a hand in motion was taken with the same flat homogeneous phantom as the background.

4.2.3 Results

4.2.3.1 System Design

The optical design shown in Fig. 4.2.1(a) has minimal components and can be relatively inexpensive depending on the choice of source, endoscope, and camera. The NIR source used in this system has been built and described in recent work.[176] For this embodiment, we utilized two 1W laser diodes operating at 660 nm (LDX-3115-660, LDX Optronics, Maryville, TN) along with current and thermoelectric cooler controllers (ITC300, Thorlabs, Newton, NJ). The laser module is integrated to the endoscope optical system with a 1mm multimode fiber optic cable (BFY1000LS02, Thorlabs) and the light is then shaped using two 35 mm focal length biconvex lenses L_1 and L_2 (LB1811, Thorlabs) for illuminating the sinusoidal projection pattern, M. The projection pattern M was printed onto transparency film using an office laser printer. The endoscope used was a dual-imaging, rigid endoscope (Schölly, Inc., Worcester, MA). The projection lens L_3 was a75

mm focal plano-convex lens (LA1765, Thorlabs). A pair of linear polarizers, P_1 and P_2 (PPL05C, Moxtek, Inc., Orem, UT) helped reduce specular reflections on the proximal end of the endoscope. A simple plano-convex objective lens was used for L_4 (#45-508, Edmund Optics, Barrington, NJ) that imaged the sample onto a 14-bit CCD camera (pco.pixelfly usb, PCO, Romulus, MI).

4.2.3.2 Flat Homogeneous Phantom

Fixed distance measurement: The flat homogeneous phantom was imaged at 6cm, the same height as the reference phantom (see Fig. 4.2.3). At this distance, the field of view of the entire CCD was 5.7 x 7.6 cm. Signal loss towards the edges of the collected image was too low for proper processing, and so a mask (480 pixel diameter circle) was used to throw away unusable pixels, slightly decreasing the field of view. Also, close to the mask edge there are apparent artifacts due to this loss of signal, and so all analyzed data was taken from the dotted rectangular ROI (310 x 405 pixels, 3.39 x 4.42 cm) in the center of view. In Fig. 4.2.3(a), the measured absorption of 0.033 ± 0.00037 mm^{-1} was very accurate to the expected value of 0.032 mm^{-1}. Likewise, in Fig. 4.2.3(b) the measured reduced scattering 0.96 ± 0.0079 mm^{-1} was very close to its expected value of 0.99 mm^{-1}.

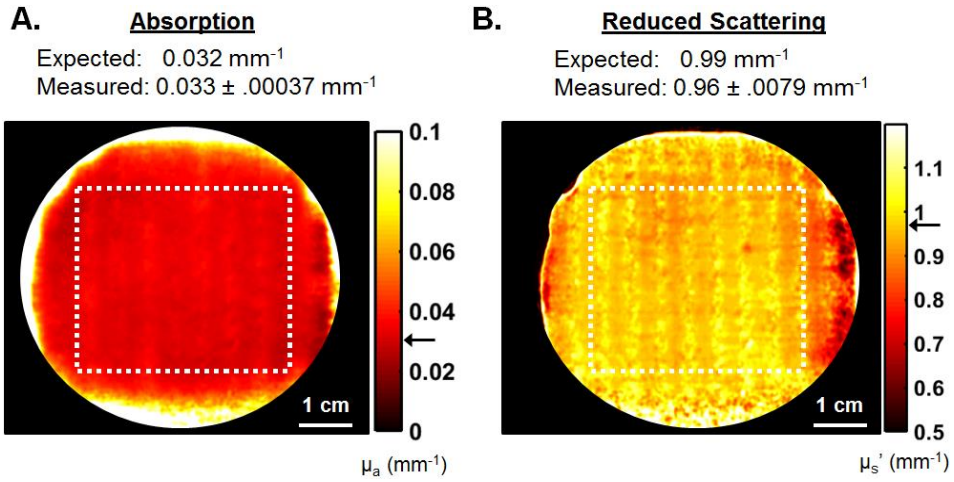

Figure 4.2.3. A flat homogeneous phantom was measured 6 cm from the distal end of the endoscope and (a) absorption and (b) reduced scattering properties were generated. Analysis was done on the white-dotted ROIs.

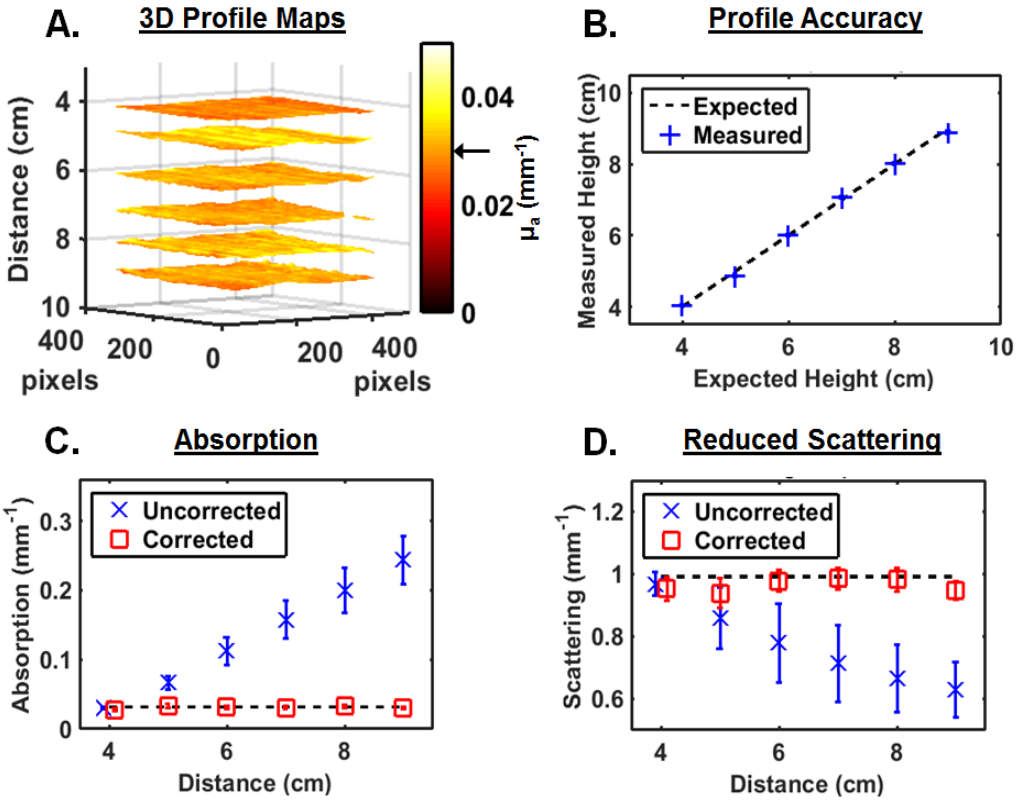

Figure 4.2.4: A flat homogeneous was measured from 4 to 9 cm in 1 cm increments. (a) The surface topography for all 6 measurements are plotted with the color map showing absorption values. (b) The topographical accuracy is shown by analyzing the ROI for each distance measurement. The analyzed (c) absorption and (d) reduced scattering values for the distance-corrected measurement and the uncorrected measurement demonstrate the need for distance-correction.

Multi-distance measurement: The flat homogeneous phantom was measured from 4 to 9 cm in 1 cm increments (see Fig. 4.2.4). The sample profile maps are shown in Fig. 4.2.4(a) with the color showing absorption values. In Fig. 4.2.4(b) the measured distance is compared with the known distance of the phantom from the endoscope and shows high accuracy at each distance with a maximum error of 1.3 mm. Each plotted point is the average height within the ROI and includes error bars. In Figs. 4.2.4(c) and (d), the uncorrected measurements (blue x's) were referenced against a phantom at 4cm. The uncorrected measurements lose accuracy rapidly as the sample distance increases, changing by nearly an order of magnitude for absorption and reduced by 0.36 mm^{-1} for scattering. In comparison, the corrected measurements (red squares) show fairly accurate and precise values over the distance range, staying within 0.004 mm^{-1} for absorption and within 0.05 mm^{-1} for scattering.

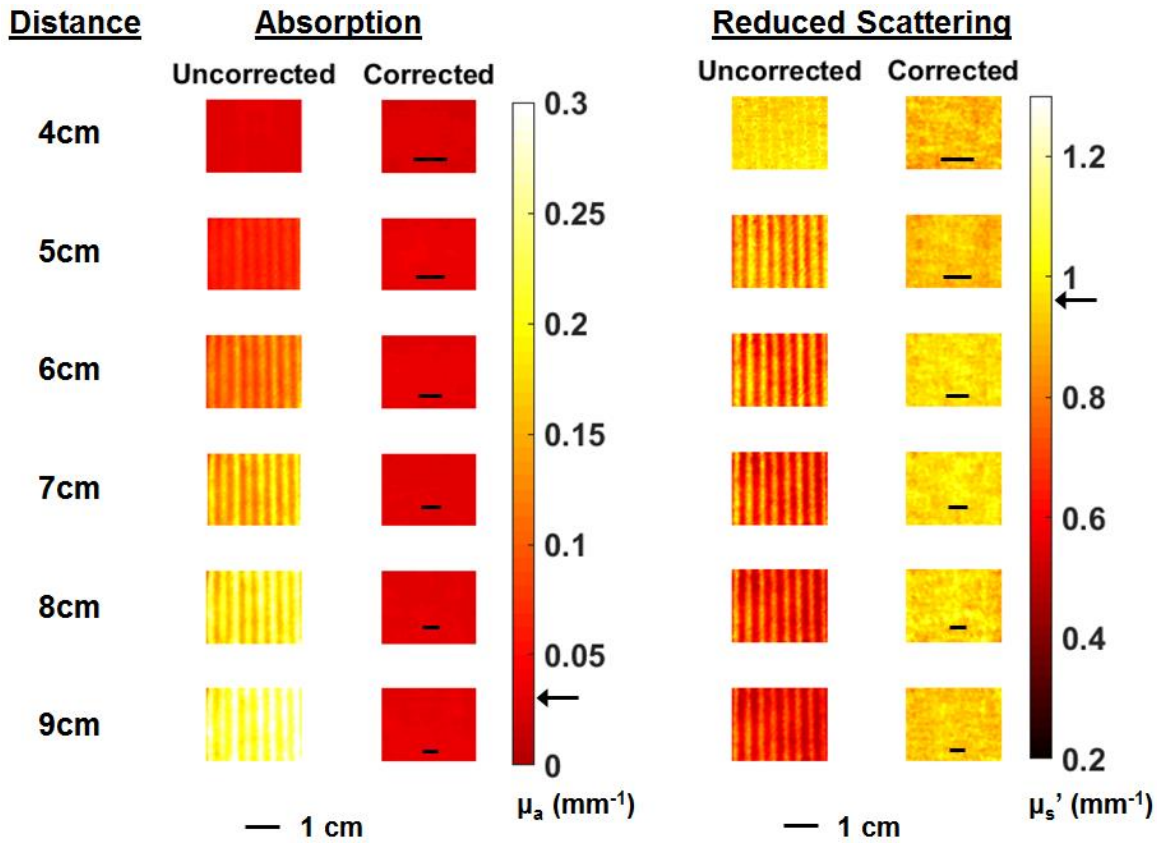

Figure 4.2.5: Absorption and reduced scattering maps measured on a flat homogeneous phantom from 4 to 9 cm. These maps demonstrate the divergence of accuracy when not correcting for sample distance. The 1 cm scale bar varies with increased sample-distance from the endoscope, as does the field of view.

To demonstrate the general degradation of optical property maps when profilometry is not used, the absorption and reduced scattering maps are presented in corrected and uncorrected formats in Fig. 4.2.5. The large color scale range is to capture the large variations in the uncorrected maps. These maps demonstrate not only the large deviation in the average optical properties measured, but also a large increase in standard deviation, with absorption error going from 0.0019 mm^{-1} (corrected) to 0.032 mm^{-1} (uncorrected) and scattering going from 0.048 mm^{-1} (corrected) to 0.13 mm^{-1}. The scale bar given at

each height represents 1 cm and demonstrates the correlation between increasing field of view and distance.

4.2.3.3. Hemispheric homogeneous phantom

Figure 4.2.6 shows data collected and processed from the real-time acquisition of optical properties for a moving hemispherical phantom and a flat homogeneous background. The video was acquired with a 85ms exposure time, and thus a framerate of approximately 11 frames per second (fps). The raw data inside the ROI is shown in the upper left frame, and the three extracted measurements of 3D profile (top right), absorption (bottom left), and reduced scattering (bottom right) come from this single raw image. The hemispherical phantom and the flat homogeneous background phantom are translated in the transverse plane in a random manner, showing stable optical property measurements in time and space. The phantom's translation was done by hand, and so slight variations in depth occur. The variations in height mean the field of view is not constant, but a scale bar that represents the scale at a distance of 7 cm is presented. The latter half of the movie captures a large translation in depth and shows stable measurements throughout. Slight optical property artifacts, especially for absorption, occur at the base of the hemispherical phantom and tend to ripple laterally around it.

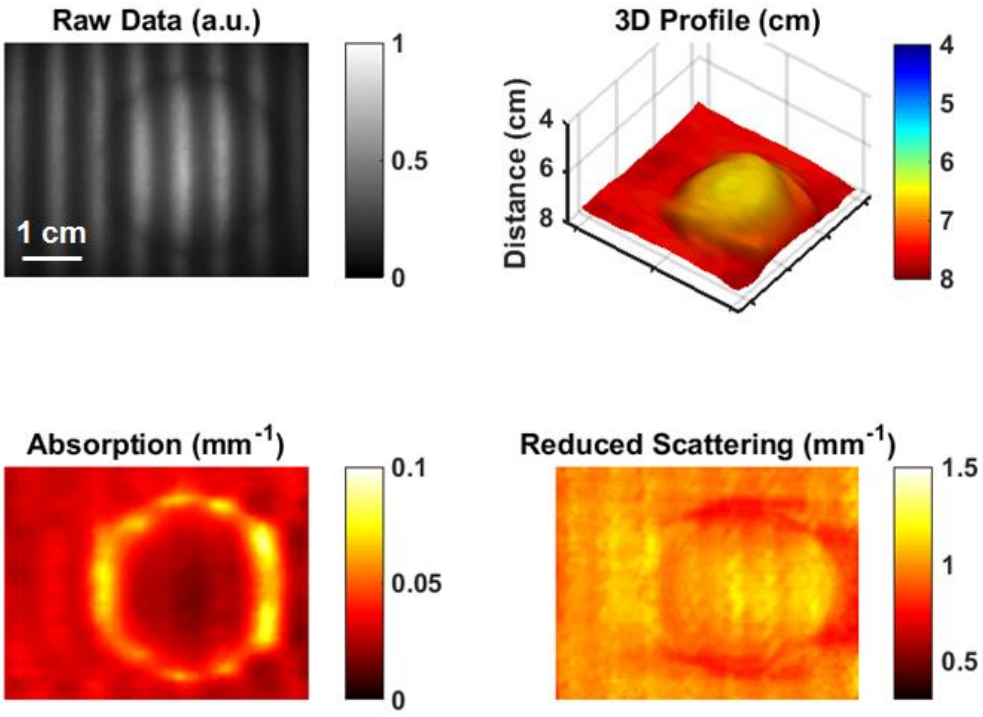

Figure 4.2.6: A hemispherical phantom resting on a flat homogeneous phantom was measured at video rate (~11 fps). Every frame of collected raw data generated a 3D profile, absorption, and reduced scattering maps. Note: since the scale changes with distance, this scale bar is given for 7cm.

4.2.3.4. In-vivo measurement

Figure 4.2.7 shows the in-vivo experiment with real-time acquisition of optical properties of a hand in motion. In the background is the flat homogeneous phantom previously used, and its position is held constant throughout the experiment. The video was acquired with a 85ms exposure time (~11 fps), and each ROI frame of raw data (top left) produced the three extracted measurements of 3D profile (top right), absorption (bottom left), and reduced scattered (bottom right). The hand is moved laterally over a static background, showing stable optical property and 3D profile maps throughout. Similarly to Fig. 6, the variations in height mean the field of view is not constant, so a scale bar that represents

the scale at a distance of 7 cm is presented. Slight optical property artifacts are seen outlining the hand, as well as rippling laterally from the hand.

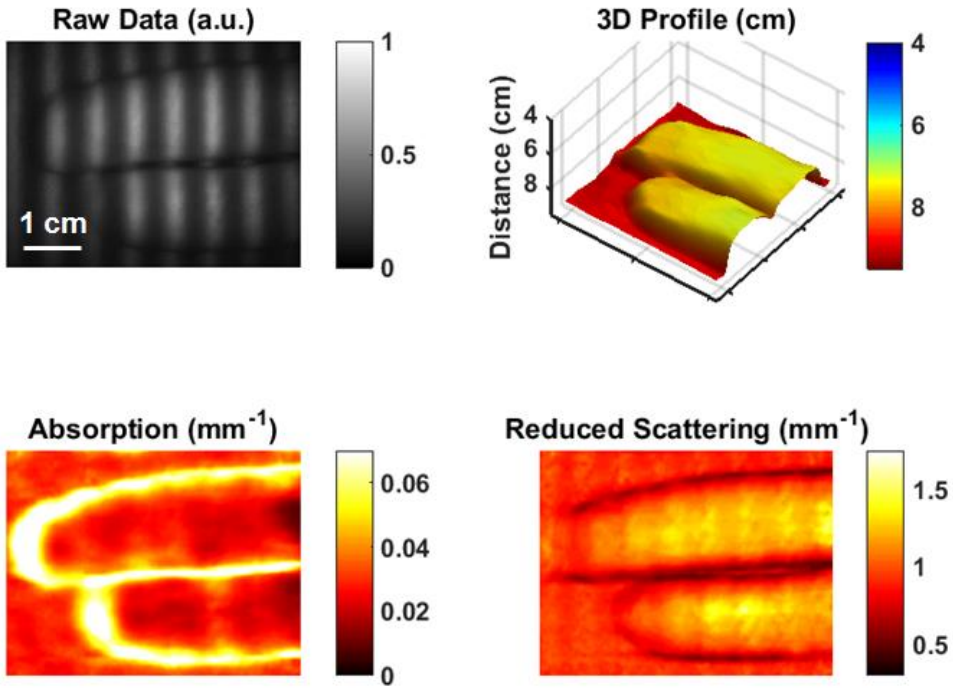

Figure 4.2.7: An *in vivo* sample (hand) is measured at video rate as it passes into view over a homogeneous flat phantom.

4.2.4 Discussion

In this work we introduced a novel implementation of single snapshot of optical property (SSOP) imaging capable of acquiring widefield optical property and 3D profile maps in real-time. This technique relies on the projection of a single 1D-sinusoidal illumination pattern that is then imaged and decomposed into components of AC, DC, and phase for further processing in the spatial frequency domain.[35,170,177] Calibration at multiple distances is done in order to calculate optical property and 3D profile maps and to also

account for system parameter variations due to changes in the sample distance. The context for this work is focused on enabling quantitative surgical guidance, and while this work demonstrates a benchtop proof-of-concept system toward this goal, several factors should be considered for future work.

During surgery, the field of view is likely to change continuously due to the handling of the endoscope or the *in-vivo* sample's motion itself, and so real-time acquisition is crucial to eliminate motion artifacts while imaging. The video framerate demonstrated in these experiments is approximately 11 frames per second, but it should be noted that this technique's framerate is only limited by the time of a single exposure, and so improved throughput and collection efficiency in an optimized system would greatly reduce the exposure time and increase the framerate of this technique. Ideally the acquisition speed would be greater than 15 fps to offer a smooth viewing experience, though cardiac dynamics have been seen in a similar technique done in widefield at rates of 50 fps.[59]

Given the intended use of this technique, sample distance variation will most likely be happening continuously during imaging. As shown here, endoscopic SSOP imaging necessitates the use of profilometry correction. As distance is increased, absorption map averages fall by nearly an order of magnitude while reduced scattering was reduced by 0.36 mm^{-1}. Moreover, artifacts become apparent as the measured sample's distance gets farther from the reference phantom's distance (see Fig. 4.2.4). The use of profilometry keeps absorption and reduced scattering map averages within 0.004 mm^{-1} and 0.05 mm^{-1},

respectively. Because the single snapshot collects phase information as well, there is no additional acquisition time necessary to measure the sample's phase, though calibration steps are added in order to create distance-dependent correction factors. Profilometry corrections are therefore necessary for quantitative imaging of samples with variations in height and also help reduce imaging artifacts.[62,199]

The spatial information extracted from a single raw image allows for rapid acquisition, but the cost will be some loss of spatial resolution. The videos presented (Figs. 4.2.6 and 4.2.7) show a slight loss in image resolution from the raw image collected to the optical property maps, along with minor ringing artifacts due to the demodulation process relying on filtering in the Fourier domain. However, these image degradations tend to be stable and minor in the variations in optical properties. No measure of image quality or viewer experience has been presented in this work because this work is simply a proof-of-concept and a more optimized system will greatly improve image quality. This optimization will mostly entail increased optical efficiency and throughput, along with optimization of SSOP processing framework.

In order to progress this technique from endoscopic real-time imaging of optical properties to surgical guidance will first entail incorporating a second wavelength in order to enable oximetry imaging. Previous work has demonstrated the ability of spatial frequency domain imaging to perform accurate oximetry measurements in tissue with only two spatial frequencies and two wavelengths,[106] making endoscopic real-time

oximetry imaging readily achievable by adding a second wavelength to the benchtop system presented here. The next concern will be to perform real-time acquisition along with real-time feedback. Two fundamental hurdles need to be considered: 1) demodulation time and 2) inversion of measured diffuse reflectance to sample properties, e.g. optical property or chromophore maps. Demodulation time is currently estimated at 100ms, though this processing is currently being done in MATLAB and could certainly be optimized for real-time feedback. While the current processing time to invert diffuse reflectance maps to optical properties is typically on the order of 1 second, we recently demonstrated that this inversion time could be reduced significantly to approximately 10ms.[8] Altogether this work lays the foundation of real-time quantitative optical imaging through an endoscope and its clinical translation.

4.2.5 Conclusion

The endoscopic SSOP system allows for real-time imaging of profile-corrected optical properties through an endoscope. In this work, we presented the principles and methods of this system's design and processing scheme, along with a validation of its accuracy on tissue mimicking phantoms and a demonstration of its *in-vivo* imaging capabilities. In addition, the method presented is also capable of measuring the sample profile and corrects for variations in the sample's distance from the endoscope to obtain accurate optical property maps from a single image acquisition with a slight loss in image resolution. This work utilizes previous investigations into widefield imaging of optical properties to lay the foundation for real-time, endoscopic surgical image-guidance using endogenous contrast.

4.2.6 Acknowledgements

The authors would like to thank Bruce Tromberg for his thoughtful contributions to this project, Intuitive Surgical and Jonathan Sorger for their support with instrumentation.

4.2.7 Funding

Funding was provided by: National Institutes of Health (NIH) (K01-DK-093603, F31-DK-105839); France Life Imaging; University of Strasbourg and ICube Laboratory.

4.3 Real-time Endoscopic Oxygenation using 3D Single Snapshot of Optical Property (SSOP) Imaging

The work in part 4.3 has been partially presented through SPIE[7] with the following contributing authors:

Joseph P. Angelo,[1,2] Martijn van de Giessen,[3], and Sylvain Gioux[4,5]

[1]*Dept. of Medicine, Beth Israel Deaconess Medical Center, Boston, MA 02215, USA*

[2]*Dept. of Biomedical Engineering Boston University, Boston, MA 02215, USA*

[3]*Dept. of Radiology, Leiden University Medical Center, Leiden, The Netherlands*

[4]*Dept. of Surgery, Beth Israel Deaconess Medical Center, Boston, MA 02215, USA*

[5]*ICube Laboratory, University of Strasbourg, 300 Bd S. Brant, Illkirch, 67412 France*

4.3.1 Introduction

Surgical guidance poses a unique scenario and restricts the parameters for potential technological solutions. Space in the operating room is highly limited and time is costly in both patient care and patient management. Ideally, the technique would be noncontact and measure broadly so as to not disrupt the surgeon's field of view and it would provide quantitative feedback in real-time. The importance of oxygen in all aspects of wound healing has been well studied for many years,[73,74] and so tissue oxygenation measurement has shown a prominent role in assessing tissue viability.[69] My associated lab has recently retroactively reviewed the utility of an optical tissue oxygenation monitoring device to save transplanted skin flaps, and this technology has shown promise in clinical trials by giving surgeons tissue oxygenation feedback at a single point, influencing surgical

decisions that dramatically decreased the rate of skin flap loss in breast reconstructive surgery.[98,143] However, due to its single point sampling this technique requires contact with the tissue and relies on global effects, and visualization of the complete surgical field would be advantageous. Furthermore, no adaptation of this technique, or a full-field technique, has been made suitable for minimally invasive surgery.

A great difficulty in quantitative, non-contact endoscopic imaging is the unstable distance of the sample over time and space. Furthermore, the endoscope will most likely be handheld, making it difficult to keep a steady field of view and therefore requiring rapid measurement acquisition. Our lab has focused heavily on finding solutions for quantitative imaging methods that are ideal for real-time,[177] profile-corrected,[170] suitable for endoscopic implementation,[6] and presented here is our work on endoscopic oxygenation imaging in real-time.

This work is a direct continuation of the single-wavelength endoscopic imaging presented in chapter 4 part 2, and so, in an effort to limit redundancy, aforementioned system details will be kept brief.

4.3.2 Materials and Methods

4.3.2.1 Endoscopic Imaging Considerations in the Spatial Frequency Domain

Due to the simultaneous, widefield measurement inherent to spatial frequency domain imaging, techniques have been developed in order to push the acquisition requirements

from 6 images with standard SFDI,[35,36] down to 2 images with alternating DC and AC patterns,[115] to 1 single image.[177] As discussed in chapter 2 section 4, the system response of diffusive medium, e.g. skin tissue, to a spatial frequency projection of light will depend on the tissue's absorption, reduced scattering, and the spatial frequency used. The above-mentioned methods push the speed of acquisition in the spatial frequency domain, but assume the tissue sample matches the optical reference, and this is very much unlikely for clinical imaging. With the help of recent work in phase extraction from spatial frequency patterns for widefield optical property imaging,[170] we recently submitted work demonstrating a real-time, profile corrected endoscopic imaging system utilizing SSOP at a single wavelength.[6]

Briefly, some of the unique challenges circumvented with our endoscopic SSOP system will be addressed here, and further information can be seen above in chapter 4 section 2. First, given the strong influence of sample distance on the accuracy of measured optical properties (see Fig. 4.2.4 and Fig. 4.2.5), it is imperative to invoke a profile-correction method. Similar to past spatial frequency domain profile-correction methods,[62,170] this system utilizes slight angle between the projection and collection of light to create and measure phase-sensitive structured illumination (see Fig. 4.2.2). Unique to our endoscopic implementation, we use the phase-sensitive projection also as the optical property measurement.[6] This helps increase signal to noise by increasing overall throughput of the system. Next, with a changing working distance (distal end of endoscope to the sample) comes a change in the spatial frequency of the projected pattern

due to the viewing angle of the endoscope (45°) (see Fig. 4.2.2). Because the system-response analysis depends on spatial frequency, this system requires a calculation of spatial frequency at every pixel. This is achieved by calibrating the spatial frequency dependence with distance prior to measurement (see section 4.2.2.3). Once these considerations are met, standard SFDI processing is done to obtain optical property maps at 670 nm and 808 nm, and least square fitting takes the measured absorption maps and fits them to chromophore concentrations of oxy- and deoxyhemoglobin to then obtain oxygenation.

4.3.2.2 Endoscopic Dual-Wavelength Imaging System

The single-wavelength endoscopic imaging system previously developed (see Fig. 4.2.1) was amended to accommodate a second wavelength channel such that 670 nm and 808 nm could be acquired simultaneously. In Fig. 4.3.1 A), a schematic depicts the dual-wavelength endoscopic imaging system with lenses L_1 and L_2 collimating light onto image mask M before being imaged in the projection channel of the endoscope by lens L_3. The projection and collection channels at the distal end of the endoscope are cross-polarized with XP to remove specular reflections. The collected light is relayed by lens L_4 and split with a dichroic mirror to separate wavelength channels. Fig. 4.3.1 B) and C) are photographs of the actual endoscope used.

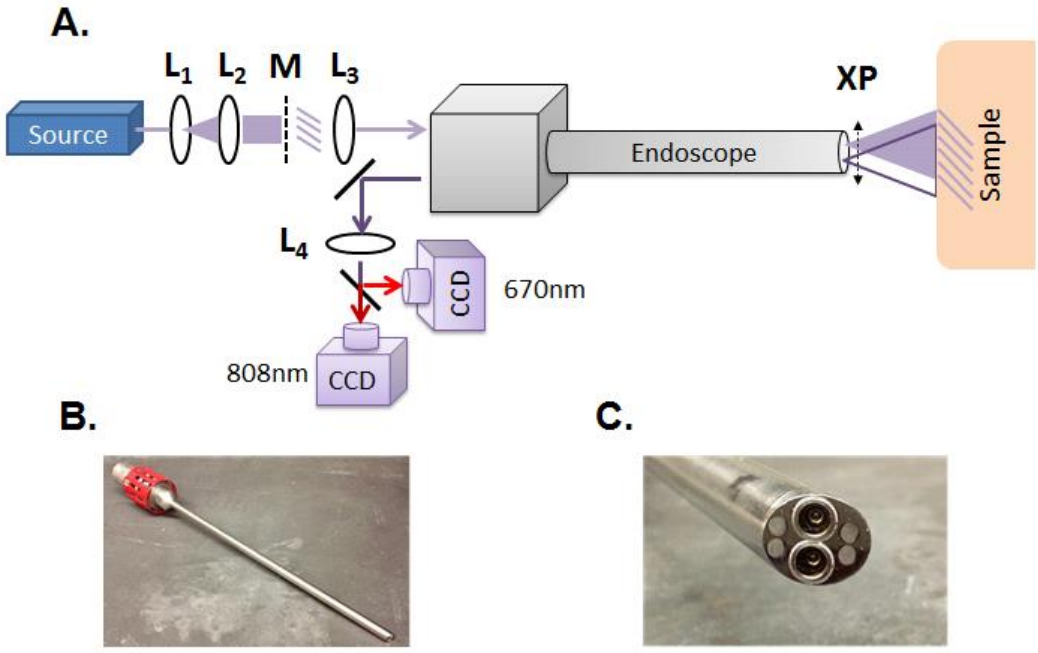

Figure 4.3.1: A) Schematic of the dual-wavelength endoscopic imaging system with lenses L_1 and L_2 collimating light onto image mask M before being imaged in the projection channel of the endoscope by lens L_3. The projection and collection channels at the distal end of the endoscope are cross-polarized with XP to remove specular reflections. The collected light is relayed by lens L_4 and split with a dichroic mirror to separate wavelength channels. B) and C) are photographs of the actual endoscope used.

4.3.2.3 Experiments

4.3.2.3.1 Crosstalk validation

In order to confirm that the channels were accurate for both single channel and dual channel use, and to ensure that no crosstalk between channels was present, a fixed-distance measurement was made on a flat homogeneous phantom of known optical properties with the primary channel on, and with the second channel on. Statistical analysis of the resulting optical properties was used to assess the accuracy and precision in both cases for both wavelengths.

4.3.2.3.2 Multi-distance accuracy

To then validate the system for generating optical property and distance maps over varying distances, the same flat homogeneous phantom was measured at each calibration distance (4 thru 9 cm at 1 cm increments). Validating against the expected values, distance-based corrected optical property measurements and profile maps were compared with non-corrected optical property measurements for accuracy and precision for each wavelength channel.

4.3.2.3.3 In-vivo demonstration

Two arm cuff occlusion experiments were done on a healthy volunteer. Both experiments acquired video-rate images before, during, and after the occlusion was applied and oxygenation curves were generated. In the first experiment, the subject's fingers were imaged and analyzed over an ROI, while the subject's palm was measured was analyzed in the second experiment. These oxygenation and profile measurements are made from single exposures from two cameras taken simultaneously

4.3.3 Results

4.3.3.1 System Design

The optical design shown in Fig. 4.3.1(A) has minimal components and can be relatively inexpensive depending on the choice of source, endoscope, and camera. For this embodiment, we utilized two 1W laser diodes operating at 670 nm (LDX-3115-665, LDX Optronics, Maryville, TN) and one 2W diode at 808 nm (LDX-3210-808) along with current and thermoelectric cooler controllers (ITC300, Thorlabs, Newton, NJ). The laser

module is integrated to the endoscope optical system with a 1mm multimode fiber optic cable (BFY1000LS02, Thorlabs) and the light is then shaped using two 35 mm focal length biconvex lenses L_1 and L_2 (LB1811, Thorlabs) for illuminating the sinusoidal projection pattern, M. The projection pattern M was printed onto transparency film using an office laser printer. The endoscope used was a dual-imaging, rigid endoscope (Schölly, Inc., Worcester, MA). The projection lens L_3 is a75 mm focal plano-convex lens (LA1765, Thorlabs). A pair of linear polarizers, (LPVISE2X2, Thorlabs, Newton, NJ) create the crossed polarizer pair XP and helped reduce specular reflections on the proximal end of the endoscope. A simple plano-convex objective lens was used for L_4 (#45-508, Edmund Optics, Barrington, NJ) that imaged the sample onto a 14-bit CCD camera (pco.pixelfly usb, PCO, Romulus, MI).

4.3.3.2. Phantom Experiments

Figures 4.3.2 and 4.3.3 present the crosstalk validation experiment, showing 670 nm and 808 nm, respectively, in mono- and dual-wavelength acquisition. Both figures were fixed-distance measurements at 7 cm from the distal end of the endoscope. In Figure 4.3.2, the results of optical property measurements at 670 nm are shown to be highly accurate for both mono- and dual-wavelength imaging. Analysis of the ROIs of each map show highly accurate optical properties, with absorption within 0.001 mm^{-1} from the expected value of 0.033 mm^{-1} for both cases and reduced scattering within 0.04 mm^{-1} of the expected 0.91 mm^{-1}. For the remainder of the data processing, all data analysis was done within the ROIs shown.

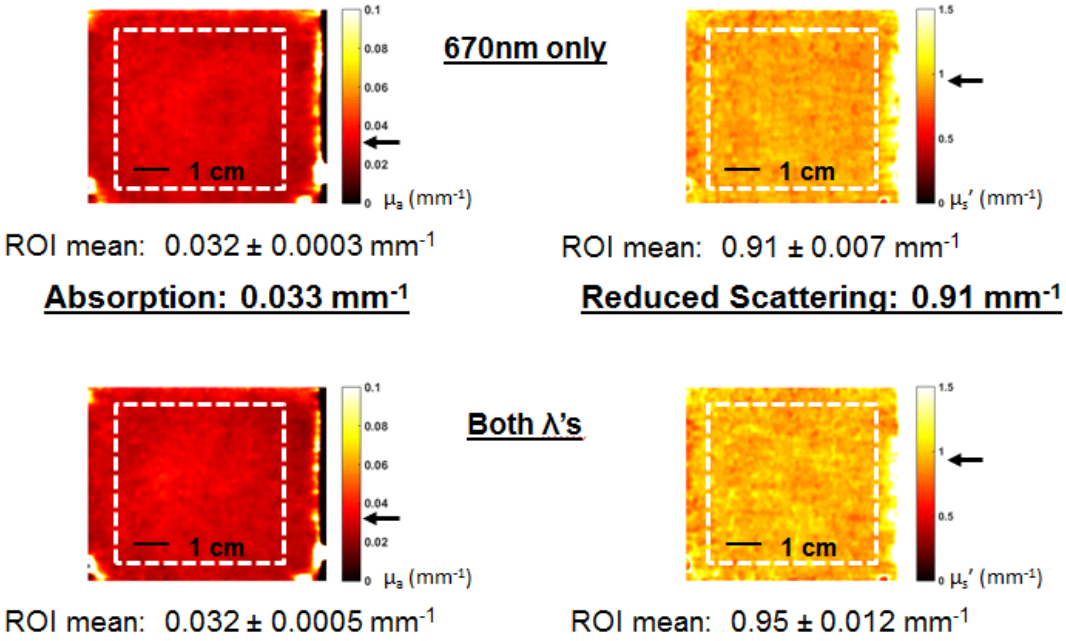

Figure 4.3.2: Optical property maps of fixed-distance measurements at 670 nm for both mono- and dual-wavelength imaging. ROI analysis shows highly accurate optical property measurements for both cases, showing no signs of crosstalk between wavelengths.

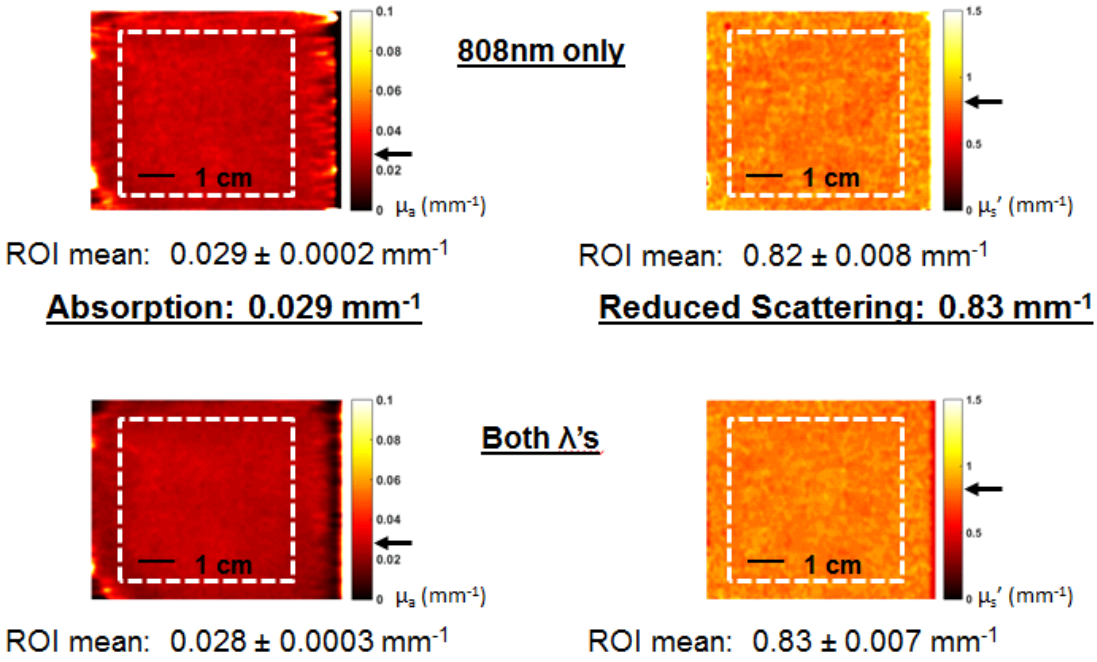

Figure 4.3.3: Optical property maps of fixed-distance measurements at 808 nm for both mono- and dual-wavelength imaging. ROI analysis shows highly accurate optical property measurements for both cases, showing no signs of crosstalk between wavelengths.

In Figure 4.3.3, the results of optical property measurements at 808 nm are shown to be highly accurate for both mono- and dual-wavelength imaging. Analysis of the ROIs of each map show highly accurate optical properties, with absorption within 0.001 mm^{-1} from the expected value of 0.033 mm^{-1} for both cases and reduced scattering within 0.04 mm^{-1} of the expected 0.91 mm^{-1}. For the remainder of the data processing, all data analysis was done within the ROIs shown.

To further validate the accuracy of the dual-wavelength measurement, Figure 4.3.4 shows multi-distant measurement results from taking a flat homogeneous optical phantom over a distance of 4 to 9 cm in 1 cm increments. Both 670 nm and 808 nm measurements were accurate over the range of distances for the distance-corrected maps for both absorption and reduced scattering, while uncorrected optical properties tended to diverge quickly once the sample left the reference distance. The data points were averaged pixel values over the ROIs shown in Fig. 4.3.2 with standard deviations as error bars.

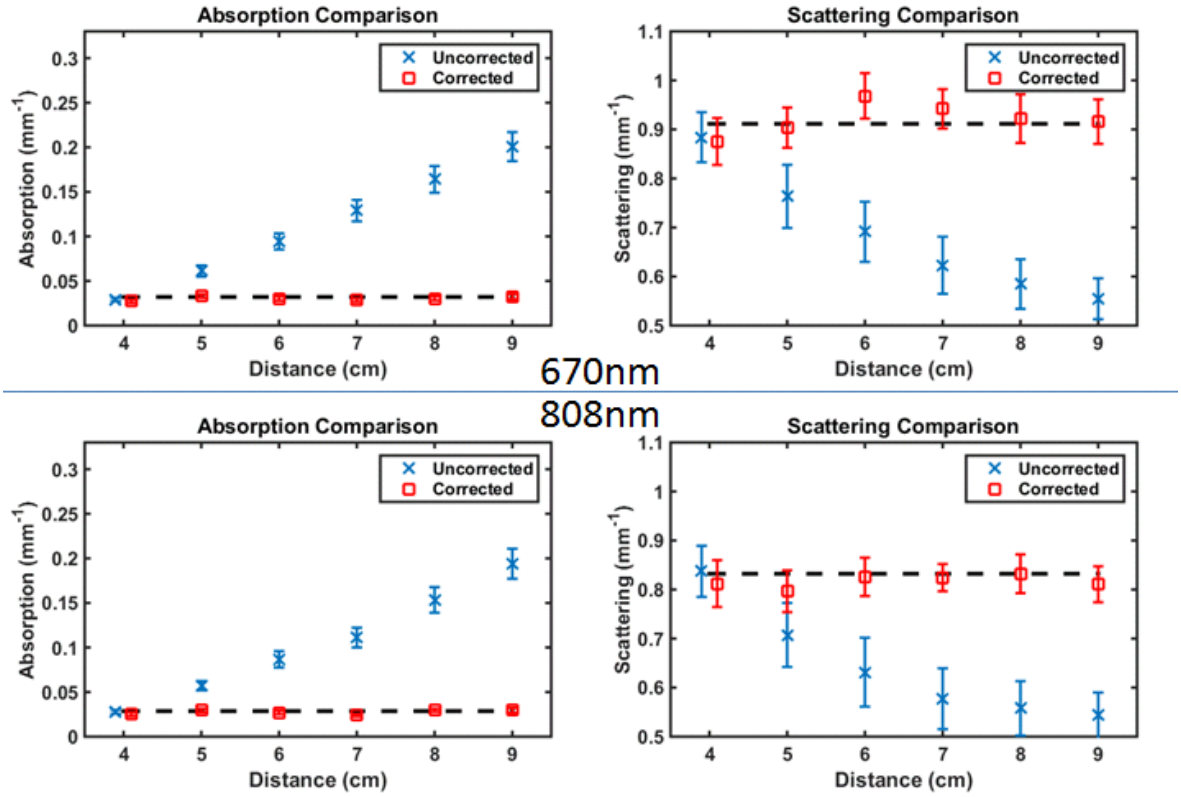

Figure 4.3.4: Multi-distant measurement results from taking a flat homogeneous optical phantom over a distance of 4 to 9 cm in 1 cm increments.

4.3.3.3 In vivo oxygenation measurements

Two in vivo samples were measured, both arm cuff occlusions with a baseline, occlusion, and recovery state, for percent oxygen saturation. Oxygenation video acquisition was made at 2 frames per second of a finger of a hand of the occluded arm, as shown in Figure 4.3.5. Each frame of the video is acquired from single exposures of two cameras taken simultaneously. This figure shows a single frame near the end of the occlusion cycle in the recovery state, with oxygen saturation percent coming back to a stable ~80%, as it started as in the baseline state. The upper left panel shows the raw data collection by

the 670 nm channel normalized to its max signal. The upper right panel shows the profile map as distance from the distal end of the endoscope and coloration also representing distance. The lower left panel shows the average pixel value, over time, of the black-dashed rectangle ROI in the lower right panel, demonstrating the predictable oxygenation curve of an occluded tissue. Finally, the lower right panel shows the oxygenation map of the sample for each frame. Note: the background of the sample was a black piece of paper, resulting in 0% oxygenation between fingers.

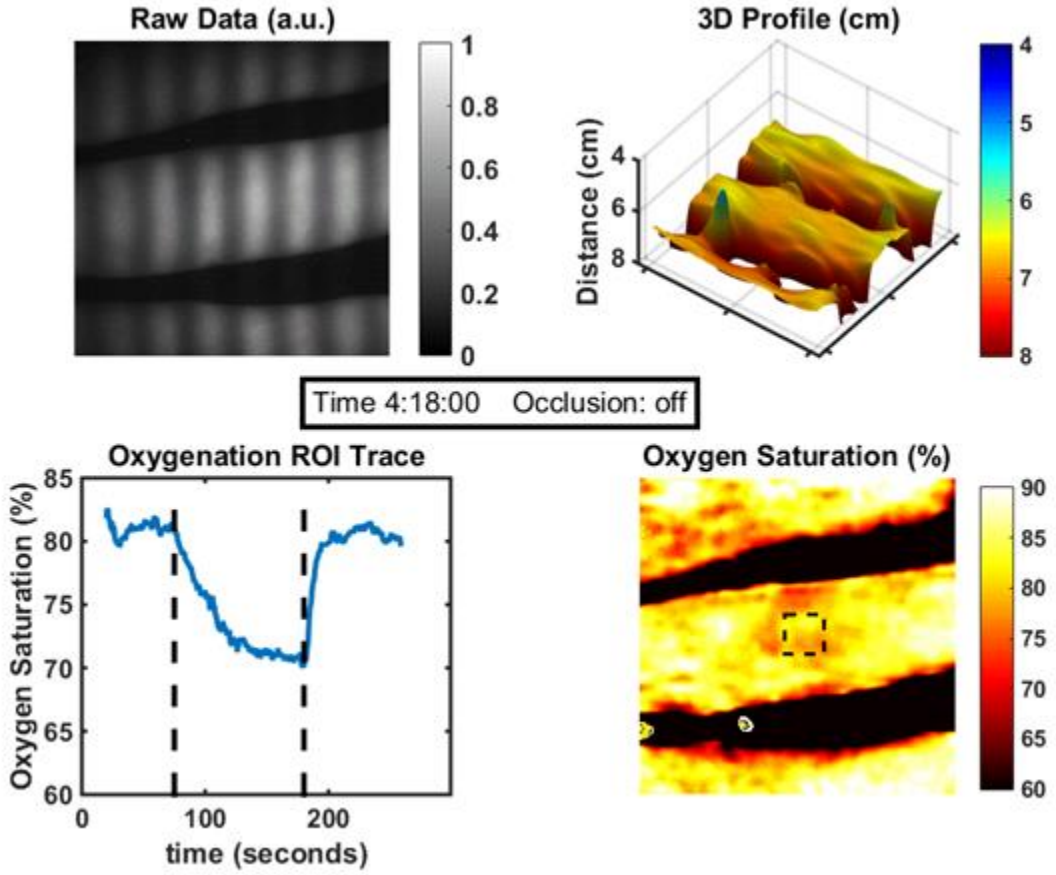

Figure 4.3.5: In vivo sample of a finger measured throughout a cuff occlusion cycle. This figure is a single frame of oxygenation video acquisition at 2 frames per second, with the sample in the recovery state. Note: the ROI trace is taken from the black-dashed rectangle in the lower right panel of the oxygenation map. Note: no scale bar is given since the field of view varies with sample distance, though the upper right hand panel captures approximately 5 x 5 cm.

The last sample was the palm of a hand of an occluded arm with oxygenation measurements acquired at 2 frames per second. Again, single frame exposures are acquired simultaneously from both cameras to obtain profile and oxygenation measurements. Figure 4.3.6 shows the baseline state of the palm, with the oxygenation map on the left panel and the right panel showing the oxygenation time trace of the black-dashed ROI.

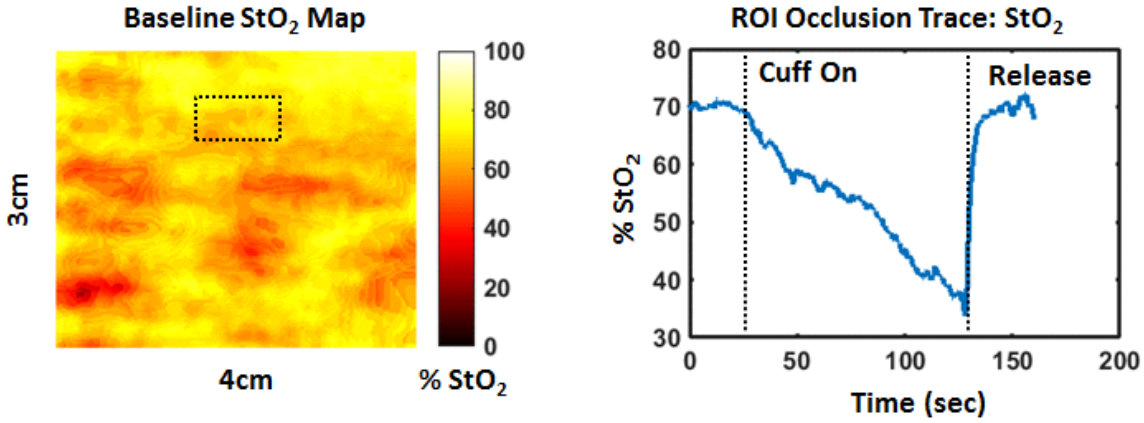

Figure 4.3.6: The in vivo oxygenation measurement of a palm of an occluded hand. This figure is a single frame of oxygenation video acquisition at 2 frames per second, with the sample in the baseline state. Note: the ROI trace is taken from the black-dotted rectangle in the left panel oxygenation map. Note: the palm measurement was taken closer to the endoscope than the fingers, resulting in a smaller field of view.

4.3.4 Discussion

The crosstalk validation experiment results shown in Fig. 4.3.3 demonstrate the negligible, if any, effects of using dual-wavelength imaging versus the mono-wavelength imaging. Both imaging schemes show accurate results for both absorption and reduced scatter measurements, within 0.001 mm^{-1} for all absorption maps and 0.04 mm^{-1} for all

reduced scattering maps.

The multi-distance validation experiment results shown in Fig. 4.3.4 demonstrate the necessity for distance correction. For both wavelengths and for both optical property maps, uncorrected measurements of optical properties diverge rapidly from the expected values as the sample distance increases from the reference distance of 4 cm.

Both in vivo demonstrations of real-time oxygenation measurement, seen in Figs. 4.3.5 and 4.3.6, show the potential of this novel technique for endoscopic tissue viability assessment in vivo. Acquisition rates were limited to 2 frames per second due to low throughput of 808 nm. This low throughput was largely due to non-optimized optics and low output power of the 808 nm laser diode. The framerate possible for 670 nm is > 10 frames per second (see chapter 4 section 2).[6] Though this overall framerate of 2 frames per second is hardly 'real-time' it should be explicitly stated, again, that acquisition rates are limited to single exposure times. Therefore, by simply increasing laser power, optimizing optical throughput, or decreasing sample distance, exposure time can be greatly reduced and framerate increased.

Though this work has primarily focused on the novel introduction of real-time, endoscopic oxygenation imaging, there is yet more to be gained from the profile measurement taken during acquisition. Recently, an endoscopic profile measurement technique has helped detect and classify colon polyps because while their coloration is

very similar to healthy tissue, their unique topography provides high contrast in 3D imaging.[47] There has been a great push in technology and methodology in order to make these 3D imaging techniques real-time and robust,[171] and these developments can greatly aid surgical vision and help discern between tissue states using quantitative sensing.[172] This quantitative profile analysis approach could be potentially useful to assist the oxygenation maps in tissue viability assessment in future work.

4.3.6 Conclusion

This work presents improvements to our novel real-time, single-wavelength, endoscopic imaging system for measuring tissue optical properties. Highlighting dual-wavelength imaging design, validation, and in vivo demonstrations of oxygenation measurements, this work expands upon both widefield and endoscopic imaging by achieving oxygenation measurement based off single exposures. These improvements push the limits of current surgical guidance and biomedical imaging techniques.

CHAPTER 5: CONTRIBUTIONS TO REAL-TIME SPATIAL FREQUENCY DOMAIN PROCESSING

Chapters 3 and 4 highlight the real-time acquisition techniques developed for widefield optical property imaging, leading to real-time fluorescence correction and oxygenation imaging. However, with acquisition time being reduced to a single exposure, the bottleneck to real-time feedback lies in the processing. The "rapid" processing techniques used to convert spatial frequency domain measurements to optical property maps were certainly fast enough for the original acquisition methods, but with the advent of real-time acquisition, a commensurate processing technique is needed. Hence, presented here is work directed to this end of real-time processing to enable real-time feedback for clinical imaging and surgical guidance.

5.1 Ultra-fast optical property map generation using lookup tables

The work in section 5.1 is published in the Journal of Biomedical Optics[3] with the following contributing authors:

Joseph Angelo,[1, 2] Christina R. Vargas,[3] Bernard T. Lee,[3] Irving J. Bigio,[2,4] and Sylvain Gioux[2,5]

[1] Beth Israel Deaconess Medical Center, Department of Medicine and [3] Department of Surgery, 330 Brookline Avenue, Boston, MA 02215, United States

[2] Boston University, Department of Biomedical Engineering and [4] Department of Electrical and Computer Engineering, Boston, MA 02215, United States

[5] ICube Laboratory, University of Strasbourg, 300 Bd S. Brant, 67412 Illkirch, France

5.1.1 Introduction

Rapid quantitative imaging of tissue optical properties, namely absorption (μ_a) and reduced scattering (μ_s'), has long been a challenge in the field of biomedical optics. The recent introduction of Spatial Frequency Domain Imaging (SFDI) provides a transformative approach capable of measuring optical properties over a large field-of-view.[44] In principle, SFDI relies on the analysis of the tissue response to structured illumination (patterns of light) in the spatial frequency domain in a multi-pixel manner over an entire field-of-view at once.[35,36] More specifically, the spatial-frequency-dependent response, called the modulation transfer function (s-MTF), is calibrated using a phantom with known optical properties to determine the tissue diffuse reflectance (R_d), which is then used to extract the optical properties using a light propagation model.

While the method is rapid, SFDI has until recently involved the measurement of several images to form maps of optical properties, typically a total of 6 images (2 spatial

frequencies at 3 phases), although a method employing only a single spatial frequency and 3 phases has also been described. Recent developments in acquisition methods reduced the number of images necessary to extract optical properties from 6 to 2,[92] and even from 6 to a single image with the method called Single Snapshot of Optical Properties (SSOP).[177] In their most advanced implementations, such methods enable profile-corrected measurements of optical properties in a single snapshot, in turn facilitating true real-time acquisition of optical properties.[170]

Unfortunately, while acquisition methods can be performed in real-time, the processing is still commonly achieved post-acquisition. The most rapid processing method employs a lookup table approach, by which solutions for diffuse reflectance are generated from a light propagation model (diffusion, Monte-Carlo) or empirically with various spatial frequencies and optical properties.[35,124,132] Such a method allows one to directly link a calibrated diffuse reflectance measurement at known spatial frequencies to a unique solution of optical properties (μ_a and μ_s'). However, because it necessitates interpolations within the lookup table for each pixel in the image, this method is still time-consuming (seconds), preventing the use of SFDI for true real-time imaging of optical properties.

In this work, we present novel forms of lookup tables allowing rapid extraction of optical properties from the measurement of calibrated diffuse reflectance. We propose two solutions that do not necessitate interpolations and thus dramatically reduce computation time. The first method consists of a hyper-dense linearized lookup table, and the second

invokes an analytical representation of the lookup table. These methods are described, implemented, and compared to the standard lookup table method in terms of precision, accuracy, and computation time. Combined with real-time acquisition, this work facilitates real-time quantitative optical imaging of tissue properties.

5.1.2 Materials and Methods

The two methods described in this work are based on a previously developed lookup table (LUT).[35] This standard LUT method uses "white" Monte Carlo simulation (WMC, with zero absorbance) to model the spatially-resolved impulse response, i.e. the steady-state diffuse reflectance $R_d(\rho)$, of a collimated point-source illumination for a given set of μ_a, μ_s', n, and g, which is then Fourier transformed to determine the spatial frequency response of the diffuse reflectance.[85,157] To generate the standard LUT, WMC was used to simulate 10^7 photons into a homogenous medium with index of refraction n = 1.4 and anisotropy factor g = 0.9. The model used a detector with a numerical aperture of 0.22 and the radial bins were sampled in increments of $\Delta\rho$ = 0.09 mm, allowing a maximum spatial frequency of over 5 mm^{-1}. This process is repeated over several optical properties, and stored in a table that associates the diffuse reflectance at two spatial frequencies with a unique pair of optical properties. Recovering optical properties therefore involves measuring the diffuse reflectance of the sample and searching the table to find the corresponding optical property values (hence the name "lookup table"). With this method, it is important to understand that the optical properties are linearly sampled, so we refer to this method as the Linear OP LUT. Using this method, the measured R_d

values are used to search through the nonlinear mapping of R_d against the tissue properties in the Linear OP LUT table, and then μ_a and μ_s' are acquired using cubic spline interpolation. For our Linear OP LUT, the resolution of the sampled optical properties was 0.001 mm^{-1} and 0.01 mm^{-1} with a range of [0, 0.3] mm^{-1} and [0.3, 3] mm^{-1} for μ_a and μ_s', respectively, with a table size of 81,571 points (see Linear OP LUT in Fig. 5.1.1).

To avoid the time consuming searching and interpolation steps required for the standard Linear OP LUT, an LUT linear with respect to R_d (Linear R_d LUT) was made by interpolating linearly sampled R_d values from 0 to 1 by 500 points within a high resolution Linear OP LUT (0.0001 mm^{-1} and 0.001 mm^{-1} resolution with a range of [0, 0.3] mm^{-1} and [0.3, 3] mm^{-1} for μ_a and μ_s', respectively, with a table size of 8,105,701 points). The resolution of the R_d linear sampling is chosen so that measured R_d values can be found directly in the table by rounding their value to the nearest increment of 0.02, without interpolation (see Linear R_d LUT in Fig. 5.1.1). Given a sample's R_d values, the LUT's corresponding indices can be calculated by parameterizing the linear R_d grid and rounding to the nearest vertex to acquire μ_a and μ_s'.

Using the Linear R_d LUT, each optical property table was fit to a 2D function using a nonlinear least squares solver ("fit" using MATLAB):

$$\mu_a(DC, AC) = a_1 e^{a_2 DC + a_3 AC + a_4} + b_1 e^{b_2 DC + b_3 AC + b_4} + c_1 e^{c_2 DC + c_3} + d_1 e^{d_2 AC^3 + d_3 (DC + d_4) AC^2 + d_5 DC + d_6 AC + d_7} \quad (23)$$

$$\mu_s'(DC, AC) = a_1 e^{a_2 AC + a_3} + b_1 e^{b_2 AC + b_3} + c_1 e^{c_2 AC + c_3} + d_1 e^{d_2 AC + d_3} + (d_1 + AC) e^{d_2 DC^2 + d_3 DC + d_4}, \quad (24)$$

where a_1 through d_4 are optimized parameters. Using these functions, optical properties can be directly deduced from the diffuse reflectance at low spatial frequency (noted DC here) and the diffuse reflectance at high spatial frequency (noted AC here). This is referred to as the 2D Fit LUT (see 2D Fit LUT in Fig. 5.1.1).

Figure 5.1.1 summarizes the LUT formations and workflows. The red arrows describe the formation process from Monte-Carlo simulation to the Linear OP LUT (arrow 1), to the Linear R_d LUT (arrow 2), and finally to the 2D Fit LUT (arrow 3). The blue arrows indicate the three options for workflow when using the LUTs to extract optical properties. Diffuse reflectance measurements at 2 spatial frequencies (low: DC, and high: AC) are used as inputs to the lookup tables to extract the optical properties.

The custom imaging system and associated processing has been described extensively and results have been published, including a clinical trial.[62,63] Briefly, the system utilizes a digital micro-mirror device (DMD) to project patterns of 670nm laser illumination which is cross polarized with the collection optics to minimize specular reflections in images collected on a CCD camera.

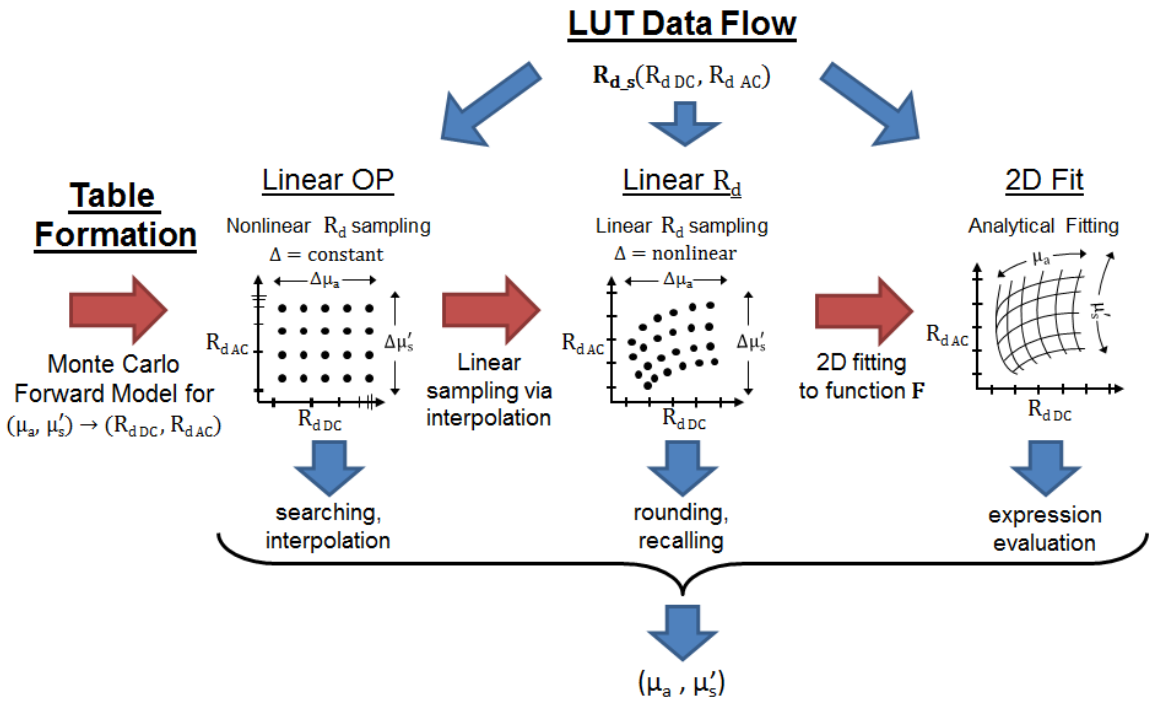

Figure 5.1.1: LUT protocols: red white arrows indicate the formation of each lookup table, from Monte-Carlo simulation, to linear Rd sampling, and finally function fitting. Blue Black arrows indicate three options for data flow and usage of each LUT. First, a sample's R_d (DC and AC) is measured and used as input. The Linear OP LUT (Left) must search and interpolate to generate optical properties, the Linear R_d LUT (Middle) uses parametric indexing to recall optical properties, and the 2D Fit LUT (Right) evaluates the function F to generate optical properties.

An array of tissue-like silicone phantoms was made using India ink (Blick Art Materials, Boston MA) and titanium dioxide (Atlantic Equipment Engineers, Bergenfield NJ) for absorption and scattering, respectively. The array was made to span the optical properties μ_a = [0.01, 0.1] mm^{-1} and μ_s' = [0.5, 2] mm^{-1}. The array was imaged using SFDI and the inversion from R_d to optical properties was then evaluated on all three LUT methods and compared to a Monte Carlo (MC) least-squares solver over square ROIs of 15 x 15 pixels.[85]

Finally, a Yorkshire pig was used as an *in vivo* model to evaluate each LUT method during realistic surgical conditions (Beth Israel Deaconess Medical Center Institutional Animal Care and Use Committee approved institutional protocol #034-2013). Abdominal skin flaps were elevated on a pair of perforator vessels, the venous pedicle was occluded, and the pedicle was released to restore tissue perfusion.

All computational processing and analyses were done on a 64bit Dell Optiplex 9020 (Dell, Round Rock TX) with an Intel Core i7-4770 CPU (Intel, Santa Clara CA). R_d inversions were repeated 100 times for each LUT type and averaged for comparison.

5.1.3 Results

Figure 5.1.2 shows the results for the phantom sample array. Agreement is seen among all three LUTs for both absorption and reduced scattering maps (Fig. 5.1.2a). ROIs were chosen to quantify the results for each phantom well (Fig. 5.1.2a) and to compare the LUT methods (Fig. 5.1.2b). All methods show low relative error compared to the MC results (μ_a %, μ_s' %): Linear OP LUT (1.3, 0.5), Linear R_d LUT (0.2, 0.09), 2D Fit LUT (1.9, 2.8). Table 5.1.1 summarizes the processing times for each method on this sample, from a single pixel to the entire image. The Linear R_d and 2D Fit LUTs exhibit better performances over the entire range. Importantly, processing shows a 100-fold improvement for an entire image (572 x 612 pixels), for both absorption and reduced scattering.

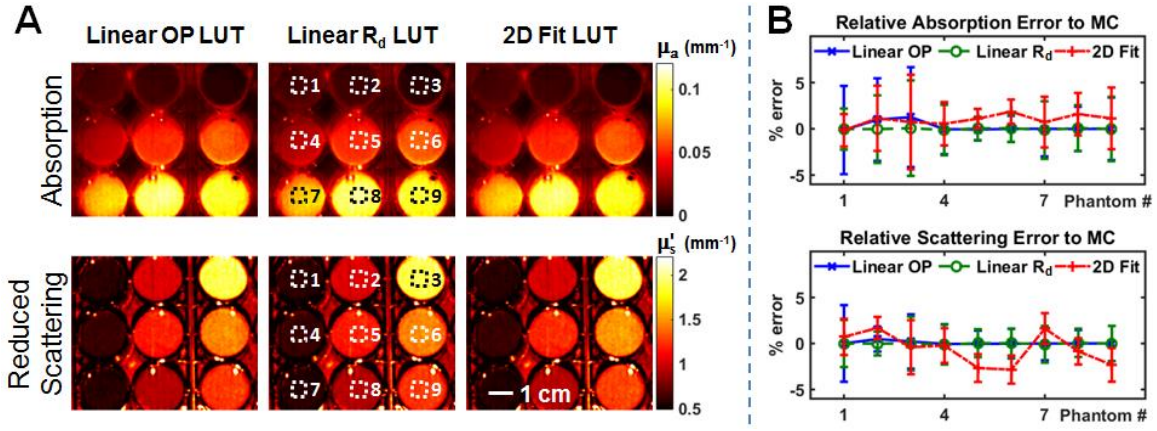

Figure 5.1.2: Phantom array measurement. A) Tissue-simulating phantom array was measured using SFDI and absorption (top row) and reduced scattering (bottom row) maps were generated using the Linear OP, Linear R_d, and 2D Fit LUTs. B) Regions of interest (dotted squares) were chosen to compare each method's accuracy. Image resolution is 512 x 672 pixels. Scale bar represents 1cm.

Table 5.1.1: Processing speeds for LUT inversion of R_d to both μ_a and μ_s' property maps.

Number of Pixels	Linear OP LUT	Linear R_d LUT	2D Fit LUT
1	0.2814 s	5.207×10^{-5} s	5.117×10^{-4} s
10 x 10	0.4801 s	1.107×10^{-4} s	5.205×10^{-4} s
100 x 100	0.5120 s	5.801×10^{-4} s	1.174×10^{-3} s
572 x 672	2.492 s	0.0175 s	0.01881 s

The *in vivo* results are shown in Figure 5.1.3. All LUT methods show strong agreement for both absorption and reduced scattering maps (Fig. 5.1.3a). A line profile was taken across the sample (dotted lines in Fig. 5.1.3a) to quantitatively compare the LUT results (Fig. 5.1.3b). All LUTs show agreement to the MC results (μ_a %, μ_s' %): Linear OP LUT (4.1, 2.1), Linear R_d LUT (0.9, 0.6), 2D Fit LUT (1.5, 3.2).

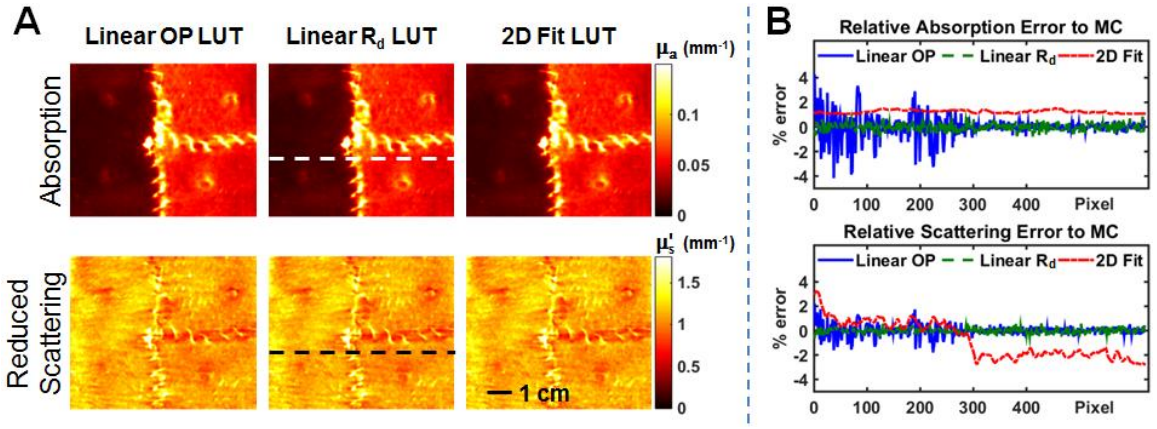

Figure 5.1.3: In vivo measurement. A) A pig skin flap vascular occlusion model was measured using SFDI and optical property maps were generated using each LUT. B) Line profiles (dotted lines) compare each method's accuracy. Scale bar represents 1cm.

5.1.4 Discussion

Both newly developed LUT methods, the Linear R_d LUT and 2D Fit LUT, decrease the processing time by a factor of ~100x by avoiding searching and interpolating with two different approaches. The Linear R_d LUT parameterizes a linear grid using the table's sampling resolution and range and rounds to the nearest vertex that matches the sample's R_d input. The 2D Fit method avoids this discrete sampling by fitting a continuous function to each surface of μ_a and μ_s' as a function of diffuse reflectance at two spatial frequencies.

Each LUT method has its own unique relationship between inversion speed, memory space, and accuracy. The standard Linear OP LUT must use interpolation for practically-sized tables, which increases the required processing time. Withal, because this table samples R_d in a nonlinear manner, increasing the sampling grid greatly increases the

searching time for each input. In comparison, the Linear R_d LUT is sampled with a parameterized grid, and so its speed is minimally affected by increased grid size because no searching occurs. However, because the table is linearly sampled, the density required to maximize accuracy at high gradients in the table is used for the entire table, resulting in a large grid that requires considerable computer memory. This could potentially be mitigated by choosing a sampling function whose density increases for higher gradients of the table. The 2D Fit LUT requires less computer memory space but has variable accuracy across the table due to under-fitting, though this accuracy could potentially be weighted toward optical property values that are more likely to occur, e.g. separate LUTs for brain, liver, or skin tissues. While the presented 2D Fit LUT was fit to the entire Linear R_d LUT, accuracy was weighted to prioritize optical properties reasonably expected for skin tissues (μ_a= [0.0035 0.192] mm^{-1}, μ_s' = [0.3 2.281] mm^{-1}). Within this range of optical properties, errors in comparing the 2D Fit LUT with ground truth does not exceed 0.004 mm^{-1} in absorption and 0.1072 mm^{-1} in scattering.

The two LUTs introduced in this work have utility in different settings. Figures 5.1.2(b) and 5.1.3(b) demonstrate the accuracy advantage of the Linear R_d LUT over other LUTs, but it is the most memory intensive. In a scenario where batch processing is occurring, the Linear R_d LUT can potentially be more accurate and 100x faster than the standard Linear OP LUT used. However, our lab is developing several techniques based on the method of SSOP imaging that are aiming towards real-time feedback, and memory is a major concern. Here, the 2D Fit LUT may be more practical since it requires only 18

parameters in memory to invert R_d values to absorption values. Likewise, if the processing scheme were moved to parallel processing or to a FPGA, the low memory requirements for the 2D Fit LUT make it a more practical choice.

As with the originally proposed standard Linear OP LUT, the Linear R_d LUT and the 2D Fit LUT are built with a two-frequency input for inverse solutions of optical properties. When using inverse solvers, the problem of degeneracy should always be considered. Here, these LUTs have no degeneracies, but they are potentially sensitive to orthogonality and noise. If two spatial frequencies are chosen that are not well separated, e.g. 0 and 0.01 mm^{-1}, then the table's orthogonality will decrease, meaning the contour lines of absorption and scattering will start to collapse and that small amounts of noise can lead to large changes in the retrieved optical properties. This is why our work and many others use higher AC frequencies (~0.2 mm^{-1}). A multi-frequency analysis is also possible for retrieving a more robust measure of absorption and scattering, and these LUTs are capable of incorporating multiple AC frequencies.

The new frameworks introduced can be applied to other lookup table processes with possibly more dimensions. For profile corrected SFDI[62] or 3D-SSOP,[170] there is the potential to include height/phase dependence among the table's input parameters for optical property mapping. In addition, it is important to note that in order to make multispectral measurements each wavelength is processed separately with the same LUT. Because wavelengths can be independently processed in parallel, processing time is

minimally affected. Given a known set of wavelengths, one could also go directly from R_d input values to hemodynamic values such as oxygen saturation. Generating these calculations after calibrating the imaging system but before the sample acquisition makes real-time feedback for surgical guidance possible.

5.1.5 Conclusion

In this work, we introduced a new framework for LUT formation and evaluated its performance on tissue-mimicking phantoms and *in vivo* in comparison with a standard OP LUT.[35] Overall, the new techniques were accurate compared to MC simulations, i.e. within 0.9% and 0.6% for Linear R_d LUT μ_a and μ_s', respectively, and within 1.9% and 3.2% for 2D Fit LUT μ_a and μ_s', respectively, and are 100x faster than the standard Linear OP LUT. These techniques help enable real-time image-guidance feedback for spatial frequency domain techniques.

5.1.6 Acknowledgements

The authors would like to thank Steve McClure for his helpful discussion and support. This work was supported by R01-DE-022820 (BL), K01-DK-093603, France Life Imaging, University of Strasbourg and ICube Laboratory (SG), and NIH/NIDDK Award Number F31-DK-105839 (JA).

CHAPTER 6: PRE-CLINICAL STUDIES OF OXIMETRY-MONITORED TISSUE VIABILITY

Chapters 3 and 4 present novel acquisition techniques to enhance image-guided surgery, supporting both fluorescence and endogenous contrast. While testing and validating these techniques is paramount for their acceptance and utility, their relevance for clinical application needs to be demonstrated further with tissue viability studies. To this point, the first part of this chapter presents a rat skin flap model for tissue viability margin assessment using both fluorescence and tissue property monitoring. Part two demonstrates the power of oxygenation imaging using spatial frequency domain imaging for sensing vascular occlusion in vivo.

6.1 A Preliminary Study of Endogenous Imaging used to Predict Tissue Viability Boundary

The work in section 6.2 is preliminary and has not been published. However, this work was done in concert with the fluorescence work in section 6.1 and the same contributing members should be mentioned:

Joseph Angelo,[1,2] Christina Vargas,[3] Hideyuki Wada,[3, 4] Bernard T. Lee (BTL),[3] and Sylvain Gioux

[1]*Division of Hematology/Oncology, Department of Medicine, Beth Israel Deaconess Medical Center and Harvard Medical School, Boston, MA 02215*

[2]*Department of Biomedical Engineering, Boston University, Boston, MA 02215*

3Division of Plastic and Reconstructive Surgery, Department of Surgery, Beth Israel Deaconess Medical Center and Harvard Medical School, Boston, MA 02215

[4]*Department of Gastroenterological Surgery II, Hokkaido University Graduate School of Medicine, Sapporo, 060-8638, Japan*

[5] *ICube Laboratory, University of Strasbourg, 300 Bd S. Brant, 67412 Illkirch, France*

6.1.1 Introduction

Necrosis is a morbidity that can lead to higher rates of infection and longer hospital stays. Unfortunately, it is associated with a number of surgical procedures, such as mastectomy skin flaps,[173] tissue transfer, among others. Though there is a strong effort to lower the occurrence of necrosis through sound surgical techniques, rates are still unacceptably high at 4.9 - 16%.[33,58,178] There is a need to provide objective guidance to predict tissue viability and to enable intraoperative intervention.

There is currently no objective measure of tissue viability in the clinic today. The standard of care is to use qualitative measures for tissue perfusion, such as skin color,

capillary refill, and temperature. The results based off these measures are shown to be unreliable and rely on the clinician's experience.[25,139]

This work investigates the potential for using widefield endogenous imaging as an early indicator of tissue viability. Profile-corrected spatial frequency domain imaging (SFDI) is used to quantitatively track several tissue parameters including absorption, reduced scattering, and hemoglobin concentrations on a rat model for skin flap necrosis. This preliminary work shows promising correlations between variations in these tissue parameters and a 7 day necrosis line determined with color imaging.

6.1.2 Material and Methods

6.1.2.1 Animal Model

For clarity, it will be stated that animals were housed in an Association for Assessment and Accreditation of Laboratory Animal Care–certified facility and were studied under the supervision of Beth Israel Deaconess Medical Center's Institutional Animal Care and Use Committee in accordance with approved institutional protocol number 030-2013. For this study, three Male Sprague-Dawley rats were imaged with an average weight of 365 g (Charles River Laboratories, Wilmington, Mass.) were induced, and anesthesia was maintained, with 2 to 3% isoflurane. Meloxicam (Bimeda, Oakbrook Terrace, Ill.) was administered subcutaneously 20 minutes before the end of surgery and at 24 hours for analgesia.

A reverse McFarlane dorsal skin flap in rats (Fig. 6.1.1) is well validated and reproducible as a skin profusion model.[108,135] However, for this preliminary study only three rats were imaged. Analysis of a representative sample is provided from a single rat. A visual example of a rat prepared for surgery is shown in Fig. 6.1.1. This also represents the control image.

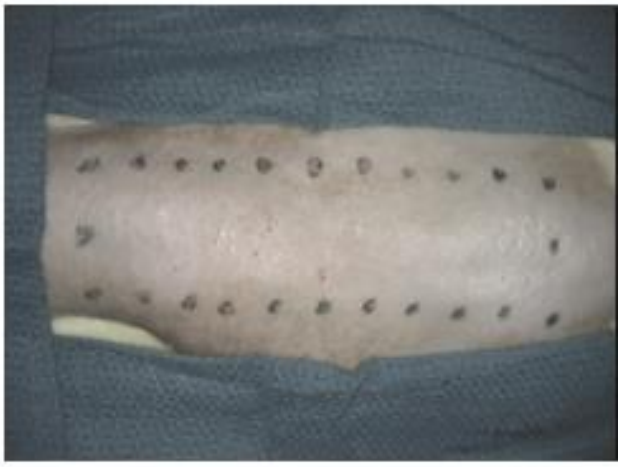

Figure 6.1.1: A color image of the control time point: a rat marked for skin flap surgery.

6.1.2.1 Spatial Frequency Domain Imaging

The details of the SFDI imaging system have been previously reported.[64] Briefly, a clinic-friendly cart houses the NIR light source, control electronics, and computer and has an adjustable imaging head on a locking mechanical arm. The NIR source is capable of projection 6 wavelengths simultaneously or in any combination of 670, 730, 760, 808, 860, and 980 nm. This source is fiber-coupled to a digital light modulator (DMD) which projects structured illumination used for SFDI analysis. The collected light is split into

one of three optical pathways: color, NIR1 (650 to 780 nm), or NIR2 (780 to 1000 nm). All three cameras are co-registered for comparison and analysis purposes.

For analysis, the spatial frequencies of 0 and 0.2 mm^{-1} were projected and processed for optical property measurements at each wavelength. These absorption coefficients were then fit with least square error to chromophore extinction spectra, such as oxyhemoglobin and deoxyhemoglobin, using Beer's Law. Two methods of fit were considered for chromophore extraction. The first used water as a chromophore to fit, and the second method set the water concentration at a fixed value of 50% and excluded 980 nm from chromophore fitting. Control images were taken preoperatively and 0 time point images were taken immediately after surgery, followed by acquisitions at 5, 10, 15, 30 minutes, and every 30 minutes thereafter.

To reduce the amount of information, line profiles were taken across the entirety of the skin flap, utilizing the surgical margins drawn in Fig. 6.1.1. The plastic surgeon boundary lines were averaged horizontally for every vertical position to form a boundary line for SFDI evaluation.

6.1.2.3 Necrosis Boundary Determination

Three independent plastic surgeons were asked to draw a line to separate what they believed were the viable and necrotic areas of the flap using the color image on

postoperative day 7. This information was used to as a gold standard to evaluate the SFDI results.

6.1.3 Results

Figure 6.1.2 represents the wealth of information from a single time point. Presented are tissue optical parameters from Rat 3 15 minutes post operation. For all 6 wavelengths, absorption and reduced scattering optical property maps are given. In Fig 6.1.2 A) a chromophore fitting was done to include 980 nm and fit for percent water concentration. B) presents the fitting excluding 980 nm and fixes the water concentration at 50% for chromophore fitting. Also presented are the power law scattering parameters log(A) and B, shown to be sensitive to nanoscale physiological changes.[154]

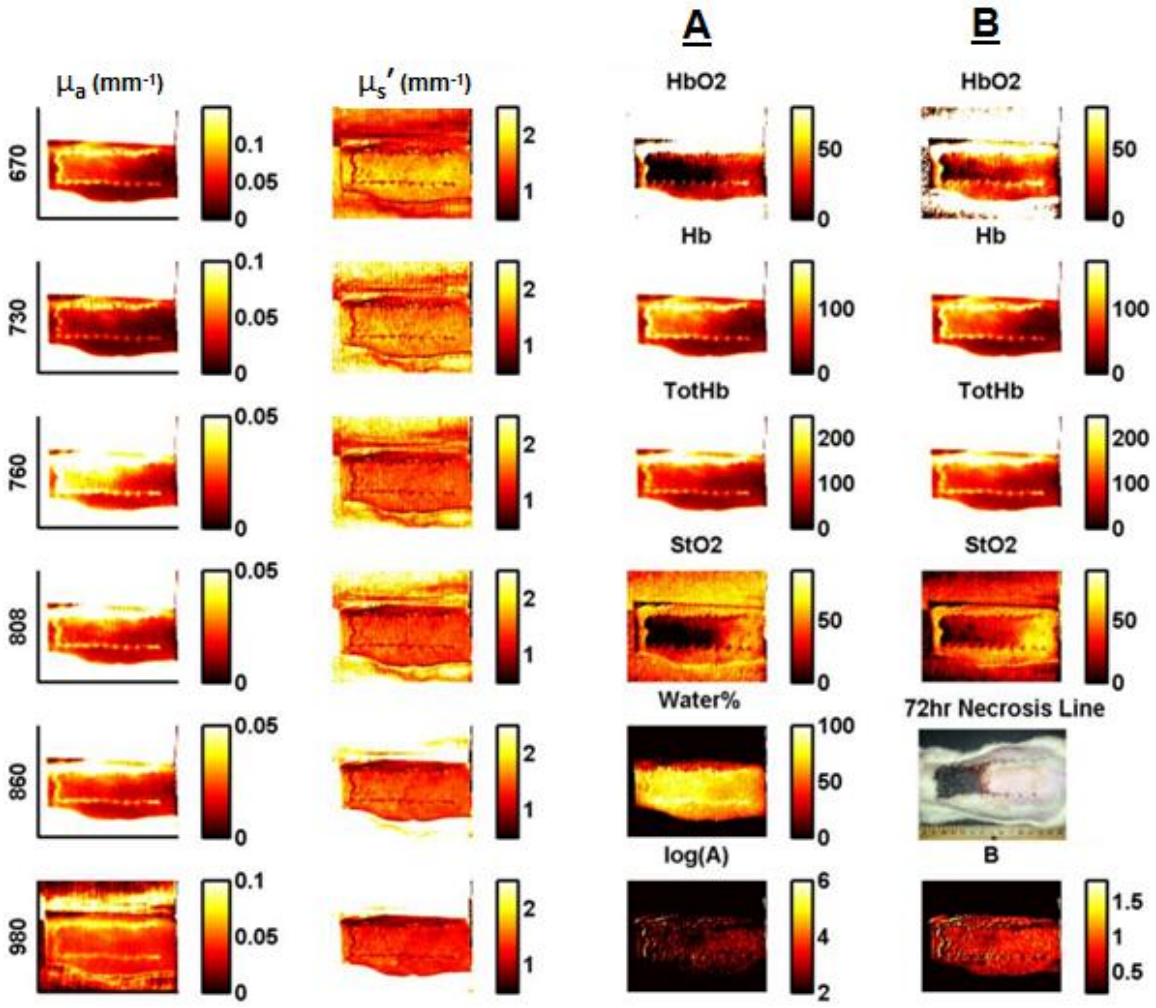

Figure 6.1.2: Tissue optical parameters given for all wavelengths and for various chromophore fittings. Also included is a 72 hour post-operative color image for a visual reference. Optical property maps are given in mm^{-1}, oxy-, deoxy-, and total hemoglobin are given in μM, and oxygenation and water are given in percent concentration.

Line profiles for several tissue optical measurements of the Rat 3 skin flap are shown in Fig. 6.1.3. The horizontal axes are pixel location in the extracted maps, 0 being at the base of the necrotic end of the flap and 430 being at the perfused, connected end of the flap. From the bulk of information in Fig. 6.1.2, the parameters that best correlated with the necrosis boundary determined by a group of three plastic surgeons (black dotted line) are represented.

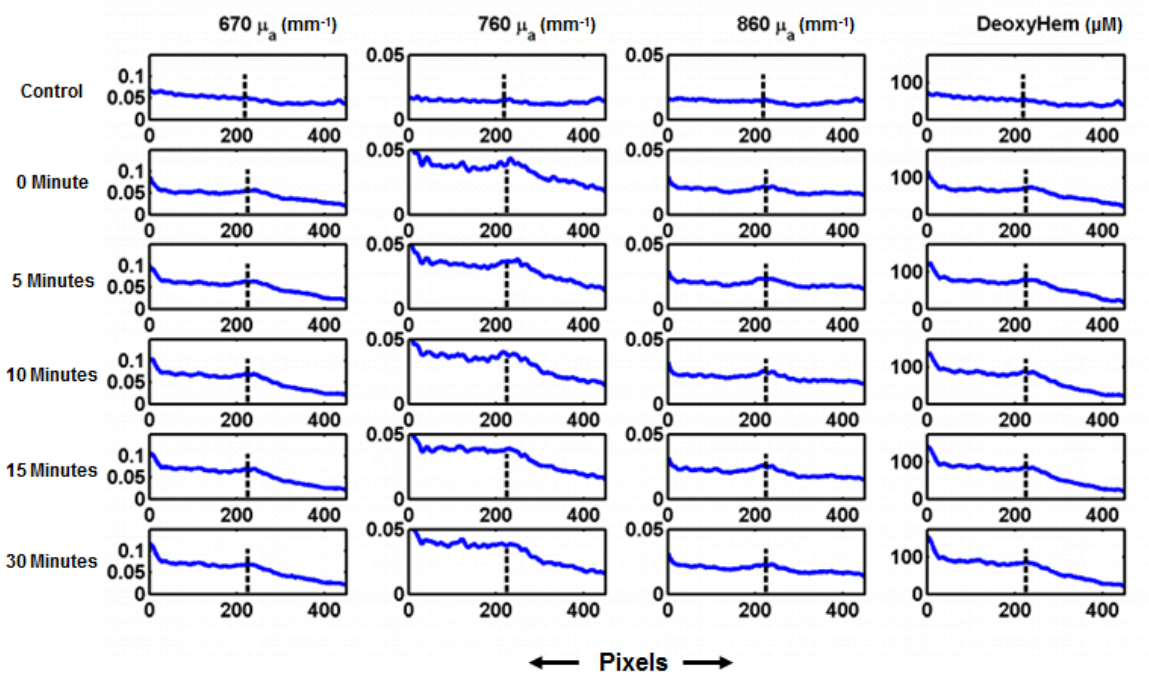

Figure 6.1.3: Line profiles from Rat 3 for various tissue optical parameters. All horizontal axes represent pixel location across the skin flap. The black dotted line represents the necrosis boundary line determined by three plastic surgeons.

6.1.4 Discussion and Conclusion

The utility of this measurement is in its potential for early intervention to treat ischemic tissue. Surprisingly, directly after surgery at the 0 time point, there are noticeable differences in the slope and magnitude of necrotic and viable tissue areas for 670 and 760 absorption and deoxyhemoglobin (see Fig. 6.1.3). To be clear, directly after the flap is elevated it is sutured back in place, which takes approximately 3 to 5 minutes, so the 0 time point represents tissue that has possibly been losing perfusion for several minutes.

For all parameters in Fig. 6.1.3, the trends started at time 0 are kept through the 30-minute time point. This is also surprising, as the outstanding visual appearance of

necrosis seen in the 72-hour image take days to form, but this data and the paper presented in the previous section show sensitivity to early perfusion loss. 670 and 760 nm absorption contribute the most to the deoxyhemoglobin chromophore fit, so the trends, similar in the absorption parameter, are found directly in the chromophore. As expected, the necrotic region is becoming deoxygenated, though interestingly the entire region beyond the eventual necrotic boundary has the same level of deoxyhemoglobin. The point of transition from this deoxyhemoglobin plateau to a monotonic region of decrease seems to correspond with the necrotic boundary very well.

The chromophore most sensitive to 860 nm absorption is oxyhemoglobin. However, one would expect the concentration of oxyhemoglobin to fall dramatically in the necrotic region and Fig. 6.1.3 does not show this trend. The ischemia has not set in long enough to introduce other chromophores like high levels of methemoglobin, and so the chromophore fitting should still be most sensitive to oxy- and deoxyhemoglobin, along with water and lipids. Though this method shows very promising results for possible tissue viability assessment based on deoxyhemoglobin alone, the next section of this chapter will demonstrate the importance of having both oxy- and deoxyhemoglobin to help differentiate venous from arterial occlusions.

6.2 Intraoperative Hemifacial Composite Flap Perfusion Assessment using Spatial Frequency Domain Imaging: A Pilot Study in Preparation for Facial Transplantation

The work in part 6.2 was published in the Annals of Plastic Surgery[174] with the following contributing authors:

Vargas, C.R. MD,[1] Nguyen, J.T. MD,[1] Ashitate, Y. MD,[2,3] Angelo, J. BS,[2,4] Venugopal, V. PhD,[2] Kettenring, F. BS,[2] Neacsu, F. MSc,[2] Frangioni, J.V. MD, PhD,[2,5,6] Gioux, S. PhD,[2] Lee, B.T. MD, MBA, MPH[1]

[1] Division of Plastic and Reconstructive Surgery, Department of Surgery, [2] Division of Hematology and Oncology, Department of Medicine, and [5] Department of Radiology, Beth Israel Deaconess Medical Center, Harvard Medical School, Boston, MA

[3] Division of Cancer Diagnostics and Therapeutics, Hokkaido University Graduate School of Medicine, Sapporo, Japan

[4] Department of Biomedical Engineering, Boston University, Boston, MA

[5] Department of Radiology, Beth Israel Deaconess Medical Center, Harvard Medical School, Boston, MA

[6] Curadel, LLC, Worcester, MA.

6.2.1 Introduction

Vascularized composite allotransplantation (VCA) has continued to increase in popularity over the last 2 decades as a means of providing functional restoration of complex defects.[70] The VCA methods are uniquely advantageous compared with conventional techniques in that they offer replacement of defective or absent structures with anatomically identical tissues.[129] Advancing microsurgical and immunosuppressive techniques have led to composite hand and face transplantation with encouraging

results.[147,149] Since the first reported partial face transplantation in 2005, over 30 human facial VCAs have been performed worldwide.[42,83,148]

Despite distinct clinical utility, more complex VCAs present inherent risks, both perioperatively and over the long term. The risk of flap failure in head and neck free autologous tissue transfer has been reported at 3.8% and represents significant clinical morbidity.[187] Emergent surgical re-exploration is indicated for postoperative flap compromise and is most often performed for venous or arterial insufficiency.[187,181] A majority of salvage procedures performed for vascular compromise in a recent series of autologous head and neck flaps were reported to be successful in preventing complete flap loss.[187] Earlier identification of flap compromise and prompt re-exploration have led to improvement in rates of successful flap salvage.[43] The importance of early detection and salvage of facial allografts cannot be understated, as loss of the graft mandates removal, and may leave patients in a worse functional and aesthetic state than before transplantation.[129]

Although the field of reconstructive microsurgery has seen remarkable advances in VCA, standard intraoperative monitoring techniques have not evolved. In most institutions, flap viability is determined clinically by the surgical team, typically in terms of color, temperature, edema, and capillary refill. Unfortunately, these measures are subjective and rely on relatively late signs of tissue compromise. Often, clinical assessment is supplemented with the use of a handheld Doppler probe when pedicle vessels are easily

accessible. Although other techniques, such as implantable Doppler systems,[68,100] laser Doppler flowmetry,[68] fluorescence angiography,[94,95,103] and near-infrared (NIR) tissue oximetry[98,100] have been described, each has important limitations, and none has achieved widespread adoption into routine clinical practice.

Spatial frequency domain imaging (SFDI) is a noncontact optical imaging method which provides accurate assessment of tissue optical properties using rapid acquisition over a large field of view (>100 cm2).[35,177] Measurement of specific NIR wavelengths allows quantification of tissue constituents—oxyhemoglobin, deoxyhemoglobin, lipids, and water—at depths up to 5 mm.[63] Our group has previously validated the SFDI system in porcine abdominal skin flap, bowel, and liver ischemia models, and performed a first-in-human study during perforator flap breast reconstruction.[120] Here, we present a novel evaluation of this technology in a porcine hemifacial composite transplantation model.

6.2.2 Methods

6.2.2.1 Animals

The use of animals in this study was performed under the supervision of the Institutional Animal Care and Use Committee, and in accordance with approved institutional protocol number 046-2010. Three female, 35 kg Yorkshire pigs (E.M. Parsons and Sons, Hadley, MA) were included in this study. All animals were healthy, with no history of allosensitization. Each pig was housed in its own cage and provided with a standard diet

and water ad libitum. An initial physical examination was performed on each animal before beginning the procedure.

6.2.2.2 Surgical Procedure

Anesthesia was induced using 4.4 mg/kg intramuscular Telazol (Fort Dodge Animal Health, Fort Dodge, IA), and maintained with 2% isoflurane (Baxter Healthcare Corp., Deerfield, IL) in oxygen after intubation. Mechanical ventilation via Quantiflex ventilator (Matrix Medical, Inc, Orchard Park, NY) was maintained throughout the procedure. Femoral central venous access was established for intravenous hydration, and a urinary catheter was placed for urine output monitoring before the start of surgery. Physiologic parameters—heart rate, blood pressure, temperature, and urine output—were monitored during all experiments.

A total of 6 hemifacial composite flaps were elevated, and included skin, muscle, nerve, ear cartilage, parotid gland, and surrounding soft tissue as previously described.[119] In the lateral position, after hair removal, skin was incised to the depth of the platysma anteriorly, cleido-occipitalis and cleidomastoideus posteriorly, and to the periosteum cranially. The upper and lower eyelids were excluded from the flap. Anteriorly, the platysma was divided, and external jugular vein was carefully preserved as the pedicle vein. The tendon of the sternomastoideus muscle was transected, and the bony paracondylar process was removed to reveal the common carotid artery and its branches. The internal carotid artery and lingual artery were ligated and the external carotid was

preserved as the pedicle artery. The superficial temporal artery, 1 of 2 terminal branches of the external carotid, was preserved to supply the flap; the other branch, the maxillary artery, was identified and ligated. Facial dissection was carried out superficial to the masseter muscle toward the ear, with preservation and inclusion of the parotid gland and ligation of the facial nerve trunk. Posteriorly, the flap was elevated in a plane superficial to the trapezius, cleido-occipitalis, and cleidomastoideus muscles. External ear cartilage was detached at the osteocartilaginous junction and included in the flap. After complete elevation about the external jugular vein and external carotid artery pedicle, the flap was secured using a running 4-0 nylon cuticular suture to prevent inadvertent pedicle tension or torsion (Fig. 6.2.1).

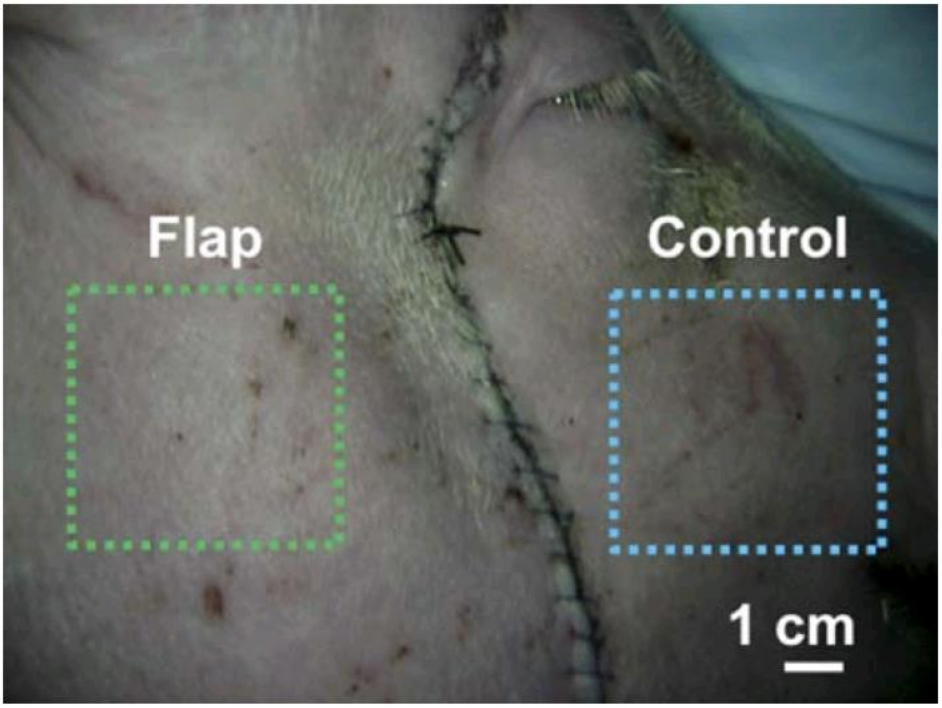

Figure 6.2.1: Hemifacial flap elevation. The SFDI field of view is shown after elevation of a right hemifacial composite flap in a 35-kg Yorkshire pig. The anteriormost aspect of the face is included for control measurement and comparison.

To evaluate the ability to detect tissue oxygenation defects associated with acute compromise of the vascular pedicle, after an initial 3 to 5 minutes of that the data were acquired, a vascular clamp was applied to either the pedicle artery or vein for a period of 10 to 15 minutes and subsequently released.

6.2.2.3 Imaging

As shown in Figure 6.2.2, the SFDI system consists of an imaging cart containing a multispectral NIR light source, control electronics, computer, and adjustable imaging head which enables data acquisition over a 16 × 12 cm field at a 45-cm working distance. The imaging head is further composed of a projector which shines patterns of light onto the surgical field and cameras that record color images coregistered with NIR images for further processing (2 channels, NIR1 from 650 to 780 nm, and NIR2 from 780 to 1000 nm). The SFDI data are acquired by projecting 6 wavelengths onto the field: 670, 730, and 760 collected on the NIR1 channel, and 808, 860, and 980 nm collected on the NIR2 channel. Three distinct patterns are projected: 2 of which are used to extract optical properties, and the other which is used for profilometry measurement and correction for variation in surface profile.[62] Acquisition is performed in real-time intraoperatively, then processed to extract spatial maps of tissue oxyhemoglobin (ctO2Hb) and deoxyhemoglobin (ctHHb) concentration. Complete details of the SFDI clinical system have been previously reported.[63] The SFDI oxygen saturation measurements have also been validated directly against a clinical, Food and Drug Administration–approved

oxygenation probe in an earlier study using a skin flap model, and values were found to correlate within 10%.[63]

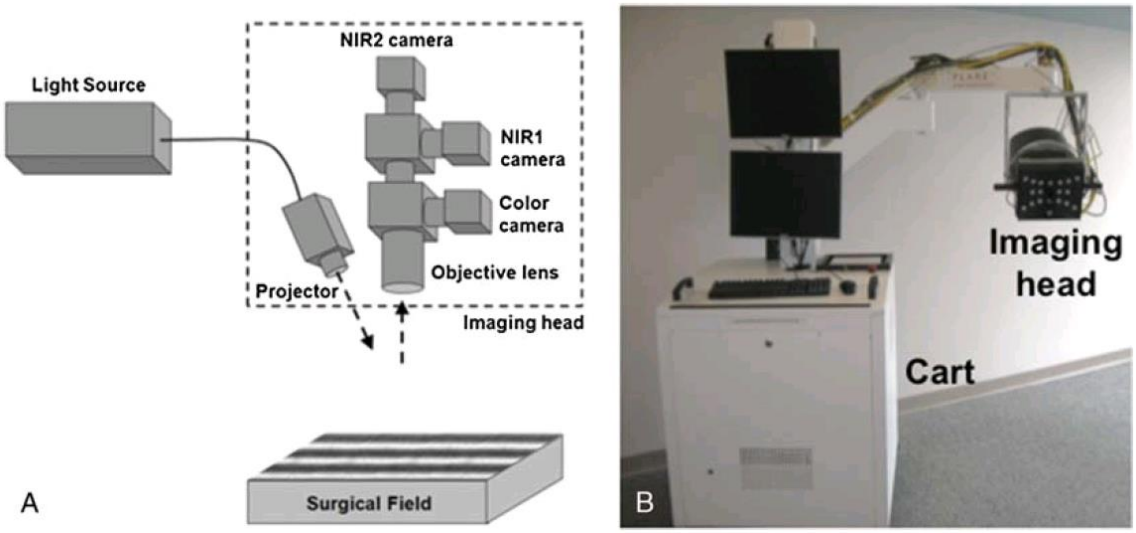

Figure 6.2.2: The SFDI imaging system. The SFDI imaging system is composed of a cart containing all electronics and a light source, and of an imaging head containing a projector and 3 coregistered cameras (color, NIR1 and NIR2). A) Schematics of the imaging head. B) Picture of the actual imaging system.

In this study, SFDI data were acquired continuously during vascular pedicle clamping, and for 10 minutes after clamp release. Regions of interest were established in 2 areas of the facial composite flap as well as in a control area of the face not included in the flap. Data were processed using a custom code in MATLAB (Mathworks, Natick, MA), and component analysis of oxyhemoglobin concentration, deoxyhemoglobin concentration, and total hemoglobin was performed.

6.2.2.4 Statistical Analysis

Change in flap oxygenation measurements were compared with controls using unpaired t tests. A P value less than 0.05 was considered statistically significant. Flaps that experienced significant change in control tissue measurements during the imaging period were not included.

6.2.3 Results

A total of 6 composite hemifacial flaps were successfully elevated and evaluated using SFDI. Intraoperative SFDI demonstrated clear change in all 3 parameters during both arterial and venous pedicle clamping. Unique and consistent profiles using these elements were identified for arterial occlusion and venous occlusion relative to controls and to one another.

6.2.3.1 Arterial Occlusions

As expected clinically, the concentration of oxyhemoglobin after arterial pedicle occlusion decreased within seconds by a mean of 20.0 μM (SD, 5.5). The concentration subsequently appeared to reach a steady trough, which lasted until clamp release. Interestingly, the postocclusion concentration of oxyhemoglobin exceeded baseline flap measurements by an average of 3.1 μM (SD, 2.0) (Fig. 6.2.3A).

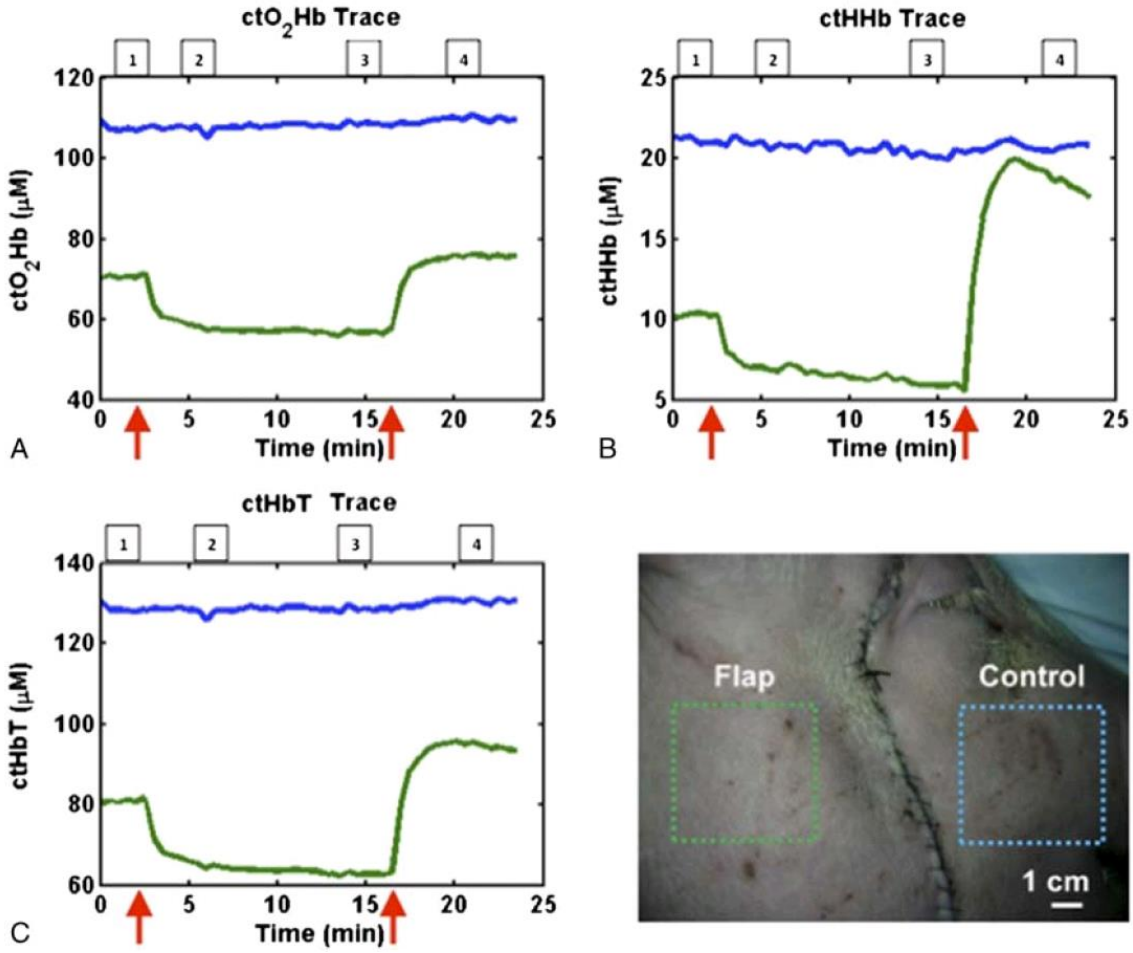

Figure 6.2.3: Arterial occlusion. Representative SFDI measurements of oxygenation parameters are shown over the study period for flap (green) and control (blue) regions. The pedicle artery was clamped at 3 minutes and released at 16min (red arrows). Numbers 1 to 4 indicate key time points for which spatial maps are shown in Figure 6.2.4. A) Tracing of ctO2Hb concentration over the study period. B) Tracing of ctHHb concentration over the study period. C) Tracing of ctHbT during the study period.

Deoxyhemoglobin concentration within the flap also decreased within seconds after arterial pedicle occlusion, and steadily declined by a mean of 4.6 μM (SD, 2.9) during the clamping period. After clamp release, ctHHb increased rapidly, peaking an average of 2.8 μM (SD, 2.1) above the baseline flap measurement before declining again (Fig. 6.2.3B).

Total hemoglobin concentration decreased by an average of 23.0 μM (SD, 4.0) during arterial pedicle clamping, quickly reaching a relatively steady value. Release of the vascular clamp produced an immediate increase in total hemoglobin, which exceeded initial flap measurements by 5.0 μM (SD, 4.6) (Fig. 6.2.3C).

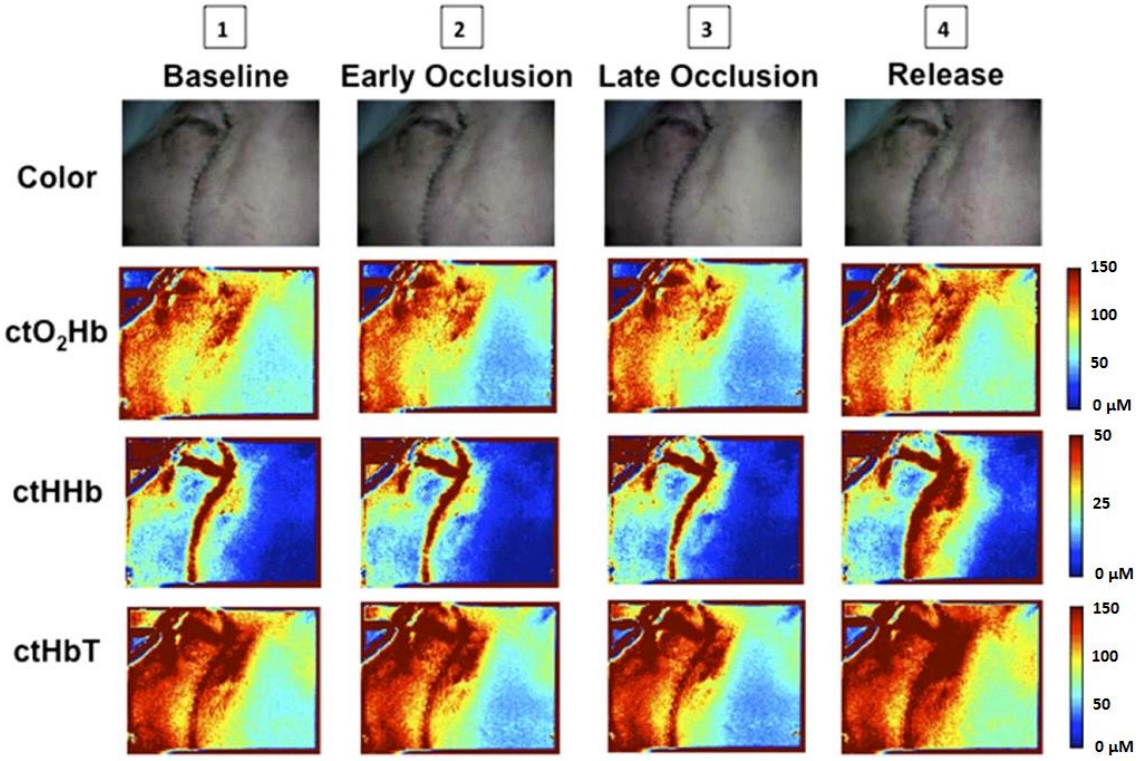

Figure 6.2.4: Spatial map of perfusion defects during arterial occlusion. Changes in flap color, ctO2Hb, ctHHb, and ctHbT over the SFDI field of view are shown at key time points (1–4) during arterial pedicle occlusion. The anterior aspect of the face is included as a control region for comparison.

Spatial mapping of alterations in ctO2Hb, ctHHb, and total hemoglobin (ctHbT) during arterial occlusion are shown in Figure 6.2.4. Although the flap color may appear slightly pale to the surgeon in late occlusion (color images), examination of the SFDI component

maps demonstrate visible change at the earlier time point. All 3 components return to or exceed baseline measurements after release of the pedicle clamp.

6.2.3.2 Venous Occlusions

Unlike the arterial occlusion pattern, venous pedicle clamping produced an immediate increase in oxyhemoglobin concentration by a mean of 13.0 μM (SD, 3.3). The concentration was noted to fall slowly during the clamping period until reaching approximately the initial flap value. Only a very small increase in concentration was noted when the venous clamp was released (Fig. 6.2.5A).

Deoxyhemoglobin measurements followed a dramatic and consistent path during venous occlusion, with a progressive increase by an average of 39.0 μM (SD, 14.0) over the period leading up to clamp release. Release of the venous clamp resulted in a sharp decrease in concentration followed by a gradual return to initial values. Unlike the changes in ctHHb with arterial occlusion, flap ctHHb during venous occlusion actually increased to values well above that of the control tissue (Fig. 6.2.5B).

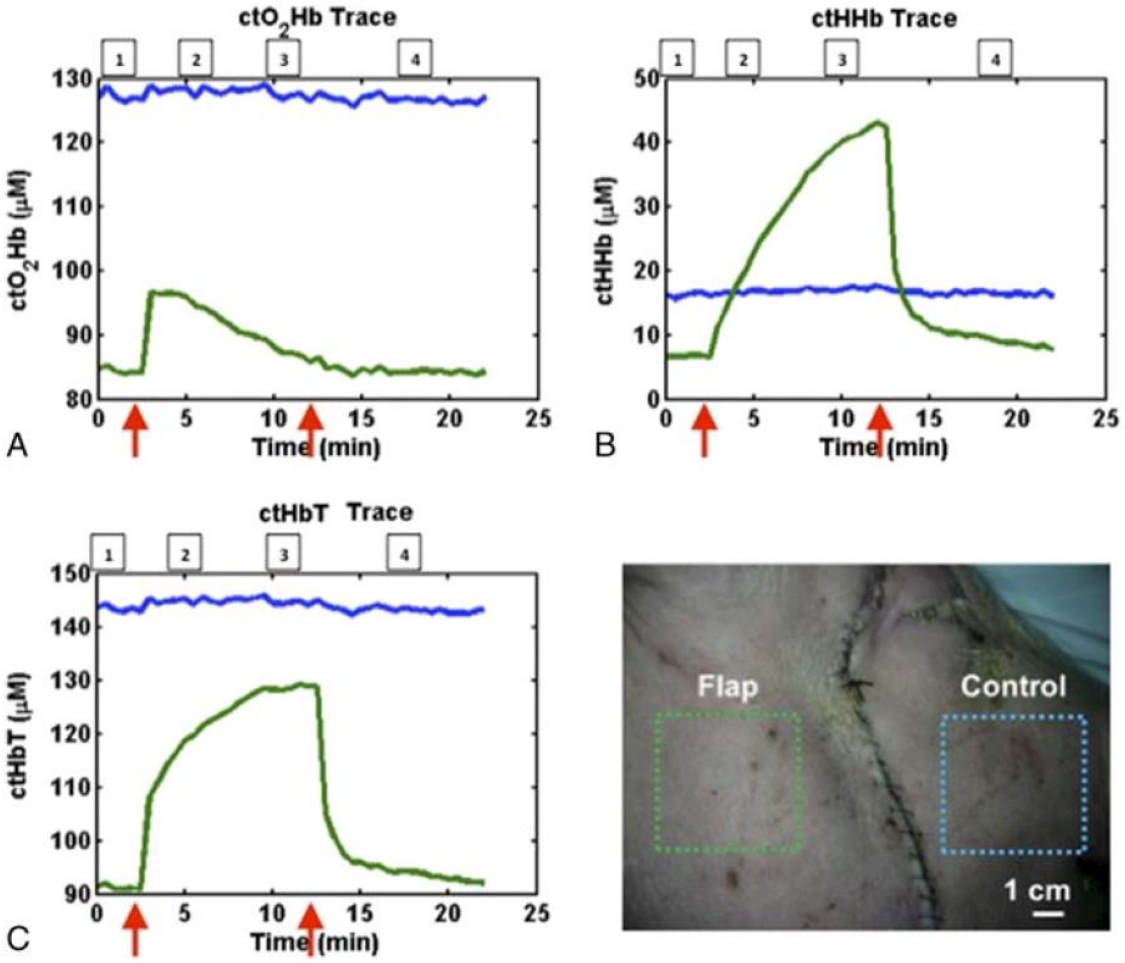

Figure 6.2.5: Venous occlusion. Representative SFDI measurements of oxygenation parameters are shown over the study period for flap (green) and control (blue) regions. The pedicle vein was clamped at 3 minutes and released at 13minutes (red arrows). Numbers 1 to 4 indicate key time points for which spatial maps are shown in Figure 6.2.6 A) Tracing of ctO2Hb concentration over the study period. B) Tracing of ctHHb concentration over the study period. C) Tracing of ctHbT during the study period.

Initial ctHbT measurements in the flap were 105.0 μM (SD, 14.3). Total hemoglobin concentration during pedicle vein occlusion was noted to increase quickly at first then more slowly, reaching an average of 134.0 μM (SD, 18.4). Clamp release produced a steep decrease in ctHbT, which subsequently approached initial flap values at 106.0 μM

(SD, 16.3) (Fig. 6.2.5C). This pattern was noted to correlate inversely with changes during arterial occlusion (Fig. 6.2.3C).

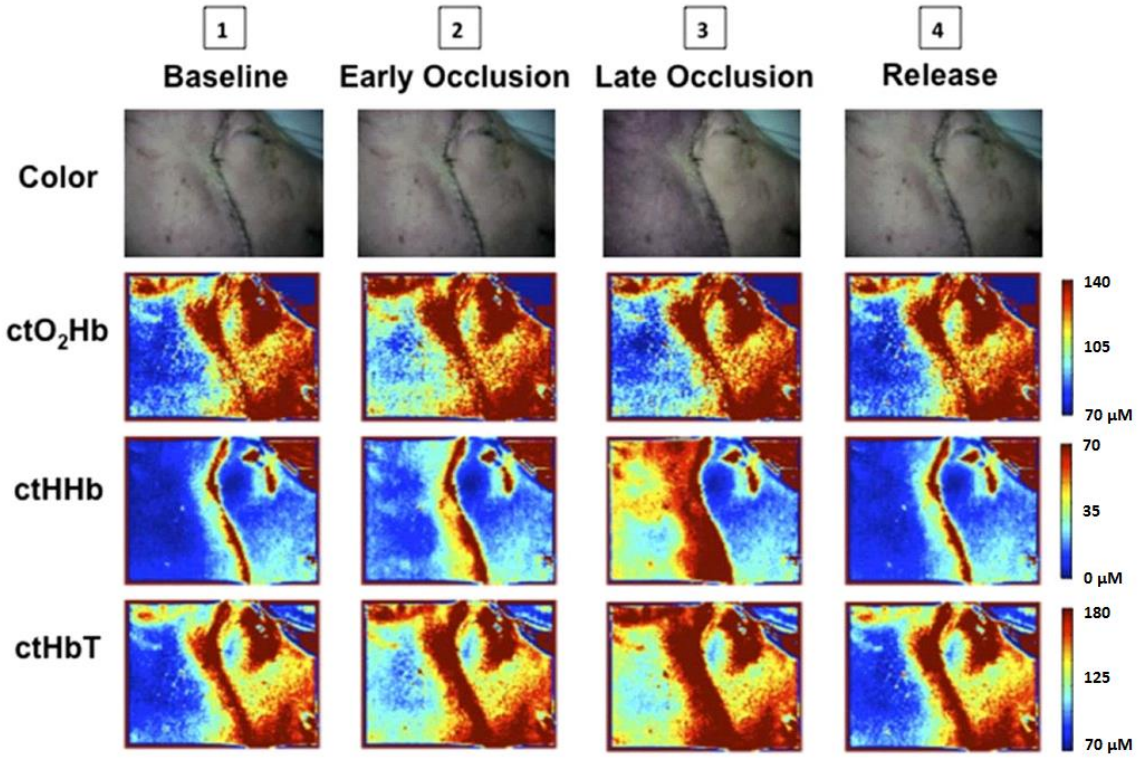

Figure 6.2.6: Spatial map of perfusion defects during venous occlusion. Changes in flap color, ctO2Hb, ctHHb, and ctHbT over the SFDI field of view are shown at key time points (1–4) during venous pedicle occlusion. The anterior aspect of the face is included as a control region for comparison.

Spatial mapping of alterations in ctO2Hb, ctHHb, and ctHbT during venous occlusion are shown in Figure 6.2.6. Although changes in flap color would be apparent to the surgeon in late occlusion (color images), examination of the SFDI component maps demonstrate visible change at the earlier time point. Return to baseline appearance is seen in all 4 components after release of the pedicle clamp.

6.2.4 Discussion

The SFDI technology provides a potential method for reliably imaging changes in ctO2Hb, ctHHb, and ctHbT during VCA in this model of hemifacial flap vascular compromise. Characteristic patterns identified using these measurements were seen quickly after vascular clamping and may be reliably differentiated based on which pedicle vessel was clamped. This technique could provide a means of not only rapidly detecting pedicle occlusion but also directing revascularization of the affected vessel.

The opportunity to view spatial representations of changes in tissue oxygenation associated with pedicle compromise provides additional valuable information to the surgeon. As regions of the flap further from the pedicle vessels are typically affected more rapidly by vascular insufficiency, evaluation of the larger surgical field is important for early detection. Figure 6.2.6 demonstrates the pattern of alteration in each aspect of tissue oxygenation during key phases of experimental venous pedicle occlusion. Appreciable change in ctO2Hb, ctHHb, and ctHbT occur quickly during early occlusion—perhaps sooner than might be detected using more localized techniques or with tissue oximetry measurements alone.

As demonstrated in the ctO2Hb, ctHHb, and ctHbT tracings during pedicle vessel clamping (Figs. 6.2.3 and 6.2.5), the ability to extract these values individually provides valuable insight into the presence and type of vascular compromise beyond simply monitoring tissue oxygenation. Access to this information intraoperatively could aid

surgeons during initial microsurgical anastomosis and flap inset as well as during revision, if necessary. As shown in Table 6.2.1, significant change in ctO2Hb, ctHHB, and ctHbT was seen in both arterial and venous flap pedicle occlusion relative to control tissue. By analyzing ctO2Hb, ctHHb, and ctHbT individually, the SFDI system has the ability to differentiate between arterial and vascular compromise within 2 minutes; far earlier than any potential irreversible damage from thrombosis.

Table 6.2.1: Component Change with Vascular Occlusion

	ΔctO_2Hb, μM	**ΔctHHb, μM**	**ΔctHbT, μM**
(A) Arterial Occlusion			
Flap	20.0 (SD, 5.5)	4.6 (SD, 2.9)	23.0
Control	0.3 (SD, 0.5)	0.7 (SD, 0.8)	0.0 (SD, 0.0)
P	<0.01*	<0.01*	<0.01*
(B) Venous Occlusion			
Flap	13.0 (SD, 3.3)	27.0 (SD, 13.0)	29.0 (SD, 10.0)
Control	12.0 (SD, 1.9)	0.2 (SD, 0.4)	1.0 (SD, 1.1)
P	<0.01*	<0.01*	<0.01*

(A) Absolute change in ctO_2Hb, ctHHb, and ctHbT in control tissue and the hemifacial flap during pedicle artery occlusion are shown (mean, standard deviation). *P* values less than 0.05 are considered statistically significant

(B) Change in ctO_2Hb, ctHHb, and ctHbT in control tissue and hemifacial flap during pedicle vein occlusion are shown (mean, standard deviation). *P* values less than 0.05 are considered statistically significant.

There are limitations to this study. To compare SFDI flap monitoring against the gold standard of clinical assessment as well as methods of tissue oximetry currently in use at some institutions, we will need to perform simultaneous measurements of flap oxygenation parameters using all three techniques. Future study is planned in this regard to assess the time to detection of vessel occlusion using each method. Only complete vascular compromise was evaluated; additional investigation of partial pedicle

compromise is planned to assess the use of SFDI in varying degrees of flap failure. Effects of microvascular anastomosis were not evaluated because native pedicle vessels were clamped after flap elevation. The experimental clamp time of 15 minutes, though important for early detection of pedicle compromise, would not detect patterns of change in oxygenation parameters that require longer ischemia time. In these preliminary experiments, we did not attempt to predict long-term flap outcome in the setting of specific vascular insults. Our group is planning additional study of more complex auto- and allografted composite tissue using SFDI. We are also pursuing development of software capable of providing real-time processing of the SFDI data to further increase the opportunity for intraoperative application (see Chapter 5).

The need for noninvasive, reliable, immediate assessment of composite tissue graft viability is clear, given the morbidity associated with flap failure. The ability to rapidly detect and simultaneously characterize vascular pedicle defects represents an important advancement in the evaluation of composite tissue transfer. The SFDI technology shows promise in providing reconstructive surgeons with critical intraoperative guidance with regard to pedicle vessel integrity.

6.2.5 Conflicts of Interest and Funding

Conflicts of interest and sources of funding: Dr. Frangioni is currently CEO of Curadel, LLC, which has licensed FLARE imaging systems and contrast agents from the Beth Israel Deaconess Medical Center. NIH/NIDCR Award Number R01-DE-022820 (JVF

and BTL); NIH/NIDDK Award Number K01-DK-093603 (SG); NSF Award Number DGE-1247312 (JA).

CHAPTER 7: CONCLUSIONS AND FUTURE WORK

This final chapter summarizes the conclusions of this body of work and offers ideas directly related to these results for future work.

Section 7.1 Summaries

Chapter 3 presents novel technological improvements to fluorescence imaging. The first method, masked detection of structured illumination (MDSI), scans a line of light across a fluorescent sample and uses various masks on the collection pathway to selectively enhance contrast for either superficial or deep fluorescent sources. This is done completely through instrumentation, as the choice of detection mask acts as a filter for short or long source-detector separations, effectively favoring photons that have scattered minimally or that have scattered broadly.

The second method presented in Chapter 3 gives a quantitative fluorescence correction method using single snapshot of optical properties called qF-SSOP. This method uses simultaneous real-time acquisition of fluorescence and optical property maps at the excitation and emission wavelengths in order to correct the fluorescence signal and provide fluorescence concentration. This method is shown to have highly accurate results for a large range of optical properties and outperforms raw fluorescence imaging and F/R imaging (a common correction method) as well. Furthermore, we have demonstrated the

real-time capabilities of this measurement, as each measurement time depends upon a single exposure.

Chapter 4 presents robust improvements to real-time imaging of optical properties with two new techniques. The first builds upon the original single snapshot of optical properties (SSOP) imaging by introducing two-dimensional image processing, height map generation, and profile-corrections to SSOP's real-time acquisition capabilities. This technique has been validated against standard spatial frequency domain imaging (SFDI) measurements, including height map generation, and demonstrated its acquisition speed by presenting a moving hand at approximately 10 frames per second. This profile-corrected technique gives SSOP the robustness necessary for practical imaging in the clinic.

Next, the second technique presented in Chapter 4 was the endoscopic implementation of SSOP. This technique, for the first time, enables simultaneous acquisition of profile-corrected optical property maps, a sample profile map, and hemodynamic maps such as oxyhemoglobin, deoxyhemoglobin, total hemoglobin, and oxygen saturation. Several new challenges were circumvented in order to implement the endoscopic, dual-wavelength imaging scheme, including the spatial-frequency dependence on sample distance. This work validated the accuracy of this bench-top, dual-wavelength endoscopic SSOP system by measuring samples with known optical properties over several distances from the distal end of the endoscope using both wavelengths and ensuring no crosstalk

was present. Several videos were acquired using single- and dual-wavelength imaging as fast as 11 frames per second and vascular occlusions were tracked using oxygenation imaging, resulting in the predictable curve of baseline saturation, loss of perfusion, and quick recovery to normal. This adaptation of SSOP opens the door to many applications once thought to be cut-off from oxygenation imaging, and future work will push it there.

Chapter 5 focuses the other side of this equation for real-time imaging: processing speed. Using new ways of forming and utilizing lookup table (LUT) methods, this work demonstrates that it can be as accurate as the standard LUT method[35] while being 100 times faster. This improvement brings processing speed from seconds to milliseconds and removes the processing bottleneck that prevented any chance at real-time processing. These new methods were demonstrated on a wide range of optical property phantoms as well as in vivo. They also aim to viable in different environments, with one more suited for batch processing on a personal computer and the other for possible on-chip processing. These new methods provide the means for real-time feedback and looks to future work for that implementation.

Finally, Chapter 6 provides demonstrations of widefield optical imaging technologies assessing tissue viability. The first pare uses a rat skin flap model of necrosis in order to have a sample with both necrotic and viable tissue that can be separated by a boundary. Three plastic surgeons chose a necrosis boundary that was used as a gold standard for both the fluorescence imaging and SFDI study. The SFDI study only presents preliminary

data for a single rat, but shows promising correlations between the necrosis boundary and deoxy-hemoglobin variation.

The final project in Chapter 6 presents a pig facial flap model to study how sensitive SFDI is to vascular occlusions, both venous and arterial. The work demonstrates a skin flap model that is viable and amenable to both arterial and vascular occlusions. As expected, oxyhemoglobin concentrations decrease rapidly for arterial occlusions, while deoxyhemoglobin greatly increases for venous occlusions, showing that these measurements are indeed immediately sensitive to occlusions and can show quantitative measures of change far before subjective measures currently practiced such as capillary refill or skin color. However, this work also demonstrates that measurements of tissue oxygen saturation, while capable of sensing either occlusion, cannot discern between an arterial and a venous occlusion. This emphasizes the need for a suite a measurements besides oxygenation alone.

Section 7.2 Future Work

Many future directions are possible based off this dissertation, though a few potential directions stand out to extend the presented work:

1. Masked detection of structured illumination resulted in enhanced fluorescence images, though this work was less quantitative and less impressive than initially hoped for. However, there is potential for this method with endogenous imaging. Work has been done by Mourant and Bigio et al that shows a region of source-

detector separations that does not depend on scattering properties.[111] This means masked detection could be designed to utilize this regime and be sensitive only to changes in absorption presumably due to physiological changes.

2. Many exciting avenues are available to SSOP since its only requirement is that a striped pattern is projected and collected. Some work can aim to improve its application and robustness, as done here with profile measurements and endoscopic implementation, but one can also aim for multimodal developments, such as the presented qF-SSOP or another new technique, cSFDI.[59] For robustness, the ability to acquire many spatial frequencies at once could potentially be very useful and has been demonstrated recently,[116] but not using SSOP. The analysis and filtering in Fourier space is straight forward and new information could be useful, especially for depth resolved measurements. For a multimodal contribution, hyperspectral SSOP seems like a natural extension of combining the quantitative power of the spatial frequency domain along with the robust content of hyperspectral imaging. The most present challenge would be to detect and separate all of this information, but snapshot hyperspectral imaging is also on the rise,[67,72] and the timing seems quite perfect.

3. The rapid lookup table methods presented here have several avenues for improvement, namely improving the fitting functions for the analytic method, choosing a nonlinear (but parametric) sampling function for the “linear” lookup

table, and pre-computing a table for other results besides optical properties. Optical properties are most often used for spectroscopic analysis of the absorption coefficients, and so creating a table that solves directly for oxy- and deoxyhemoglobin would make this table immediately applicable. Furthermore, these tables can be adapted to incorporate more dimensions, or inputs, for more complex output, such as profile-corrected optical properties or multi-frequency analysis.

4. Finally, perhaps the least exciting for engineers but the most necessary, much legwork is needed to bring real clinical impact with most optical technologies that sense functional change. Diffuse optics has continued to make quantitative measures of biomarkers for the last twenty-odd years, yet has little use in the clinic today. More work is needed to demonstrate, with specific application, the utility and physiological relevance of most optical measurements. A few researchers have taken a statistical approach and showed utility of their measurement for guiding surgeons by demonstrating their technique can very accurately discern, for example, between thyroid and parathyroid glands[109] or between neoplastic and non-neoplastic polyps.[137] This I find very promising, as demonstrating high sensitivity, specificity, and reproducibility for a specific problem is providing an answer to that problem. Utilizing this paradigm, perhaps oxygenation measurements of a specific tissue during a specific surgery can be tracked for predictive outcome. Hopeful future applications for endoscopic SSOP

are aimed at imaging various bowel diseases and occlusions, and the use of this tightly focused approach could bring great impact to patient care and management.

Section 7.3 Conclusion

This body of work has aimed to improve, expand, and mature the field of biomedical optics so as to be practical for clinical use and benefit patient outcomes. Surgical guidance is currently lead by subjective measures and needs to be replaced with quantitative tools to provide objective guidance. The proposed techniques have been validated for accuracy and have provided potential answers to what these objective tools might look like. More work needs to be done in order to see these tools reach the clinic, including system optimization and clinical studies to investigate their utility for specific clinical problems. Biomedical optics has great potential to lower healthcare costs, aid patient management, and improve patient outcomes, and it is my hope that this body of work contributes to this goal.

BIBLIOGRAPHY

List of abbreviated journal titles

Acad Radiol	Academic Radiology
Anal Biochem	Analytical Biochemistry
Ann Plast Surg	Annals of Plastic Surgery
Ann Surg	Annals of Surgery
Ann Surg Oncol	Annals of Surgical Oncology
Annu Rev Med	Annual Review of Medicine
Appl Opt	Applied Optics
Biochim Biophys Acta	Biochimica et Biophysica Acta
Biomed Opt Express	Biomedical Optics Express
Biophys J	Biophysical Journal
Br J Plast Surg	British Journal of Plastic Surgery
Breast Cancer Res	Breast Cancer Research
Clin Dermatol	Clinics in Dermatology
Clin Plast Surg	Clinics in Plastic Surgery
Colorectal Dis	Colorectal Disease
Comput Methods Programs Biomed	Computer Methods and Programs in Biomedicine
Curr Opin Biotechnol	Current Opinion in Biotechnology
Curr Opin Chem Biol	Current Opinion in Chemical Biology
Gastrointest Endosc	Gastrointestinal Endoscopy
IEEE ICCP Proceeding	IEEE Intelligent Computer Communication and Processing Proceeding
Int J Low Extrem Wounds	The International Journal of Lower Extremity Wounds
Int J Surg	International Journal of Surgery
Invest Ophthalmol Vis Sci	Investigative Ophthalmology & Visual Science
J Biomed Opt	Journal of Biomedical Optics
J Burn Care Res	Journal of Burn Care & Research
J Cell Sci	Journal of Cell Science
J Neurosurg	Journal of Neurosurgery
J Opt Soc Am A	Journal of the Optical Society of America. A, Optics and Image Science
J Opt Soc Am A Opt Image Sci Vis	Journal of the Optical Society of America. A, Optics, Image Science, and Vision

J Reconstr Microsurg	Journal of Reconstructive Microsurgery
J Surg Res	Journal of Surgical Research
JACC Cardiovasc Imaging	JACC. Cardiovascular Imaging
Lancet Oncol	The Lancet. Oncology
Lasers Med Sci	Lasers in Medical Science
Lasers Surg Med	Lasers in Surgery and Medicine
Med Phys	Medical Physics
Mol Imaging	Molecular Imaging
Mol Imaging Biol	Molecular Imaging and Biology
Nat Biotechnol	Nature Biotechnology
Nat Med	Nature Medicine
Nat Rev Cancer	Nature Reviews. Cancer
Opt Eng	Optical Engineering
Opt Express	Optics Express
Opt Lasers in Eng	Optics and Lasers in Engineering
Opt Lett	Optics Letters
Photochem Photobiol Sci	Photochemical & Photobiological Sciences
Phys Med Biol	Physics in Medicine and Biology
Phys Rev Lett	Physical Review Letters
Physiol Meas	Physiological Measurement
Plast Reconstr Surg,	Plastic and Reconstructive Surgery
Proc Natl Acad Sci U S A	Proceedings of the National Academy of Sciences of the United States of America
Proc SPIE	Proceedings of SPIE - the International Society for Optical Engineering
Surg Endosc	Surgical Endoscopy
Surg Gynecol Obstet	Surgery, Gynecology & Obstetrics
Technol Cancer Res Treat	Technology in Cancer Research & Treatment
Transpl Int	Transplant International

1. Akers, W., et al., "In vivo resolution of multiexponential decays of multiple near-infrared molecular probes by fluorescence lifetime-gated whole-body time-resolved diffuse optical imaging," *Mol Imaging*, **6**(4), 237-46 (2007).

2. Alerstam, E., T. Svensson and S. Andersson-Engels, "Parallel computing with graphics processing units for high-speed Monte Carlo simulation of photon migration," *J Biomed Opt*, **13**(6), 060504 (2008).

3. Angelo, J., et al., "Ultrafast optical property map generation using lookup tables," *J Biomed Opt*, **21**(11), 110501 (2016).

4. Angelo, J., et al. *Masked detection of structured illumination (MDSI): depth sensitive fluorescence measurement*. in *Optical Tomography and Spectroscopy of Tissue X*. 2013.

5. Angelo, J., et al., "Depth-enhanced fluorescence imaging using masked detection of structured illumination," *J Biomed Opt*, **19**(11), 116008 (2014).

6. Angelo, J.P., M. Van de Giessen and S. Gioux, "Real-time endoscopic optical properties imaging using single snapshot of optical properties (SSOP) imaging," *Proc. SPIE*, **9313** (2015).

7. Angelo, J.P., M. Van de Giessen and S. Gioux, "Real-time endoscopic oxygenation imaging using single snapshot of optical properties (SSOP) imaging," *SPIE Presentation*, (2016).

8. Angelo, J.P., et al., "Ultra-fast optical property map generation using lookup tables," *J Biomed Opt*, **21**(11), 110501 (2016).

9. Arridge, S.R. and W.R. Lionheart, "Nonuniqueness in diffusion-based optical tomography," *Opt Lett*, **23**(11), 882-4 (1998).

10. Ayers, F., et al. *Fabrication and characterization of silicone-based tissue phantoms with tunable optical properties in the visible and near infrared domain*. in *SPIE*. 2008.

11. Azar, F.S. and X. Intes, *Translational multimodality optical imaging*. 2008: Artech House.

12. Backman, V., et al., "Detection of preinvasive cancer cells," *Nature*, **406**(6791), 35-6 (2000).

13. Beauvoit, B., T. Kitai and B. Chance, "Contribution of the mitochondrial compartment to the optical properties of the rat liver: a theoretical and practical approach," *Biophys J*, **67**(6), 2501-10 (1994).

14. Beuthan, J., et al., "The spatial variation of the refractive index in biological cells," *Phys Med Biol*, **41**(3), 369-82 (1996).

15. Bevilacqua, F., et al., "Broadband absorption spectroscopy in turbid media by combined frequency-domain and steady-state methods," *Appl Opt*, **39**(34), 6498-507 (2000).

16. Bevilacqua, F., et al., "In vivo local determination of tissue optical properties: applications to human brain," *Appl Opt*, **38**(22), 4939-50 (1999).

17. Boas, D.A., A.M. Dale and M.A. Franceschini, "Diffuse optical imaging of brain activation: approaches to optimizing image sensitivity, resolution, and accuracy," *Neuroimage*, **23 Suppl 1**, S275-88 (2004).

18. Bodenschatz, N., et al., "Diffuse optical microscopy for quantification of depth-dependent epithelial backscattering in the cervix," *J Biomed Opt*, **21**(6), 66001 (2016).

19. Bonner, R.F., et al., "Model for photon migration in turbid biological media," *J Opt Soc Am A*, **4**(3), 423-32 (1987).

20. Bouma, B.E., et al., "Fourier-domain optical coherence tomography: recent advances toward clinical utility," *Curr Opin Biotechnol*, **20**(1), 111-8 (2009).

21. Bradley, R.S. and M.S. Thorniley, "A review of attenuation correction techniques for tissue fluorescence," *J R Soc Interface*, **3**(6), 1-13 (2006).

22. Briers, J.D., "Laser Doppler and time-varying speckle: a reconciliation," *J Opt Soc Am A*, **13**(2), 345-50 (1996).

23. Briers, J.D., "Laser Doppler, speckle and related techniques for blood perfusion mapping and imaging," *Physiol Meas*, **22**(4), R35-66 (2001).

24. Burmeister, D.M., et al., "Utility of spatial frequency domain imaging (SFDI) and laser speckle imaging (LSI) to non-invasively diagnose burn depth in a porcine model," *Burns*, **41**(6), 1242-52 (2015).

25. Busic, V. and R. Das-Gupta, "Temperature monitoring in free flap surgery," *Br J Plast Surg*, **57**(6), 588 (2004).

26. Calabro, K.W. and I.J. Bigio. *On the validity of assumptions to incorporate absorption in Monte Carlo simulations*. in *Biomedical Optics*. 2012: Optical Society of America.

27. Calabro, K.W. and I.J. Bigio, "Influence of the phase function in generalized diffuse reflectance models: review of current formalisms and novel observations," *J Biomed Opt*, **19**(7), 75005 (2014).

28. Cerussi, A.E., et al., "Sources of absorption and scattering contrast for near-infrared optical mammography," *Acad Radiol*, **8**(3), 211-8 (2001).

29. Chamot, S., et al., "Physical interpretation of the phase function related parameter gamma studied with a fractal distribution of spherical scatterers," *Opt Express*, **18**(23), 23664-75 (2010).

30. Chance, B., et al., "Phase measurement of light absorption and scatter in human tissue," *Review of Scientific Instruments*, **69**(10), 3457-81 (1998).

31. Chen, J., et al., "Time-resolved diffuse optical tomography with patterned-light illumination and detection," *Opt Lett*, **35**(13), 2121-3 (2010).

32. Choe, R., et al., "Diffuse optical tomography of breast cancer during neoadjuvant chemotherapy: a case study with comparison to MRI," *Med Phys*, **32**(4), 1128-39 (2005).

33. Colwell, A.S., et al., "Breast reconstruction following nipple-sparing mastectomy: predictors of complications, reconstruction outcomes, and 5-year trends," *Plast Reconstr Surg*, **133**(3), 496-506 (2014).

34. Corlu, A., et al., "Uniqueness and wavelength optimization in continuous-wave multispectral diffuse optical tomography," *Opt Lett*, **28**(23), 2339-41 (2003).

35. Cuccia, D.J., et al., "Quantitation and mapping of tissue optical properties using modulated imaging," *J Biomed Opt*, **14**(2), 024012 (2009).

36. Cuccia, D.J., et al., "Modulated imaging: quantitative analysis and tomography of turbid media in the spatial-frequency domain," *Opt Lett*, **30**(11), 1354-6 (2005).

37. Cui, W., N. Wang and B. Chance, "Study of photon migration depths with time-resolved spectroscopy," *Opt Lett*, **16**(21), 1632-4 (1991).

38. D'Andrea, C., et al., "Fast 3D optical reconstruction in turbid media using spatially modulated light," *Biomed Opt Express*, **1**(2), 471-81 (2010).

39. Darafsheh, A., et al., "Performance characterization of a low-cost spatial frequency domain imaging system for the determination of optical properties in tissue-simulating phantoms and in vivo," *Photodiagnosis and Photodynamic Therapy*, **12**(3), 331-2 (2015).

40. de Veld, D.C., et al., "Autofluorescence and diffuse reflectance spectroscopy for oral oncology," *Lasers Surg Med*, **36**(5), 356-64 (2005).

41. Delpy, D.T., et al., "Estimation of optical pathlength through tissue from direct time of flight measurement," *Phys Med Biol*, **33**(12), 1433-42 (1988).

42. Devauchelle, B., et al., "First human face allograft: early report," *Lancet*, **368**(9531), 203-9 (2006).

43. Disa, J.J., P.G. Cordeiro and D.A. Hidalgo, "Efficacy of conventional monitoring techniques in free tissue transfer: an 11-year experience in 750 consecutive cases," *Plast Reconstr Surg*, **104**(1), 97-101 (1999).

44. Dögnitz, N. and G. Wagnières, "Determination of tissue optical properties by steady-state spatial frequency-domain reflectometry," *Lasers in Medical Science*, **13**(1), 55-65 (1998).

45. Doornbos, R.M., et al., "The determination of in vivo human tissue optical properties and absolute chromophore concentrations using spatially resolved steady-state diffuse reflectance spectroscopy," *Phys Med Biol*, **44**(4), 967-81 (1999).

46. Draijer, M., et al., "Review of laser speckle contrast techniques for visualizing tissue perfusion," *Lasers Med Sci*, **24**(4), 639-51 (2009).

47. Durr, N.J., et al., "Imaging colonic surface topography with a photometric stereo endoscope," *In Gastrointestinal Endoscopy*, **79** (2014).

48. Elson, D., et al., "Time-domain fluorescence lifetime imaging applied to biological tissue," *Photochem Photobiol Sci*, **3**(8), 795-801 (2004).

49. Erickson, T.A., et al., "Lookup-table method for imaging optical properties with structured illumination beyond the diffusion theory regime," *J Biomed Opt*, **15**(3), 036013 (2010).

50. Eun, H.C., "Evaluation of skin blood flow by laser Doppler flowmetry," *Clin Dermatol*, **13**(4), 337-47 (1995).

51. Fantoni, F., et al., "Laser line scanning for fluorescence reflectance imaging: a phantom study and in vivo validation of the enhancement of contrast and resolution," *J Biomed Opt*, **19**(10), 106003 (2014).

52. Farrell, T.J., M.S. Patterson and B. Wilson, "A diffusion theory model of spatially resolved, steady-state diffuse reflectance for the noninvasive determination of tissue optical properties in vivo," *Med Phys*, **19**(4), 879-88 (1992).

53. Fengler, J., "Near-infrared fluorescence laparoscopy--technical description of PINPOINT(R) a novel and commercially available system," *Colorectal Dis*, **17**(3), 3-6 (2015).

54. Fishkin, J.B. and E. Gratton, "Propagation of photon-density waves in strongly scattering media containing an absorbing semi-infinite plane bounded by a straight edge," *J Opt Soc Am A*, **10**(1), 127-40 (1993).

55. Frangioni, J.V., "In vivo near-infrared fluorescence imaging," *Curr Opin Chem Biol*, **7**(5), 626-34 (2003).

56. Gabriele, M.L., et al., "Optical coherence tomography: history, current status, and laboratory work," *Invest Ophthalmol Vis Sci*, **52**(5), 2425-36 (2011).

57. Gardner, C.M., S.L. Jacques and A.J. Welch, "Fluorescence spectroscopy of tissue: recovery of intrinsic fluorescence from measured fluorescence," *Appl Opt*, **35**(10), 1780-92 (1996).

58. Garwood, E.R., et al., "Total skin-sparing mastectomy: complications and local recurrence rates in 2 cohorts of patients," *Ann Surg*, **249**(1), 26-32 (2009).

59. Ghijsen, M., et al., "Real-time simultaneous single snapshot of optical properties and blood flow using coherent spatial frequency domain imaging (cSFDI)," *Biomed Opt Express*, **7**(3), 870-82 (2016).

60. Gibson, A.P., J.C. Hebden and S.R. Arridge, "Recent advances in diffuse optical imaging," *Phys Med Biol*, **50**(4), R1-43 (2005).

61. Gioux, S., H.S. Choi and J.V. Frangioni, "Image-guided surgery using invisible near-infrared light: fundamentals of clinical translation," *Mol Imaging*, **9**(5), 237-55 (2010).

62. Gioux, S., et al., "Three-dimensional surface profile intensity correction for spatially modulated imaging," *J Biomed Opt*, **14**(3), 034045 (2009).

63. Gioux, S., et al., "First-in-human pilot study of a spatial frequency domain oxygenation imaging system," *J Biomed Opt*, **16**(8), 086015 (2011).

64. Giunta, R.E., et al., "Prediction of flap necrosis with laser induced indocyanine green fluorescence in a rat model," *Br J Plast Surg*, **58**(5), 695-701 (2005).

65. Grosenick, D., et al., "Development of a time-domain optical mammograph and first in vivo applications," *Appl Opt*, **38**(13), 2927-43 (1999).

66. Gurjar, R.S., et al., "Imaging human epithelial properties with polarized light-scattering spectroscopy," *Nat Med*, **7**(11), 1245-8 (2001).

67. Hagen, N. and M.W. Kudenov, "Review of snapshot spectral imaging technologies," *Opt Eng*, **52**(9) (2013).

68. Hallock, G.G., "Acoustic Doppler sonography, color duplex ultrasound, and laser Doppler flowmetry as tools for successful autologous breast reconstruction," *Clin Plast Surg*, **38**(2), 203-11 (2011).

69. Harrison, D.K., "Optical measurement of tissue oxygen saturation," *Int J Low Extrem Wounds*, **1**(3), 191-201 (2002).

70. Hettiaratchy, S., et al., "Composite tissue allotransplantation--a new era in plastic surgery?," *Br J Plast Surg*, **57**(5), 381-91 (2004).

71. Hillman, E.M., et al., "Laminar optical tomography: demonstration of millimeter-scale depth-resolved imaging in turbid media," *Opt Lett*, **29**(14), 1650-2 (2004).

72. Horstmeyer, R., et al., "Flexible Multimodal Camera Using a Light Field Architecture," *IEEE ICCP Proceeding*, (2009).

73. Hunt, T.K. and J.E. Dunphy, "Effects of increasing oxygen supply to healing wounds," *Br J Surg*, **56**(9), 705 (1969).

74. Hunt, T.K. and M.P. Pai, "The effect of varying ambient oxygen tensions on wound metabolism and collagen synthesis," *Surg Gynecol Obstet*, **135**(4), 561-7 (1972).

75. Indebetouw, G., "Profile measurement using projection of running fringes," *Appl Opt*, **17**(18), 2930-3 (1978).

76. Intes, X., et al., "In vivo continuous-wave optical breast imaging enhanced with Indocyanine Green," *Med Phys*, **30**(6), 1039-47 (2003).

77. Intuitive Surgical, I. *Da Vinci Surgical System*. [cited 2016 August]; Available from: http://www.intuitivesurgical.com.

78. Jacques, S.L., "Optical properties of biological tissues: a review," *Phys Med Biol*, **58**(11), R37-61 (2013).

79. Jacques, S.L. and B.W. Pogue, "Tutorial on diffuse light transport," *J Biomed Opt*, **13**(4), 041302 (2008).

80. Jacques, S.L. and L. Wang, *Monte Carlo modeling of light transport in tissues*, in *Optical-thermal response of laser-irradiated tissue*. 1995, Springer. p. 73-100.

81. Johnson, W.R., et al., "Snapshot hyperspectral imaging in ophthalmology," *J Biomed Opt*, **12**(1), 014036 (2007).

82. Keereweer, S., et al., "Optical image-guided surgery--where do we stand?," *Mol Imaging Biol*, **13**(2), 199-207 (2011).

83. Khalifian, S., et al., "Facial transplantation: the first 9 years," *Lancet*, **384**(9960), 2153-63 (2014).

84. Kienle, A., F.K. Forster and R. Hibst, "Anisotropy of light propagation in biological tissue," *Opt Lett*, **29**(22), 2617-9 (2004).

85. Kienle, A., et al., "Spatially resolved absolute diffuse reflectance measurements for noninvasive determination of the optical scattering and absorption coefficients of biological tissue," *Appl Opt*, **35**(13), 2304-14 (1996).

86. Kim, C., et al., "Sentinel lymph nodes and lymphatic vessels: noninvasive dual-modality in vivo mapping by using indocyanine green in rats--volumetric spectroscopic photoacoustic imaging and planar fluorescence imaging," *Radiology*, **255**(2), 442-50 (2010).

87. Kim, T.H., et al., "Evaluation of temperature-sensitive, indocyanine green-encapsulating micelles for noninvasive near-infrared tumor imaging," *Pharm Res*, **27**(9), 1900-13 (2010).

88. Kingwell, B.A., et al., "Type 2 diabetic individuals have impaired leg blood flow responses to exercise: role of endothelium-dependent vasodilation," *Diabetes Care*, **26**(3), 899-904 (2003).

89. Konecky, S.D., et al., "Quantitative optical tomography of sub-surface heterogeneities using spatially modulated structured light," *Opt Express*, **17**(17), 14780-90 (2009).

90. Konecky, S.D., et al., "Imaging scattering orientation with spatial frequency domain imaging," *J Biomed Opt*, **16**(12), 126001 (2011).

91. Kukreti, S., et al., "Characterization of metabolic differences between benign and malignant tumors: high-spectral-resolution diffuse optical spectroscopy," *Radiology*, **254**(1), 277-84 (2010).

92. Lachance, V., et al., "Ubiquitylation and activation of a Rab GTPase is promoted by a beta(2)AR-HACE1 complex," *J Cell Sci*, **127**(Pt 1), 111-23 (2014).

93. Laughney, A.M., et al., "Spectral discrimination of breast pathologies in situ using spatial frequency domain imaging," *Breast Cancer Res*, **15**(4), R61 (2013).

94. Lee, B.T., et al., "The FLARE intraoperative near-infrared fluorescence imaging system: a first-in-human clinical trial in perforator flap breast reconstruction," *Plast Reconstr Surg*, **126**(5), 1472-81 (2010).

95. Lee, B.T., et al., "Intraoperative near-infrared fluorescence imaging in perforator flap reconstruction: current research and early clinical experience," *J Reconstr Microsurg*, **26**(1), 59-65 (2010).

96. Leitner, R., et al., "Multi-spectral video endoscopy system for the detection of cancerous tissue," *Pattern Recognition Letters*, **34**(1), 85-93 (2013).

97. Leutenegger, M., et al., "Real-time full field laser Doppler imaging," *Biomed Opt Express*, **2**(6), 1470-7 (2011).

98. Lin, S.J., et al., "Tissue oximetry monitoring in microsurgical breast reconstruction decreases flap loss and improves rate of flap salvage," *Plast Reconstr Surg*, **127**(3), 1080-5 (2011).

99. Litvack, Z.N., G. Zada and E.R. Laws, Jr., "Indocyanine green fluorescence endoscopy for visual differentiation of pituitary tumor from surrounding structures," *J Neurosurg*, **116**(5), 935-41 (2012).

100. Lohman, R.F., et al., "A prospective analysis of free flap monitoring techniques: physical examination, external Doppler, implantable Doppler, and tissue oximetry," *J Reconstr Microsurg*, **29**(1), 51-6 (2013).

101. Matcher, S.J. and C.E. Cooper, "Absolute quantification of deoxyhaemoglobin concentration in tissue near infrared spectroscopy," *Phys Med Biol*, **39**(8), 1295-312 (1994).

102. Matcher, S.J., et al., "Performance comparison of several published tissue near-infrared spectroscopy algorithms," *Anal Biochem*, **227**(1), 54-68 (1995).

103. Matsui, A., et al., "Image-guided perforator flap design using invisible near-infrared light and validation with x-ray angiography," *Ann Plast Surg*, **63**(3), 327-30 (2009).

104. Mazhar, A., et al., "Structured illumination enhances resolution and contrast in thick tissue fluorescence imaging," *J Biomed Opt*, **15**(1), 010506 (2010).

105. Mazhar, A., et al., "Laser speckle imaging in the spatial frequency domain," *Biomed Opt Express*, **2**(6), 1553-63 (2011).

106. Mazhar, A., et al., "Wavelength optimization for rapid chromophore mapping using spatial frequency domain imaging," *Journal of Biomedical Optics*, **15**(6), 061716 (2010).

107. McClatchy, D.M., 3rd, et al., "Wide-field quantitative imaging of tissue microstructure using sub-diffuse spatial frequency domain imaging," *Optica*, **3**(6), 613-21 (2016).

108. McFarlane, R.M., G. Deyoung and R.A. Henry, "The Design of a Pedicle Flap in the Rat to Study Necrosis and Its Prevention," *Plast Reconstr Surg*, **35**, 177-82 (1965).

109. McWade, M.A., et al., "A novel optical approach to intraoperative detection of parathyroid glands," *Surgery*, **154**(6), 1371-7; discussion 7 (2013).

110. Mourant, J.R., et al., "Elastic scattering spectroscopy as a diagnostic tool for differentiating pathologies in the gastrointestinal tract: preliminary testing," *J Biomed Opt*, **1**(2), 192-9 (1996).

111. Mourant, J.R., et al., "Measuring absorption coefficients in small volumes of highly scattering media: source-detector separations for which path lengths do not depend on scattering properties," *Appl Opt*, **36**(22), 5655-61 (1997).

112. Mourant, J.R., et al., "Influence of the scattering phase function on light transport measurements in turbid media performed with small source-detector separations," *Opt Lett*, **21**(7), 546-8 (1996).

113. Mourant, J.R., et al., "Mechanisms of light scattering from biological cells relevant to noninvasive optical-tissue diagnostics," *Appl Opt*, **37**(16), 3586-93 (1998).

114. Murray, A.K., A.L. Herrick and T.A. King, "Laser Doppler imaging: a developing technique for application in the rheumatic diseases," *Rheumatology (Oxford)*, **43**(10), 1210-8 (2004).

115. Nadeau, K.P., A.J. Durkin and B.J. Tromberg, "Advanced demodulation technique for the extraction of tissue optical properties and structural orientation contrast in the spatial frequency domain," *J Biomed Opt*, **19**(5), 056013 (2014).

116. Nadeau, K.P., et al., "Multifrequency synthesis and extraction using square wave projection patterns for quantitative tissue imaging," *J Biomed Opt*, **20**(11), 116005 (2015).

117. Neil, M.A., R. Juskaitis and T. Wilson, "Method of obtaining optical sectioning by using structured light in a conventional microscope," *Opt Lett*, **22**(24), 1905-7 (1997).

118. Nguyen, J.Q., et al., "Spatial frequency domain imaging of burn wounds in a preclinical model of graded burn severity," *J Biomed Opt*, **18**(6), 66010 (2013).

119. Nguyen, J.T., et al., "Face transplant perfusion assessment using near-infrared fluorescence imaging," *J Surg Res*, **177**(2), e83-8 (2012).

120. Nguyen, J.T., et al., "A novel pilot study using spatial frequency domain imaging to assess oxygenation of perforator flaps during reconstructive breast surgery," *Ann Plast Surg*, **71**(3), 308-15 (2013).

121. O'Leary, M.A., et al., "Refraction of diffuse photon density waves," *Phys Rev Lett*, **69**(18), 2658-61 (1992).

122. Olson, G.L., L.H. Auer and M.L. Hall, "Diffusion, P 1, and other approximate forms of radiation transport," *Journal of Quantitative Spectroscopy and Radiative Transfer*, **64**(6), 619-34 (2000).

123. Olympus, I. *Endoeye Flex 3D*. [cited 2016 August]; Available from: medical.olympusamerica.com.

124. Palmer, G.M. and N. Ramanujam, "Monte Carlo-based inverse model for calculating tissue optical properties. Part I: Theory and validation on synthetic phantoms," *Appl Opt*, **45**(5), 1062-71 (2006).

125. Perelman, L.T., et al., "Observation of Periodic Fine Structure in Reflectance from Biological Tissue: A New Technique for Measuring Nuclear Size Distribution," *Physical Review Letters*, **80**(3), 627-30 (1998).

126. Pfefer, T.J., et al., "Selective detection of fluorophore layers in turbid media: the role of fiber-optic probe design," *Opt Lett*, **28**(2), 120-2 (2003).

127. Pogue, B., et al., "Comparison of imaging geometries for diffuse optical tomography of tissue," *Opt Express*, **4**(8), 270-86 (1999).

128. Pogue, B.W. and M.S. Patterson, "Review of tissue simulating phantoms for optical spectroscopy, imaging and dosimetry," *J Biomed Opt*, **11**(4), 041102 (2006).

129. Pomahac, B., et al., "Current principles of facial allotransplantation: the Brigham and Women's Hospital Experience," *Plast Reconstr Surg*, **131**(5), 1069-76 (2013).

130. Ponticorvo, A., et al., "Quantitative assessment of graded burn wounds in a porcine model using spatial frequency domain imaging (SFDI) and laser speckle imaging (LSI)," *Biomed Opt Express*, **5**(10), 3467-81 (2014).

131. Popp, A.K., et al., "Microscopic origin of light scattering in tissue," *Appl Opt*, **42**(16), 2871-80 (2003).

132. Rajaram, N., T.H. Nguyen and J.W. Tunnell, "Lookup table-based inverse model for determining optical properties of turbid media," *J Biomed Opt*, **13**(5), 050501 (2008).

133. Ramella-Roman, J.C., S.A. Prahl and S.L. Jacques, "Three Monte Carlo programs of polarized light transport into scattering media: part I," *Optics Express*, **13**(12), 4420-38 (2005).

134. Rath, T., et al., "In vivo real-time assessment of colorectal polyp histology using an optical biopsy forceps system based on laser-induced fluorescence spectroscopy," *Endoscopy*, **48**(6), 557-62 (2016).

135. Rinker, B., et al., "The effect of calcium channel blockers on smoking-induced skin flap necrosis," *Plast Reconstr Surg*, **125**(3), 866-71 (2010).

136. Roblyer, D., et al., "Optical imaging of breast cancer oxyhemoglobin flare correlates with neoadjuvant chemotherapy response one day after starting treatment," *Proc Natl Acad Sci U S A*, **108**(35), 14626-31 (2011).

137. Rodriguez-Diaz, E., et al., "Endoscopic histological assessment of colonic polyps by using elastic scattering spectroscopy," *Gastrointest Endosc*, **81**(3), 539-47 (2015).

138. Rohrbach, D.J., et al., "Preoperative mapping of nonmelanoma skin cancer using spatial frequency domain and ultrasound imaging," *Acad Radiol*, **21**(2), 263-70 (2014).

139. Russell, J.A., et al., "Cutaneous tissue flap viability following partial venous obstruction," *Plast Reconstr Surg*, **117**(7), 2259-66; discussion 67-8 (2006).

140. Saager, R.B., et al., "Quantitative fluorescence imaging of protoporphyrin IX through determination of tissue optical properties in the spatial frequency domain," *J Biomed Opt*, **16**(12), 126013 (2011).

141. Schmidt, F.E., et al., "A 32-channel time-resolved instrument for medical optical tomography," *Review of Scientific Instruments*, **71**(1), 256-65 (2000).

142. Schmitz-Valckenberg, S., et al., "Fundus autofluorescence imaging: review and perspectives," *Retina*, **28**(3), 385-409 (2008).

143. Serruys, P.W., et al., "A Polylactide Bioresorbable Scaffold Eluting Everolimus for Treatment of Coronary Stenosis: 5-Year Follow-Up," *J Am Coll Cardiol*, **67**(7), 766-76 (2016).

144. Sevick-Muraca, E.M., "Translation of near-infrared fluorescence imaging technologies: emerging clinical applications," *Annu Rev Med*, **63**, 217-31 (2012).

145. Sexton, K., et al., "Pulsed-light imaging for fluorescence guided surgery under normal room lighting," *Opt Lett*, **38**(17), 3249-52 (2013).

146. Shah, N., et al., "Noninvasive functional optical spectroscopy of human breast tissue," *Proc Natl Acad Sci U S A*, **98**(8), 4420-5 (2001).

147. Shanmugarajah, K., et al., "Clinical outcomes of facial transplantation: a review," *Int J Surg*, **9**(8), 600-7 (2011).

148. Siemionow, M. and A. Klimczak, "Advances in the development of experimental composite tissue transplantation models," *Transpl Int*, **23**(1), 2-13 (2010).

149. Siemionow, M.Z., et al., "First U.S. near-total human face transplantation: a paradigm shift for massive complex injuries," *Plast Reconstr Surg*, **125**(1), 111-22 (2010).

150. Singh-Moon, R.P., et al., "Spatial mapping of drug delivery to brain tissue using hyperspectral spatial frequency-domain imaging," *J Biomed Opt*, **19**(9), 96003 (2014).

151. Srinivasan, S., et al., "Interpreting hemoglobin and water concentration, oxygen saturation, and scattering measured in vivo by near-infrared breast tomography," *Proc Natl Acad Sci U S A*, **100**(21), 12349-54 (2003).

152. Srinivasan, V., H.C. Liu and M. Halioua, "Automated phase-measuring profilometry of 3-D diffuse objects," *Appl Opt*, **23**(18), 3105 (1984).

153. Stummer, W., et al., "Fluorescence-guided surgery with 5-aminolevulinic acid for resection of malignant glioma: a randomised controlled multicentre phase III trial," *Lancet Oncol*, **7**(5), 392-401 (2006).

154. Subramanian, H., et al., "Optical methodology for detecting histologically unapparent nanoscale consequences of genetic alterations in biological cells," *Proc Natl Acad Sci U S A*, **105**(51), 20118-23 (2008).

155. Suter, M.J., et al., "Intravascular optical imaging technology for investigating the coronary artery," *JACC Cardiovasc Imaging*, **4**(9), 1022-39 (2011).

156. Svaasand, L.O., et al., "Reflectance measurements of layered media with diffuse photon-density waves: a potential tool for evaluating deep burns and subcutaneous lesions," *Phys Med Biol*, **44**(3), 801-13 (1999).

157. Swartling, J., J.S. Dam and S. Andersson-Engels, "Comparison of spatially and temporally resolved diffuse-reflectance measurement systems for determination of biomedical optical properties," *Appl Opt*, **42**(22), 4612-20 (2003).

158. Tabassum, S., et al., "Feasibility of spatial frequency domain imaging (SFDI) for optically characterizing a preclinical oncology model," *Biomed Opt Express*, **7**(10), 4154-70 (2016).

159. Takeda, M. and K. Mutoh, "Fourier transform profilometry for the automatic measurement of 3-D object shapes," *Appl Opt*, **22**(24), 3977 (1983).

160. Troyan, S.L., et al., "The FLARE intraoperative near-infrared fluorescence imaging system: a first-in-human clinical trial in breast cancer sentinel lymph node mapping," *Ann Surg Oncol*, **16**(10), 2943-52 (2009).

161. Tsui, C., R. Klein and M. Garabrant, "Minimally invasive surgery: national trends in adoption and future directions for hospital strategy," *Surg Endosc*, **27**(7), 2253-7 (2013).

162. Vakoc, B.J., et al., "Cancer imaging by optical coherence tomography: preclinical progress and clinical potential," *Nat Rev Cancer*, **12**(5), 363-8 (2012).

163. Valdes, P.A., J. Angelo and S. Gioux. *Real-time quantitative fluorescence imaging using a single snapshot optical properties technique for neurosurgical guidance*. in *SPIE BiOS*. 2015: International Society for Optics and Photonics.

164. Valdes, P.A., et al., "System and methods for wide-field quantitative fluorescence imaging during neurosurgery," *Opt Lett*, **38**(15), 2786-8 (2013).

165. Valdes, P.A., et al., "delta-aminolevulinic acid-induced protoporphyrin IX concentration correlates with histopathologic markers of malignancy in human gliomas: the need for quantitative fluorescence-guided resection to identify regions of increasing malignancy," *Neuro Oncol*, **13**(8), 846-56 (2011).

166. Valdes, P.A., et al., "Combined fluorescence and reflectance spectroscopy for in vivo quantification of cancer biomarkers in low- and high-grade glioma surgery," *J Biomed Opt*, **16**(11), 116007 (2011).

167. Valdes, P.A., et al., "Quantitative, spectrally-resolved intraoperative fluorescence imaging," *Sci Rep*, **2**, 798 (2012).

168. Valdes, P.A., et al., "A spectrally constrained dual-band normalization technique for protoporphyrin IX quantification in fluorescence-guided surgery," *Opt Lett*, **37**(11), 1817-9 (2012).

169. van Dam, G.M., et al., "Intraoperative tumor-specific fluorescence imaging in ovarian cancer by folate receptor-alpha targeting: first in-human results," *Nat Med*, **17**(10), 1315-9 (2011).

170. van de Giessen, M., J.P. Angelo and S. Gioux, "Real-time, profile-corrected single snapshot imaging of optical properties," *Biomed Opt Express*, **6**(10), 4051-62 (2015).

171. Van der Jeught, S. and J.J. Dirckx, "Real-time structured light profilometry: a review," *Opt Lasers in Eng*, (2016).

172. Van der Jeught, S., J.A. Soons and J.J. Dirckx, "Real-time microscopic phase-shifting profilometry," *Appl Opt*, **54**(15), 4953-9 (2015).

173. Vargas, C.R., et al., "Mastectomy skin necrosis after microsurgical breast reconstruction," *J Surg Res*, **198**(2), 530-4 (2015).

174. Vargas, C.R., et al., "Intraoperative Hemifacial Composite Flap Perfusion Assessment Using Spatial Frequency Domain Imaging: A Pilot Study in Preparation for Facial Transplantation," *Ann Plast Surg*, **76**(2), 249-55 (2016).

175. Vennemann, P., R. Lindken and J. Westerweel, "In vivo whole-field blood velocity measurement techniques," *Experiments in fluids*, **42**(4), 495-511 (2007).

176. Venugopal, V., et al., "Design and characterization of an optimized simultaneous color and near-infrared fluorescence rigid endoscopic imaging system," *J Biomed Opt*, **18**(12), 126018 (2013).

177. Vervandier, J. and S. Gioux, "Single snapshot imaging of optical properties," *Biomed Opt Express*, **4**(12), 2938-44 (2013).

178. Wang, F., et al., "Total skin-sparing mastectomy and immediate breast reconstruction: an evolution of technique and assessment of outcomes," *Ann Surg Oncol*, **21**(10), 3223-30 (2014).

179. Wang, L., S.L. Jacques and L. Zheng, "MCML--Monte Carlo modeling of light transport in multi-layered tissues," *Comput Methods Programs Biomed*, **47**(2), 131-46 (1995).

180. Wang, L.V. and H.-i. Wu, *Biomedical optics: principles and imaging*. 2012: John Wiley & Sons.

181. Wei, F.C., et al., "The outcome of failed free flaps in head and neck and extremity reconstruction: what is next in the reconstructive ladder?," *Plast Reconstr Surg*, **108**(5), 1154-60; discussion 61-2 (2001).

182. Weissleder, R., "A clearer vision for in vivo imaging," *Nat Biotechnol*, **19**(4), 316-7 (2001).

183. Welch, A.J., G. Yoon and M.J. van Gemert, "Practical models for light distribution in laser-irradiated tissue," *Lasers Surg Med*, **6**(6), 488-93 (1987).

184. Wilson, B.C. and G. Adam, "A Monte Carlo model for the absorption and flux distributions of light in tissue," *Med Phys*, **10**(6), 824-30 (1983).

185. Wilson, R.H., et al., "Quantitative short-wave infrared multispectral imaging of in vivo tissue optical properties," *Journal of Biomedical Optics*, **19**(8), 086011- (2014).

186. Wray, S., et al., "Characterization of the near infrared absorption spectra of cytochrome aa3 and haemoglobin for the non-invasive monitoring of cerebral oxygenation," *Biochim Biophys Acta*, **933**(1), 184-92 (1988).

187. Wu, C.C., et al., "Free tissue transfers in head and neck reconstruction: complications, outcomes and strategies for management of flap failure: analysis of 2019 flaps in single institute," *Microsurgery*, **34**(5), 339-44 (2014).

188. Xu, Y., et al., "Absorption and scattering images of heterogeneous scattering media can be simultaneously reconstructed by use of dc data," *Appl Opt*, **41**(25), 5427-37 (2002).

189. Yafi, A., et al., "Postoperative quantitative assessment of reconstructive tissue status in a cutaneous flap model using spatial frequency domain imaging," *Plast Reconstr Surg*, **127**(1), 117-30 (2011).

190. Yang, B., et al., "Polarized light spatial frequency domain imaging for non-destructive quantification of soft tissue fibrous structures," *Biomed Opt Express*, **6**(4), 1520-33 (2015).

191. Yang, B., M. Sharma and J.W. Tunnell, "Attenuation-corrected fluorescence extraction for image-guided surgery in spatial frequency domain," *J Biomed Opt*, **18**(8), 80503 (2013).

192. Yang, B. and J.W. Tunnell, "Real-time absorption reduced surface fluorescence imaging," *J Biomed Opt*, **19**(9), 90505 (2014).

193. Yoo, K.M. and R.R. Alfano, "Determination of the scattering and absorption lengths from the temporal profile of a backscattered pulse," *Opt Lett*, **15**(5), 276-8 (1990).

194. Yoo, K.M., F. Liu and R.R. Alfano, "When does the diffusion approximation fail to describe photon transport in random media?," *Physical Review Letters*, **64**(22), 2647-50 (1990).

195. Yuan, S., et al., "Three-dimensional coregistered optical coherence tomography and line-scanning fluorescence laminar optical tomography," *Opt Lett*, **34**(11), 1615-7 (2009).

196. Zhang, K. and J.U. Kang, "Graphics processing unit accelerated non-uniform fast Fourier transform for ultrahigh-speed, real-time Fourier-domain OCT," *Opt Express*, **18**(22), 23472-87 (2010).

197. Zhang, K. and J.U. Kang, "Real-time 4D signal processing and visualization using graphics processing unit on a regular nonlinear-k Fourier-domain OCT system," *Opt Express*, **18**(11), 11772-84 (2010).

198. Zhao, L., et al., "The integration of 3-D cell printing and mesoscopic fluorescence molecular tomography of vascular constructs within thick hydrogel scaffolds," *Biomaterials*, **33**(21), 5325-32 (2012).

199. Zhao, Y., et al., "Angle correction for small animal tumor imaging with spatial frequency domain imaging (SFDI)," *Biomed. Opt. Express*, **7**(6), 2373-84 (2016).

200. Zhou, W.S. and X.Y. Su, "A Direct Mapping Algorithm for Phase-measuring Profilometry," *Journal of Modern Optics*, **41**(1), 89-94 (1994).

201. Zhu, B., et al., "Validating the sensitivity and performance of near-infrared fluorescence imaging and tomography devices using a novel solid phantom and measurement approach," *Technol Cancer Res Treat*, **11**(1), 95-104 (2012).

202. Zhu, C. and Q. Liu, "Review of Monte Carlo modeling of light transport in tissues," *J Biomed Opt*, **18**(5), 50902 (2013).

203. Zhu, C., Q. Liu and N. Ramanujam, "Effect of fiber optic probe geometry on depth-resolved fluorescence measurements from epithelial tissues: a Monte Carlo simulation," *J Biomed Opt*, **8**(2), 237-47 (2003).